Transport properties of metal-metal and metal-insulator heterostructures

Mohamed Mostafa Fadlallah Elabd

Lehrstuhl für Theoretische Physik II
Universität Augsburg

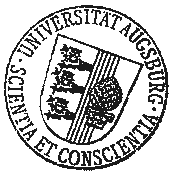

Augsburg, April 2010

Transport properties of metal-metal and metal-insulator heterostructures

Lehrstuhl für Theoretische Physik II
Universität Augsburg

Mohamed Mostafa Fadlallah Elabd

M.Sc. Physics

Benha University
Benha (Egypt)

Supervisors

Prof. Dr. Ulrich Eckern
Institut für Physik
Universität Augsburg

Dr. Cosima Schuster
Institut für Physik
Universität Augsburg

Referees: Prof. Dr. Ulrich Eckern
Priv.-Doz. Dr. Volker Eyert

Oral examination: 9 June 2010

Contents

List of Figures

Chapter 1

INTRODUCTION

1.1 Overview

This thesis is devoted to the theoretical description of charge transport across different interfaces. Electronic transport is a most interesting topic for both technical applications and fundamental understanding of basic physical phenomena. Although electrical phenomena were already known to the Ancient Greeks, systematic studies regarding stationary charge transport (i.e. electrical current) have not been possible until the year 1800, when A. Volta succeeded in building the prototype of today's batteries. After the discovery of the electron in experiments on ionized gases by J. J. Thomson at the Cavendish Laboratory in Cambridge (1897), P. Drude (1900) gave the first microscopic model for electrical conduction by describing the electrons in a metal according to the kinetic theory of gases. Despite its success in explaining many observations, some properties of metals measured at low temperatures, like the specific heat, drastically disagree with the predictions of this model. The underlying classical concepts proved to be causing the disagreement. Therefore, reliable descriptions of charge transport need to be based on quantum mechanics.

As the trend of miniaturization continues, the classical description of the physical phenomena breaks down when approaching the atomic scale, since quantum effects become dominant. Therefore, it becomes mandatory to give a detailed quantum description of the physical properties of the systems in order to understand their electronic structure. A new chapter of physics has been introduced

investigating mesoscopic systems. The motion of electrons in such devices has to be described by quantum theory in order to understand coherent quantum phenomena, like quantum Hall effect [1], Coulomb blockade [2] and conductance quantization [3, 4].

Another new field is called nanophysics, referring to the investigation of matter on the atomic scale. The characterization and manipulation of these nanosystems require experimental and theoretical methods working together. In the 1980s, the scanning tunneling microscope (STM) and atomic force microscope (AFM) gave a significant push to nanoscience. On the other hand, the constant improvement and introduction of novel computer architectures have allowed an ever increasing use of simulations for the analysis of the behaviour of systems at this scale.

A basic question that needs to be addressed before the fabrication of functional electronic devices is: how can we construct the device and understand the conductance of a bulk, wire, and molecule connected to two metallic electrodes? To calculate charge transport across an electrode-material-electrode junction, it is necessary to specify the geometry, the methodology for the computation of the conductance, the Hamiltonian and how the bias voltage across the junction will be treated. Indeed a set of recent theoretical developments has created a new direction of research that influences physics and other sciences. These are the advances in concepts and computational algorithms that have made it possible to treat real systems, as found in nature, as well as idealized model problems. The developments have occurred in recent years and are now the basis for most current research concerning the electronic structure of matter [5]:

- many-body perturbation methods for spectra of excitations;
- quantum Monte Carlo methods, which can deal directly with interacting many-body systems;
- density functional theory for the electronic ground state, and its extensions for excited states.

The density functional theory (DFT) has played and still plays an essential role in the field of computational physics of materials. DFT has been very popular for calculations in solid state physics since the 1970s. Within the DFT framework,

the ground state of an interacting system of electrons in an external potential can be expressed as a functional of the ground state electronic density. Although the theory in principle is exact, there is an unknown part in the energy functional called the exchange-correlation energy that needs to be approximated for practical applications.

The functionality of electronic devices depends crucially on the transport characteristics of interfaces. Several methods, based on electronic structure calculations, have been developed to address the problem of transmission at interfaces and nanocontacts. In the field of mesoscopic and nanoscopic physics there are two different approaches that have been widely used to model ballistic electronic transport: the Landauer method [6] and the non-equilibrium Green's function (NEGF) method [7]. These approaches have become useful especially since it has been possible to fabricate devices of high purity and small dimensions. As an example, in such systems it is possible to confine a two-dimensional electron gas and drive it through a narrow constriction. In such an experiment the quantization of the conductance has been observed for the first time and interpreted in terms of the Landauer theory [4]. The same methods have then been widely applied in molecular transport.

The first-principles approach which combines the non-equilibrium Green's function technique and density functional theory has proven to be very successful. The method can be summarized as follows. First, a non-equilibrium self-consistent procedure based on DFT and NEGF is used to determine the single-particle effective potential. Second, a Landauer-type formula is used to calculate the current, by relating the current to the integral of the single-particle transmission probability over energies. Several DFT-based non-equilibrium transport codes are available, like McDCal [8] and TranSIESTA [9]. The present study employs the SMEAGOL program package [10, 11], a flexible and efficient implementation which consists of a direct summation of both open and closed scattering channels together with a regularization procedure for the Hamiltonian. As a consequence, materials with complex electronic structures can be handled.

The electronic structure near interfaces in solids has attracted growing attention over the last decades due to its importance for technological applications. For these applications new functional heterojunctions are needed. For example, metal-oxide heterostructures gained great scientific and technological interest mainly

due to its advanced gate application in novel MOSFET devices [12] and in ferroelectric memories for the case of ferroelectric oxides [13]. The properties of interfaces differ significantly from those of bulk materials. The energy difference between the characteristic electronic band structures of the materials changes and will strongly affect the electronic transport properties. For example, the charge redistribution at metal-superconductor interfaces can impose severe restrictions on the critical current in wire and tape applications of high-temperature superconductors [14, 15].

Interfaces are also important in semiconductor physics such as for metal-semiconductor interfaces. The energy distribution of the interface states in the semiconductor gap plays physically a very important role for the properties of metal-semiconductor barriers and affects the electrical properties of the related devices [16]. A review on recent developments has been given by Ahn et al. [17], including the creation of highly conductive two-dimensional electron gases at interfaces between insulators [18–20], and the induced charge density in organic-inorganic devices [21–23]. The electron transport across metallic multilayers is of special importance for understanding the giant magnetoresistance in ferromagnetic heterostructures, like Fe/Cr multilayers [24, 25]. Also, hot-electron scattering in Au/Fe/Au trilayers is affected by the metal-metal interfaces [26]. In particular, the attenuation of the electrons strongly depends on the thickness of the Fe interlayer.

Regarding non-magnetic systems, the properties of metal-metal interfaces, for instance, are of interest in many metallurgical applications [27]. For Co/Cu, Fe/Cr, and Au/Ag multilayers the resistance can be increased or decreased by interface disorder, depending on the specific system [28]. Of crucial importance is the understanding of the interplay between interface geometry, electronic structure, functionality, and performance. To elucidate these properties we have performed first-principles calculations based on density functional theory. We concentrated our investigation on metal-metal and metal-insulator (oxide) interfaces.

1.2 Outline of the Thesis

This thesis is organised as follows.

Chapter 2:

A brief overview of density functional theory (DFT) is presented. We also discuss how the electronic structure can be calculated. Subsequently, all approximations that are used to simplify DFT are discussed. The pseudopotential method for solving the Kohn-Sham equations is described.

Chapter 3:

This chapter gives a description of the transport problem where the basic concepts of the Landauer-Büttiker formalism and the non-equilibrium Green's function (NEGF) method are discussed. The transport properties are calculated using the SMEAGOL package.

Chapter 4:

The electronic transport for clean metals is discussed. The bulk (clean) metals are Al, Cu, Ag and Au. In addition, the transport properties for rough metal interfaces are studied. The rough interfaces include vacancy, non-metallic impurity, metallic impurity, metallic interlayer and multilayers.

Chapter 5:

The electronic structure and transport properties of metal-insulator-metal (MIM) junctions are addressed. The Au-MgO-Au junction has two configurations: either Au atoms lie on top O or on top Mg. For these configurations the influence of MgO thickness, interface spacing and O vacancies are tackled.

Chapter 6:

Finally, we provide a summary and conclusion of our results of this thesis.

Appendices:

Appendices A and B include theoretical background about the history of exchange-correlation functionals and pseudopotentials, respectively. The general current formula is derived by using non-equilibrium Green's function in appendix C. We give in appendix D short notes about the density of states.

Chapter 2

THEORETICAL BASIS OF DENSITY FUNCTIONAL THEORY

2.1 Overview

The problem of calculating the electronic structure of a many-particle system is a complicated problem, and a lot of effort has been made to tackle it by various theoretical approaches. Among these, many-body perturbation theory is very popular among theoretical physicists because it allows one to make systematic corrections by adding higher order terms of the perturbation expansion [29, 30]. This method is especially fruitful when a model Hamiltonian can be found and a small parameter exists in which the series can be evaluated. An analytical treatment of the problem may also be possible within this approach [31]. Many-body perturbative theory can also be used in combination with other approaches to perform ab initio calculations (ab initio is from the Latin: from beginning) for atoms, molecules and solids [32–34]. However, the number of particles that can be treated within such a scheme is relatively small due to the high computational cost of the calculations.

A number of non-perturbative methods that are not based on any kind of expansion with respect to a small parameter has been developed [35–37]. The Monte-Carlo and configuration interaction methods are among the most accurate ones. The configuration interaction method [38] is based on a variational proce-

dure and ensures very accurate results for electronic spectra of single atoms and small molecules, but it turns out to be too expensive for extended systems. In recent years there has also been progress in developing Monte-Carlo methods [37] for treating molecular systems and solids. In spite of this progress further development is needed to reduce the computational cost of the calculations, as well as to resolve problems associated with calculating excited states in order to reproduce the entire band structure of solids, for instance. All the above-mentioned methods deal with the many-particle wave function of the system, which is calculated approximately in different ways.

A completely different approach was proposed by Hohenberg and Kohn [39] who formulated the many-particle problem as a variational problem for the total energy as a functional of the density of electrons. This energy functional has a minimum at the exact ground state density. Later Kohn and Sham suggested in [40] to write the electron density in terms of fictitious non-interacting particles. The variational minimum can then be found by solving a set of non-linear equations for these independent particles. This simplifies the many-particle problem considerably, which explains why density functional theory has become such a popular tool for electronic structure calculations [41]. A drawback of DFT is that the exact form of the energy functional is not known and approximations are needed to construct a practical form [42]. There is also a fundamental limitation of DFT because it is originally designed as an exact theory for the ground state only. Time-dependent density functional theory overcomes this limitation [43].

2.2 The Quantum Many Body Problem

A crystal consists of N_a atoms, N_e electrons and the number of nuclei is $N_N = N_a$. Each nucleus has charge $Z \cdot e$, where Z is the atomic number of the chemical element and e is the elementary charge. The exact many-particle Hamiltonian for

this system is:

$$\hat{H} = -\sum_{I}^{N_N} \frac{\hbar^2}{2M_I}\nabla^2_{\mathbf{R}_I} - \sum_{i}^{N_e} \frac{\hbar^2}{2m_e}\nabla^2_{\mathbf{r}_i} + \frac{1}{2}\sum_{i\neq j}^{N_e} \frac{e^2}{|\mathbf{r}_i - \mathbf{r}_j|} - \sum_{i,I}^{N_e,N_N} \frac{e^2 Z_I}{|\mathbf{r}_i - \mathbf{R}_I|} + \frac{1}{2}\sum_{I\neq J}^{N_N} \frac{e^2 Z_J Z_I}{|\mathbf{R}_I - \mathbf{R}_J|}, \tag{2.1}$$

where the mass of the nucleus at $\mathbf{R}_I$ is M_I and the electrons have mass m_e and are at $\mathbf{r}_i$. The first term is the kinetic energy operator of the nuclei, the second of the electrons. The last three terms describe the Coulomb interaction between electrons and other electrons, between electrons and nuclei, and between nuclei and other nuclei. The time-independent Schrödinger equation for the many-body system is:

$$\hat{H}|\psi\rangle = E|\psi\rangle, \tag{2.2}$$

where $\hat{H}$ is given by Eq. (2.1), ψ is the wave function, and E is the total energy. In order to solve Eq. (2.2) some assumptions or approximations are made. The first one is called the Born-Oppenheimer approximation (adiabatic approximation) [44]. The nuclei are much heavier and therefore much slower than the electrons. We can hence 'freeze' them at fixed positions and assume the electrons to be in instantaneous equilibrium with them. So, the kinetic energy of the nuclei is zero. In addition, the last term reduces to a constant and Eq. (2.1) becomes:

$$\begin{aligned}\hat{H} &= -\frac{\hbar^2}{2m_e}\sum_{i}^{N_e} \nabla^2_{\mathbf{r}_i} + \frac{1}{2}\sum_{i\neq j}^{N_e} \frac{e^2}{|\mathbf{r}_i - \mathbf{r}_j|} - \sum_{i,I}^{N_e,N_N} \frac{e^2 Z_I}{|\mathbf{r}_i - \mathbf{R}_I|} \\ &= \hat{T} + \hat{V} + \hat{V}_{ext},\end{aligned} \tag{2.3}$$

where $\hat{T}$ is the kinetic energy of the electrons, $\hat{V}$ the electron-electron interaction and $\hat{V}_{ext}$ the potential energy due to the nuclei. The quantum many body Hamiltonian obtained after applying the Born-Oppenheimer approximation is much simpler than the original one, but it is impossible to solve Eq. (2.2) exactly by using this approximation. The difficulty comes from the second term in this equation, $\hat{V}$. Because of this term we cannot write the total many-electron wave function as a product of single-particle wave functions. Several methods exist to reduce the Hamiltonian, Eq. (2.3), to an approximate but tractable form. A historically very important one is the Hartree-Fock method (HF) [44]. The main problem of the HF

method is in large scale electronic structure calculations, for example and particularly in molecular electronics problems where the computational time is extremely expensive. In addition, the HF method does not contain a correlation potential and some properties are overestimated, like the band gap. A new approach is needed which significantly reduces the number of variables.

2.3 Density Functional Theory

The solution of the many-particle system in terms of the wave function ψ requires the use of sophisticated computational methods [38]. A completely different approach was proposed in density functional theory (DFT). The total ground state energy is then calculated as an integral over a function that depends upon the density of the ground state only, i.e. the energy is a functional of the density. A formal proof for DFT was provided by the Hohenberg-Kohn theorems, see subsection 2.3.1. Density-functional theory has its conceptual roots in the Thomas-Fermi model [45] of a uniform electron gas and the Slater local exchange approximation, see subsection 2.3.2. In many cases DFT gives quite satisfactory results for solid state calculations in comparison to experimental data, at relatively low computational costs when compared to other ways of solving the quantum-mechanical many-body problem.
The literature on DFT and its applications is very large. Some representative examples are the following books [46–48] and review articles [41, 49]. The two core elements of DFT are the Hohenberg-Kohn (HK) theorems [39, 50] and the Kohn-Sham (KS) equations [40]. The former is mainly conceptual, but via the second the most common implementations of DFT have been done.

2.3.1 Hohenberg-Kohn Theorems

Following the idea of using a density functional for solving the many-particle problem, Hohenberg and Kohn formulated their famous theorems [39], which turned out to be a milestone in the density functional formalism.

Theorem 1 *There is a one-to-one correspondence between the external potential, $V_{ext}(\boldsymbol{r})$, of the many-body Hamiltonian, Eq. (2.3), and the corresponding ground state electron density, $\rho_0(\boldsymbol{r})$.*

This theorem is proved by contradiction. Consider two different potentials $V_{ext}(\mathbf{r})$ and $V'_{ext}(\mathbf{r})$ which differ by more than a trivial constant. These potentials give rise to the same density $\rho_0(r)$ and they define two different Schrödinger equations; their ground state wave functions are ψ_0 and ψ'_0. We consider two Hamiltonians. One of them is $\hat{H}$ which contains the potential $V_{ext}(\mathbf{r})$ and has the total energy E_0 and wave function ψ_0 and the other one is $\hat{H}'$ which contains the potential $V'_{ext}(\mathbf{r})$ and has the total energy E'_0 and wave function ψ'_0. According to the variational principle (the variational principle states that the energy is minimal with respect to a variation of the wave function, and is an upper bound to the ground state energy), assuming the ground state to be non-degenerate:

$$E_0 = \langle\psi_0|\hat{H}|\psi_0\rangle < \langle\psi'_0|\hat{H}|\psi'_0\rangle, \tag{2.4}$$

and

$$\langle\psi'_0|\hat{H}|\psi'_0\rangle = \langle\psi'_0|\hat{H}'|\psi'_0\rangle + \langle\psi'_0|\hat{V}_{ext} - \hat{V}'_{ext}|\psi'_0\rangle = E'_0 + \langle\psi'_0|\hat{V}_{ext} - \hat{V}'_{ext}|\psi'_0\rangle, \tag{2.5}$$

so that

$$E_0 < E'_0 + \langle\psi'_0|\hat{V}_{ext} - \hat{V}'_{ext}|\psi'_0\rangle, \tag{2.6}$$

where the inequality is a consequence of the fact that the two potentials are different in a non-trivial way. Interchanging $\hat{V}_{ext}$ and $\hat{V}'_{ext}$, we obtain in the same way:

$$E'_0 < E_0 - \langle\psi_0|\hat{V}_{ext} - \hat{V}'_{ext}|\psi_0\rangle. \tag{2.7}$$

Adding inequalities (2.6) and (2.7), we obtain

$$E_0 + E'_0 < E'_0 + E_0 + \langle\psi'_0|\hat{V}_{ext} - \hat{V}'_{ext}|\psi'_0\rangle - \langle\psi_0|\hat{V}_{ext} - \hat{V}'_{ext}|\psi_0\rangle. \tag{2.8}$$

But the last two terms in the right hand side of inequality (2.8) give

$$\int d^3\mathbf{r}\rho'_0(\mathbf{r})\{V_{ext}(\mathbf{r}) - V'_{ext}(\mathbf{r})\} - \int d^3\mathbf{r}\rho_0(\mathbf{r})\{V_{ext}(\mathbf{r}) - V'_{ext}(\mathbf{r})\} = 0, \tag{2.9}$$

because we considered the assumption that the densities $\rho_0(\mathbf{r})$ and $\rho'_0(\mathbf{r})$ corresponding to the two potentials are the same. This leads to the contradiction $E_0 + E'_0 < E'_0 + E_0$ and proves that our assumption is wrong and the potential $V_{ext}(\mathbf{r})$ is unique up to an additive constant. Now, one can write the total energy

as a functional of the electron density:

$$E[\rho(\mathbf{r})] = \langle\psi|\hat{T} + \hat{V}|\psi\rangle + \langle\psi|\hat{V}_{ext}|\psi\rangle$$
$$= F[\rho(\mathbf{r})] + \int \rho(\mathbf{r})V_{ext}(\mathbf{r})d^3\mathbf{r}, \tag{2.10}$$

where

$$F[\rho(\mathbf{r})] = \langle\psi|\hat{T} + \hat{V}|\psi\rangle, \tag{2.11}$$

and $|\psi\rangle$ is the ground state of $\hat{H}$. The special property of the functional $F[\rho(\mathbf{r})]$ is its universality, because it does not depend on the external potential.

Theorem 2 *The minimization of the functional $E[\rho(\mathbf{r})]$, for a given external potential, yields the exact ground state energy E_0.*

The variational principle gives the following inequality:

$$E[\rho(\mathbf{r})] = \langle\psi|\hat{H}|\psi\rangle > E[\rho_0(\mathbf{r})] \tag{2.12}$$

and $E_0 = E[\rho_0(\mathbf{r})]$. The Hohenberg-Kohn theorems provide us with an exact method for calculating the ground state energy. To describe other ground state properties one has to define density functionals corresponding to these properties, like polarizations. Because the exact expressions for the functionals are not known approximations are needed in order to construct them.

2.3.2 The Kohn-Sham Equations

While the Hohenberg-Kohn theorem rigorously establishes that we may use the density, and the density alone, as a variable to find the ground-state energy of an N_e-electron problem, it does not provide us with any useful computational scheme. The equations of Kohn and Sham turn DFT into a practical tool [40]. To understand these equations we should mention the Thomas-Fermi theory (TF). It is the simplest example of a density functional theory based upon the free electron model. The kinetic energy of an electron is approximated by a function of the local density [41]:

$$E^{TF}[\rho(\mathbf{r})] = \frac{\hbar^2}{2m_e}\kappa \int d^3\mathbf{r}\rho^{5/3}(\mathbf{r}) + \frac{e^2}{2}\int d^3\mathbf{r}\int d^3\mathbf{r}'\frac{\rho(\mathbf{r})\rho(\mathbf{r}')}{|\mathbf{r}-\mathbf{r}'|} + \int d^3\mathbf{r}V_{ext}(\mathbf{r})\rho(\mathbf{r}), \tag{2.13}$$

where the first and second terms are related to the kinetic energy of electrons and the electrostatic energy of the electron-electron interaction, respectively, and $\kappa = 3(3\pi^2)^{2/3}/5$. If the density functional Eq. (2.13) is minimized (by the variational principle):

$$\frac{\delta}{\delta\rho(\mathbf{r})}\{E^{TF}[\rho(\mathbf{r})] - \mu\int d^3\mathbf{r}\rho(\mathbf{r})\} = 0, \tag{2.14}$$

one obtains

$$\frac{5}{3}\frac{\hbar^2}{2m_e}\kappa\rho^{2/3}(\mathbf{r}) + e^2\int d^3\mathbf{r}'\frac{\rho(\mathbf{r}')}{|\mathbf{r}-\mathbf{r}'|} + V_{ext}(\mathbf{r}) = \mu, \tag{2.15}$$

where μ is a Lagrange multiplier or the chemical potential of the system. Eq. (2.15) is called Thomas-Fermi equation [41]. It is clear that Eq. (2.15) should be solved with respect to the electron density $\rho(\mathbf{r})$. However, the density functional for the kinetic energy in Eq. (2.13) is not exact. The approximate treatment of the kinetic energy within the framework of the Thomas-Fermi theory gives rise to many problems [41], since the kinetic energy in TF was obtained by assuming that the density of electrons has slow spatial variations. Furthermore, the exchange-correlation effects between electrons are not taken into account in TF theory.

To simplify the discussion, Kohn and Sham suggested that the energy as a functional of the electron density is a sum of four terms

$$E^{KS}[\rho(\mathbf{r})] = T[\rho(\mathbf{r})] + \frac{e^2}{2}\int d^3\mathbf{r}\int d^3\mathbf{r}'\frac{\rho(\mathbf{r})\rho(\mathbf{r}')}{|\mathbf{r}-\mathbf{r}'|} + E_{xc}[\rho(\mathbf{r})] + \int d^3\mathbf{r}V_{ext}(\mathbf{r})\rho(\mathbf{r}), \tag{2.16}$$

where T is the exact kinetic energy of an auxiliary system of non-interacting particles with the density $\rho(\mathbf{r})$. If we apply the variational principle on Eq. (2.16) we get

$$\frac{\delta T[\rho(\mathbf{r})]}{\delta\rho(\mathbf{r})} + e^2\int d^3\mathbf{r}'\frac{\rho(\mathbf{r}')}{|\mathbf{r}-\mathbf{r}'|} + \frac{\delta E_{xc}[\rho(\mathbf{r})]}{\delta\rho(\mathbf{r})} + V_{ext}(\mathbf{r}) = \mu. \tag{2.17}$$

The density of electrons can be calculated for single-particle wave functions ψ_n as:

$$\rho(\mathbf{r}) = \sum_{n=1}^{N_e}\psi_n(\mathbf{r})\psi_n^*(\mathbf{r}), \tag{2.18}$$

and ψ_n are obtained from

$$\hat{H}^{KS}\psi_n(\mathbf{r}) = \varepsilon_n\psi_n(\mathbf{r}), \tag{2.19}$$

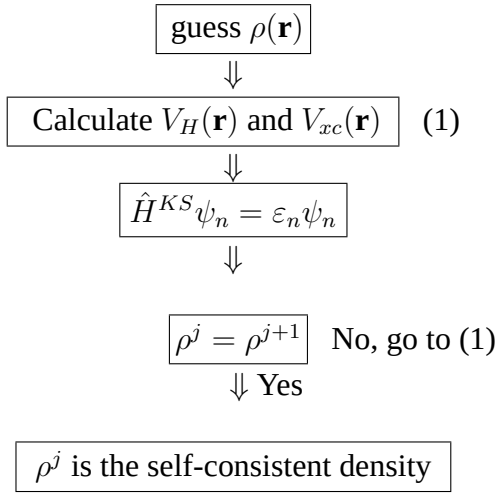

Figure 2.1: Flow chart describing the self-consistent procedure.

where

$$\hat{H}^{KS} = -\frac{\hbar^2}{2m_e}\nabla^2 + V_H(\mathbf{r}) + V_{xc}(\mathbf{r}) + V_{ext}(\mathbf{r}) \tag{2.20}$$

is called Kohn-Sham Hamiltonian. The Hartree potential

$$V_H(\mathbf{r}) = e^2 \int d^3\mathbf{r}' \frac{\rho(\mathbf{r}')}{|\mathbf{r} - \mathbf{r}'|}, \tag{2.21}$$

can also be obtained also by solving the Poisson equation for the scalar potential:

$$\nabla^2 V_H(\mathbf{r}) = -4\pi e^2 \rho(\mathbf{r}), \tag{2.22}$$

while the exchange-correlation energy functional V_{xc} is given by:

$$V_{xc}(\mathbf{r}) = \frac{\delta E_{xc}[\rho(\mathbf{r})]}{\delta\rho(\mathbf{r})}, \tag{2.23}$$

and the single-particle energies ε_n are just Lagrange multipliers to ensure the normalization. The eigenvalue problems Eq. (2.19) are called Kohn-Sham (KS) equations and they are identical to a set of single particle Schrödinger-like equations.

We do not know the exchange-correlation E_{xc} energy functional explicitly; the approximate form of E_{xc} that is used in our calculations will be discussed in the next section. We note that the single-particle wave functions ψ_n are not the wave functions of electrons! They describe a set of non-interacting KS quasi-particles.

Only the overall density of these quasi-particles is guaranteed to be equal to the true electron density. Also the single-particle energies ε_n are not single-electron energies. Both the Hartree operator $\hat{V}_H$ and the exchange-correlation operator $\hat{V}_{xc}$ depend on the density $\rho(\mathbf{r})$, which in turn depends on the ψ_n, which are being searched. This problem can be solved by an iterative self-consistent procedure (see Fig. 2.1).

2.4 The Exchange-Correlation Functional

The most difficult problem in any electronic structure calculation is posed by the need to take into account the effects of the electron-electron interaction. Electrons repel each other due to the Coulomb interaction between their charges. The Coulomb energy of a system can be reduced by keeping the electrons spatially separated, but this has to be balanced against the kinetic-energy cost of deforming the electronic wave functions in order to separate the electrons. The wave function of a many-electron system must be antisymmetric under exchange of any two electrons because electrons are fermions. The antisymmetry of the wave function produces a spatial separation between electrons that have the same spin and thus reduces the Coulomb energy of the system. This reduction in energy due to antisymmetry in the wave function is called exchange energy. The Coulomb energy can be reduced further if the electrons that have opposite spins are also spatially separated, this decrease is called the correlation energy.

Modeling the exchange and correlation interactions becomes difficult within KS DFT as the exact functionals for exchange and correlation are not known except for the homogeneous (uniform) electron gas. However, approximations exist that permit the calculation of real systems. So we make some approximations like the local density approximation (LDA) [40, 51] which is widely used:

$$E_{xc}^{LDA} = \int d^3r \rho(\mathbf{r}) e_{xc}[\rho(\mathbf{r})]. \tag{2.24}$$

The functional e_{xc} for the homogeneous (uniform) electron gas [52] is numerically known.

The next logical step to improve on LDA is by including the gradient of the

density. This approximation is therefore called the generalized gradient approximation (GGA) [53]:

$$E_{xc}^{GGA} = \int d^3 r F(\rho, \nabla\rho). \tag{2.25}$$

It should be mentioned here that both LDA and GGA are local approximations while the exact exchange-correlation potential is non-local (Appendix A).

2.5 How Can We Solve the Kohn-Sham Equations?

There are two different schemes to solve the Kohn-Sham Eq. (2.19). In the first scheme the Kohn-Sham Hamiltonian and wave function are discretized on a numerical grid by using a real-space approach [41, 54]. The second scheme relies on expanding the Kohn-Sham orbitals over a complete basis set. This scheme is used in the SIESTA package. Within this scheme the KS orbitals are expanded as

$$\psi_i(\mathbf{r}) = \sum_l c_l^i \phi_l(\mathbf{r}), \tag{2.26}$$

where $\phi_l(\mathbf{r})$ is a basis set of functions. We can separate the basis sets into two major groups [55–58]: plane waves (PW) and localized atomic orbitals. It is also possible to construct a mix of these two groups. Plane waves require a large number of basis functions in order to describe localized states. On the other hand, there are a number of advantages in using a localized basis set. One of these is that the range of interaction is finite and consequently Hamiltonian matrix elements go to zero for orbitals that are far apart in space. Therefore the Hamiltonian and the overlap matrix, $S_{ij} = \langle\phi_i|\phi_j\rangle$, become relatively sparse saving memory and computer time. This common basis set is composed of a finite number of atomic orbitals (linear combination of atomic orbitals (LCAO) ansatz), centered at each atomic nucleus. Initially, these atomic orbitals were Slater orbitals, which decay exponentially with distance from the nuclei. Later, it was realized that these Slater-type orbitals could be approximated as linear combinations of Gaussian orbitals. On the one hand it is easier to calculate overlap and other integrals with Gaussian basis functions, on the other hand very large numbers of Gaussian functions are needed for an accurate description of each orbital, which requires huge

computational memory. The smallest of these sets are called minimal (also single-zeta, SZ) basis sets, and they are composed of one basis function for each atomic orbital. The largest set can contain literally dozens to hundreds of basis functions on each atomic orbital.

It is the valence electrons which principally take part in the bonding. In recognition of this fact, it is common to represent valence orbitals by more than one basis function. Basis sets in which there are multiple basis functions corresponding to each valence atomic orbital, are called valence double (DZ), triple (TZ), quadruple-zeta (QZ), etc. basis sets. Using a linear combination of basis functions the problem reduces to that of finding the expansion coefficients that minimize Eq. (2.19).

2.6 Pseudopotential

The calculations are still very complex due to the large number of electrons in the system. To simplify matters, the concept of norm-conserving pseudopotentials [59] and later ultrasoft pseudopotentials [60] has been developed.

It is well known that most physical properties of solids depend on the valence electrons to a much greater extent than on the core electrons. Pseudopotential theory allows us to use an effective potential that absorbes the effect of the core electrons on the valence electrons into a pseudopotential, so that the core electrons are not needed anymore to describe the valence electrons. Thus the original solid is now replaced by pseudo-valence electrons and pseudo-ion cores. These pseudoelectrons experience exactly the same potential outside the core region as the original electrons but have a much softer potential inside the core, i.e. the rapid oscillation of the wave function in the core region is removed (no radial nodes). Pseudopotentials [59–67] are constructed in such a way that they are much smoother than the original all electron potentials (Appendix B). That reduces the dimension of the basis set. There is no unique recipe to construct a pseudopotential, but there are two conditions which should be verified for any good pseudopotential:

1- Only a small number of basis functions is used.

2- It can be used in whatever environment (molecule, cluster, solid, surface, insu-

lator, metal,...).

2.7 SIESTA Code

The increase in computer power and the progress in numerical methods have allowed ab initio calculations of increasingly more complex and larger systems with an increasing number of atoms N_a. In the HF LCAO and DFT PW methods the computer time and memory scales with N_a like N_a^2 or N_a^3 [54].

SIESTA (*Spanish Initiative for Electronic Simulations with Thousands of Atoms*) is a linear system-size scaling order-N DFT LCAO method for periodic systems that was developed as a general purpose, flexible DFT computer code [68]. We can use SIESTA to perform electronic structure calculations and ab initio molecular dynamics simulations of molecules and solids [68]. The SIESTA density functional for crystalline solids uses numerical atomic orbital (AO) basis sets. The exchange-correlation functionals LDA and GGA are implemented in the SIESTA code. This code uses the norm-conserving pseudopotentials in its fully nonlocal (Kleinman-Bylander) form.

The first step in the SIESTA method calculation is the choice of pseudopotentials. The SIESTA method relies on the use of strictly confined basis atomic orbitals, i.e. orbitals that are zero beyond a certain radius which is called cutoff radius r_c. This keeps the energy variational and the matrix elements of the Hamiltonian have finite range. Within the nonlocal pseudopotential approximation, the standard KS one-electron Hamiltonian is written as:

$$\hat{H}^{KS} = \hat{T} + \sum_I \hat{V}_I^{loc} + \sum_I \hat{V}_I^{nloc} + \hat{V}_H + \hat{V}_{xc}, \tag{2.27}$$

where I is an atom index, and the pseudopotential operator is the sum of the local $\hat{V}_I^{loc}$ and nonlocal $\hat{V}_I^{nloc}$ parts of the pseudopotential of atom I.

In order to eliminate the long range of V_I^{loc} it is screened with the screened neutral atom (NA) potential V_I^{NA} which is created by a neutral atom charge density ρ_I^{NA}. The neutral atom potential is defined as follows [57]:

$$V_I^{NA} = V_I^{loc} + e^2 \int d^3\mathbf{r}' \frac{\rho^{NA}(\mathbf{r}')}{|\mathbf{r} - \mathbf{r}'|}, \tag{2.28}$$

this potential is short range, since the core attraction and the electron Coulomb repulsion of the neutral atom charge cancel each other beyond r_c. Substituting from Eq. (2.28) into Eq. (2.27) one gets:

$$\hat{H}^{KS} = \hat{T} + \sum_I \hat{V}_I^{nloc} + \sum_I \hat{V}_I^{NA} + \delta\hat{V}_H + \hat{V}_{xc}, \tag{2.29}$$

where

$$\begin{aligned} \delta V_H(\mathbf{r}) &= e^2 \int d^3\mathbf{r}' \frac{\rho(\mathbf{r}') - \rho^{NA}(\mathbf{r}')}{|\mathbf{r} - \mathbf{r}'|} \\ &= e^2 \int d^3\mathbf{r}' \frac{\delta\rho(\mathbf{r}')}{|\mathbf{r} - \mathbf{r}'|}. \end{aligned} \tag{2.30}$$

Here $\delta\rho(\mathbf{r}') = \rho(\mathbf{r}') - \rho^{NA}(\mathbf{r}')$. The first three terms in Eq. (2.29) are independent of the charge density $\rho(\mathbf{r})$ and their matrix elements are calculated in reciprocal space and tabulated as a function of interatomic distance. On the other hand $\delta\hat{V}_H$ and $\hat{V}_{xc}$ depend on the charge density $\rho(\mathbf{r})$ and the matrix elements of these potentials are calculated on a real space grid.

There are two numerical procedures to find the ground state of $\hat{H}^{KS}$: (i) Direct diagonalization method and (ii) Iterative minimization method. The second method is very convenient for calculations which include large systems or large basis sets. This method was developed to deal with nonorthonormal basis sets to calculate the overlap matrix and after that the Gram-Schmidt orthonormalization procedure is used to restrict the minimization to orthonormal states during the energy minimization. The principle problem of exact diagonalization is that the computational time needed increases as N_a^3 with the number of atoms N_a. Several iterative order-N methods have been developed, i.e. whose computational cost scales only linearly with the number of atoms [69–72].

Two options are available for minimizing the ground state: direct diagonalization and order-N in the SIESTA code. Order-N in SIESTA contains two constituents: The first is the calculation of the wave functions $\psi_i(\mathbf{r})$ describing the ground state of the system by the minimization of a modified energy functional, which does not require an explicit orthogonalization step, but for which the wave functions become automatically orthonormal at the minimum.

The second is the restriction of the minimization of the energy functional to wave functions which are localized in space (Wannier-like wave functions). Each

atom I is assigned a number of states equal to $\mathrm{int}(Z_I^{valence}/2+1)$ so that, if doubly occupied, they can contain at least one excess electron (they can also become empty during the minimization of the energy functional). These states are confined to a sphere of radius R_c (different from the cutoff of the LCAO basis orbital r_c) centered at nuclei $\mathbf{R}_I$.

The SIESTA method provides a very general scheme to perform a range of calculations from very fast to very accurate, depending on the needs and stage of the simulation, of all kinds of molecule, material and surface. It allows DFT simulations of more than a thousand atoms in modest PC workstations, and over a hundred thousand atoms in parallel platforms. The numerous applications of the SIESTA DFT LCAO method can be found on the SIESTA code site [68].

Chapter 3

QUANTUM ELECTRON TRANSPORT

3.1 Transport Problem

Mesoscopic systems are intermediate between the microscopic and the macroscopic scales. Several important discoveries such as the quantum Hall effect and the quantization of conductance are all results of intense studies of electron transport in the mesoscopic regime [73, 74].

When electrons move in a material they scatter from impurities, other lattice defects and from phonons. Usually, the scattering from other electrons is less important [75]. The scattering causes electrical resistance. In macroscopic-size electronic components, the conductance follows:

$$G = \sigma A/L, \tag{3.1}$$

where σ is the conductivity, A the perpendicular area of the conductor, and L is the length. Ohm's law is understandable because typically the scatterers are uniformly distributed within the material, and a longer device has also more scatterers to reduce the collective electron drift motion. According to this law the conductance should vanish as the conductor gets narrower and $A \to 0$, and it becomes infinite for very short conductors, $L \to 0$. This behaviour relies on the assumption that the conductivity does not depend on the size of the conductor because it is a macroscopically defined quantity, which is assumed to be homoge-

nous over the conductor. If the size of the conductor reaches the atomic scale then the homogeneity of the conductivity is violated, and Ohm's law must break down. The failure of Ohm's law was indeed seen in experiments on quantum point contacts [4] and atomic-sized wires [76], where a stair-case behavior of the conductance was observed during narrowing of the point contact and elongation of the wire, respectively. An important issue is to define the characteristic size of the conductor when the macroscopic description is no longer applicable.

There are three length scales that are important in determining this size [73]:

- the de Broglie wavelength, i.e. the electron wavelength at the Fermi-level, which is related to the kinetic energy of the electrons;
- the mean free path, which is the average distance that an electron passes without changing its momentum, e.g. such events occur due to scattering at impurities;
- the phase relaxation length, which is the average distance that an electron passes without destroying its phase. Phase loss takes place due to inelastic scattering caused by the electron-electron and electron-phonon interactions.

A conductor usually exhibits ohmic behavior if its size is much larger than any of these length scales. The characteristic lengths depend on the material considered, and they can be affected by temperature or magnetic field. If the dimensions of the conductor is intermediate between microscopic and macroscopic then it is called a mesoscopic conductor having a size of tens or hundreds nanometers. Microscopic conductors have nanometer dimensions, and are often called atomic-sized conductors. Because the phase relaxation length in the mesoscopic and atomic-scaled conductors is larger than their dimensions, the electronic transport can be treated as coherent. The latter means that a fully quantum-mechanical treatment is required for an adequate description of the electron propagation in such conductors.

In the following we report on a computational technique that can be used for solving the electronic coherent transport problem in mesoscopic and nanoscale conductors. A quantum-mechanical formulation of the electronic transport through small conductors was first proposed by Landauer [6, 73]. Landauer suggested a simple formula which established the relation between the transmission probability of the electron and the electronic conductance in one-dimensional conductors.

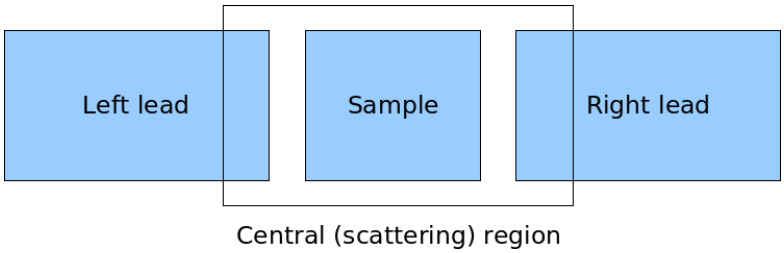

Figure 3.1: Schematic of the system used to study electron transport.

Landauer's idea was generalized by Fisher and Lee [77] for multi-channel three-dimensional conductors, using the linear response formalism. Büttiker [78, 79] proposed a multi-channel Landauer formula for multi-probe devices. A brief overview of the Landauer-Büttiker formalism is given next.

3.1.1 The Landauer Approach

The Landauer approach is a milestone in this field because of its conceptual simplicity and its predictive power. In the Landauer approach one imagines to have a small region (molecule, or any nanoscopic structure) connected to two macroscopic regions (the electrodes). One ideally partitions the system in several regions (see Fig. 3.1): (i) a central region (C) that includes the sample and a portion of the electrodes that is influenced (through geometric and charge rearrangements) by the presence of the molecule; (ii) a left (L) and right (R) lead connected to the molecule; (iii) two electron reservoirs connected to the leads, in equilibrium at some electrochemical potential $\mu_{L/R}$. The leads (often simply called electrodes) are assumed to be ballistic conductors, i.e. conductors with no scattering and thus with transmission probability equal to one. Often one does not distinguish between leads and reservoirs: what is meant in that case is that the leads are macroscopic regions that can be treated as electron reservoirs at fixed electrochemical potential. According to Landauer, transport, in such a geometry, should be viewed as a scattering problem: an incident carrier flux from one of the leads is scattered by the region C and transmitted to the other lead. The current will then be proportional to the transmission coefficient, i.e. the probability for an electron to be transmitted from one lead to the other. This approach applies to a system of elec-

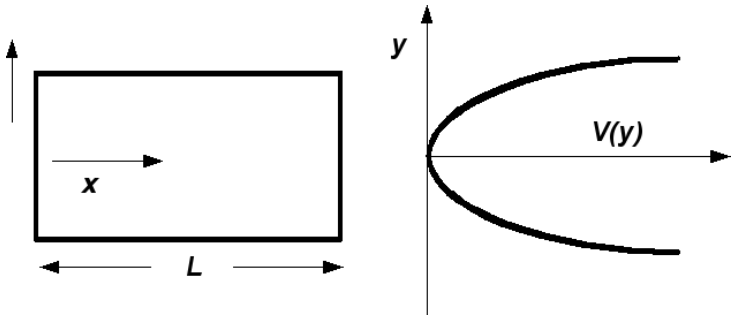

Figure 3.2: A two-dimensional system assumed to be uniform in the x-direction and the confining potential $V(y)$.

trons in which no inelastic scattering mechanisms are present: transport is therefore assumed to be coherent. We will now present a derivation of the Landauer formula that is by no means rigorous, but nonetheless it shows what are the major assumptions in this approach. A rigorous derivation of the Landauer formula in the linear response regime can be found in [73]. Let us consider for simplicity a two-dimensional system in which the conductor (the central region in Fig. 3.1) is uniform in the x direction and has a transverse confining potential $V(y)$ in the y direction. We can take such potential to be harmonic, see Fig. 3.2. The Schrödinger equation in the conductor is then:

$$\left(\frac{p_x^2}{2m} + \frac{p_y^2}{2m} + V(y)\right)\psi(x,y) = E\psi(x,y). \tag{3.2}$$

The solutions of Eq. (3.2) can be put in the form

$$\psi(x,y) = \frac{1}{\sqrt{L}} e^{ikx}\chi(y), \tag{3.3}$$

where L is the length of the conductor over which the wave functions are normalized. The potential $V(y)$ gives rise to quantized levels that we can label with the index n. These levels are called subbands or transverse modes, in analogy to the terminology used for electromagnetic waveguides. The dispersion relation $E_n(k)$ is quadratic for each subband, and different subbands are separated by a constant amount, given our choice of the confining potential. At a fixed energy E there will be a finite number of subbands crossing that energy: we use the symbol $M(E)$ to denote this quantity [73].

One then assumes that the application of a bias V to the electrodes shifts the electrochemical potential of the reservoirs such that $\mu_L - \mu_R = eV$. In the Landauer approach one further assumes that the contacts are not reflecting, i.e. an electron in the conductor can enter the electrode without suffering any reflection. Here the reservoirs are then treated as the classical analog of the radiative black body: they adsorb incident carriers without reflection and they emit carriers with a fixed thermal equilibrium distribution. So the states in the left lead corresponding to positive momentum in the x direction $(+k)$ are occupied with the equilibrium distribution $f_L(E)$ and the ones with negative momentum $(-k)$ in the right lead are occupied with the distribution $f_R(E)$. With these assumptions we are now in a position to compute the current. We will first neglect all possible scattering processes in the central region C, meaning that transport is assumed to be ballistic in that region. A uniform electron gas with n electrons per unit length moving with velocity v carries a current equal to env. Given that the electron density of a single $+k$ state in a conductor of length L is $1/L$, the current that the $+k$ state carries is

$$I^+ = \frac{e}{L}\sum_k v_k f_L(E_k) = \frac{e}{L}\sum_k \frac{1}{\hbar}\frac{\partial E}{\partial k} f_L(E_k). \tag{3.4}$$

Converting the sum over k into an integral in Eq. (3.4):

$$\sum_k \rightarrow 2L \int \frac{dk}{2\pi}, \tag{3.5}$$

(factor 2 is for spin) and including the contribution of all subbands one gets:

$$I^+ = \frac{2e}{h}\int_{-\infty}^{\infty} f_L(E) M(E) dE, \tag{3.6}$$

where $M(E)$ is the number of propagating modes at energy E and $\hbar = h/2\pi$. In the same way we can calculate the contribution to the current coming from states with negative momentum:

$$I^- = \frac{2e}{h}\int_{-\infty}^{\infty} f_R(E) M(E) dE. \tag{3.7}$$

If we assume that the number of modes is constant over the energy range $\mu_R < E < \mu_L$, at zero temperature, the total current can be obtained by:

$$I = I^+ - I^-. \tag{3.8}$$

Substituting from Eq. (3.6) and Eq. (3.7) into Eq. (3.8) we obtain:

$$I(V) = \frac{2e^2}{h} M \frac{\mu_R - \mu_L}{e} = \frac{2e^2}{h} MV, \tag{3.9}$$

and from Eq. (3.9) one can write the conductance as:

$$G_C = \frac{2e^2}{h} M. \tag{3.10}$$

We notice that the conductance in Eq. (3.10) is quantized because the integer nature of M. Furthermore the resistance is given by:

$$R_C = G_C^{-1} = \frac{h}{2e^2 M} = \frac{12.9}{M} k\Omega. \tag{3.11}$$

Somewhat surprisingly, this resistance is finite for an ideal conductor even though there is no electron scattering. This resistance comes from the contact of the conductor and the reservoirs so it is called contact resistance. These predictions have been confirmed by a number of experiments in mesoscopic semiconductor systems [4] in which by changing the gate voltage applied to the conductor (and thus changing the number of transverse modes M) the conductance is increased stepwise by units of $2e^2/h$, in agreement with Eq. (3.10). The unit $G_0 = 2e^2/h$ is called *quantum of conductance*. If we now allow for the conductor to have a transmission probability T different from one (at this point we assume it to be energy independent) the conductance is given by:

$$G = \frac{2e^2}{h} TM. \tag{3.12}$$

We can extend this result to the general case in which both T and M are energy dependent, and obtain the current as follows:

$$I = \frac{2e}{h} \int_{-\infty}^{\infty} T(E) M(E) (f_L(E) - f_R(E)) dE. \tag{3.13}$$

In the linear response regime and at low temperatures this gives:

$$G = \frac{2e^2}{h} T(E_F) M(E_F), \tag{3.14}$$

where E_F is the Fermi energy of the system.

The experimental measurements have shown that a monoatomic gold wire between two gold surfaces has a conductance of one quantum and has a single transverse mode contributing to the current [80–82]. So this system behaves like a perfect ballistic conductor according to the Landauer picture.

How can we calculate the energy dependent transmission function of the conductor C to apply the Landauer approach? What is the relation between the transmission function of the conductor C and the applied voltage V? The non-equilibrium Green's function is used to answer these two questions.

3.1.2 Non-Equilibrium Green's Function Method

The first-principles theoretical studies of the atomic and electronic structure as well as the transport properties of molecular devices are important and useful, since they supplement and guide the experiments. For the calculation of the junction conductance, the non-equilibrium Green's function (NEGF) formalism has proved to be a powerful and formally rigorous approach [83, 84]. For non-interacting electrons and neglecting inelastic scattering the NEGF and Landauer formalisms are equivalent [83].

In the NEGF method, one partitions the system in the same way as in the Landauer method. The electronic structure of the different regions are computed, depending on different implementations of the NEGF method, in different ways. When a cluster geometry, i.e. a stable aggregation or group of atoms or molecules distinguished by certain physical or chemical features from other similar stable micro objects, is adopted then the central region (C) is isolated into the cluster and the electrodes are considered bulk-like [85]. In other implementations the electronic structure is computed with periodic boundary conditions (pbc) [9, 86]. In this case the portion of the electrodes included in the calculation must be big enough so that, away from the molecule, the leads have bulk properties and also big enough to avoid spurious interactions between the periodic replicas of the molecule. After we compute the wave function of the ground state, the Green's function of the region C is computed. The effect of the leads on the molecule is taken into account through the self-energies of the leads. This approach involves the calculation of the lead surface Green's function for all the energies in the mesh considered and typically this is the most expensive part of the calculation. Once

this is done, one computes the new charge density in the region C and the new potential and repeats the calculation until self-consistency is reached. To calculate the current, the Landauer formula Eq. (3.13) is commonly used, where the transmission function is computed from the Green's function and the self-energies. The inclusion of effects like inelastic scattering or electron-electron interactions are possible in this formalism by adding to the molecule Green's function the appropriate self-energies that take into account such effects [73]. In the field of molecular transport only few attempts have been done in this direction [87, 88], whereas more literature is available for mesoscopic systems [89].

Though the electronic structure of isolated molecules and periodic solids can be calculated accurately and efficiently with density functional theory (DFT) under the Kohn-Sham (KS) ansatz [5, 48]. The NEGF+DFT approach combines the NEGF formalism with DFT employing a finite set of local orbitals and should be regarded as a practical method, rather than a rigorously exact theory. In order to use the NEGF+DFT approach properly and to know where further improvements are needed in future studies, we should know the various approximations involved. Using the non-equilibrium Keldysh formalism, Meir and Wingreen derived a formula for the current through a region of interacting electrons coupled to two multichannel leads where the electrons are non-interacting by using orthonormal basis sets to describe the wave functions [83]. Recently, Thygesen has generalized the current formula to non-orthogonal basis sets [84], which lays a firm foundation for the commonly used NEGF+DFT approach in which local basis functions are often employed. Here, for simplicity, the derivation of the current formula is given following Meir and Wingreen (Appendix C) .

Let us discuss why the leads are important for the transport characteristics of the molecule. In a molecule in vacuum one can think of electronic orbitals with well defined energies. Coupling the molecule to leads will change this structure. An electron can hop from the molecule into the lead and back, and therefore has a finite lifetime in the molecule. This leads to a broadening of the molecular orbitals in energy. Details of hybridization will determine the broadening and shifting of the orbital energies and thus are crucial for understanding the transmission through the molecule in a profound manner. The leads are taken into account in the transport calculation via a self-energy, which describes the coupling of the

molecule system to the surrounding medium, the leads. Including the leads in the self-energy makes the calculation of the molecule numerically very cheap at a first glance, but the self-energy is a very complex operator since it has to contain all information about the interaction between the molecular orbitals and the leads. An exact self-energy for realistic systems is not easily constructed, and approximations often lead to artifacts in the transmission function. Instead of ignoring the leads in the self-consistent (SC) calculation, one can deal with the hybridization by including a finite number of lead atoms in the DFT calculation, introducing the so called extended molecule and coupling the extended molecule to leads via a self-energy. The advantage of the extended molecule in comparison with the molecule in vacuum is that hybridization is explicitly included in the DFT calculation.

Among the packages using a combination of DFT and the non-equilibrium Green's functions method for calculating transport properties, SMEAGOL is chosen for our investigations [10, 11]. SMEAGOL is based on the DFT package SIESTA [68] which provides the required basis set of local atomic orbitals. The surface Green's functions are calculated using semi-analytical expressions, which result in a great improvement with respect to recursive methods.

The McDCal code [8], for example, likewise relies on an atomic orbital basis [57] but solves the electrostatic problem by a real-space multi-grid approach [90]. On the other hand, the GECM transport code [91, 92] simplifies the treatment of the leads by introducing a tight-binding Bethe lattice [93]. The TranSIESTA code [9] is an extension of SIESTA, solving the electrostatic problem in momentum space and calculating the surface Green's functions by direct integration.

3.2 SMEAGOL Code and the Transport Problem

SMEAGOL (*Spin and Molecular Electronics Algorithm on a Generalized atomic Orbital Landscape*) [10, 11] is based on the non-equilibrium Green's function (NEGF) formalism for one-particle Hamiltonians. In its present form it uses density functional theory (DFT) with the numerical implementation contained in the code SIESTA [68]. It has been designed to describe two-terminal conductance experiments, where two electrodes of macroscopic size sandwich a nanometer-size device (a molecule, an atomic point contact, a tunneling barrier, etc.). It should

be noticed that the two semi-infinite current-voltage probes are defect-free crystalline metals. These have a regular periodic structure and a bulk unit cell along which the direction of the transport can be defined. It is convenient to introduce the concept of principal layer (PL). A principal layer is the smallest cell that repeats periodically in the direction of the transport constructed in such a way to interact only with the nearest-neighbor PL's. This means that all the matrix elements between wave functions belonging to two non-adjacent PL's vanish.
The system under investigation is described by an infinite hermitian matrix $\mathcal{H}$ which is written as:

$$\mathcal{H} = \begin{pmatrix} \dots & \dots & \dots & \dots & \dots & \dots & \dots & \dots & \dots & \dots & \dots \\ \dots & 0 & H_{-1} & H_0 & H_1 & 0 & \dots & \dots & \dots & \dots & \dots \\ \dots & \dots & 0 & H_{-1} & H_0 & H_{LM} & \dots & \dots & \dots & \dots & \dots \\ \dots & \dots & \dots & 0 & H_{ML} & H_M & H_{MR} & 0 & \dots & \dots & \dots \\ \dots & \dots & \dots & \dots & 0 & H_{RM} & H_0 & H_1 & 0 & \dots & \\ \dots & \dots & \dots & \dots & \dots & 0 & H_{-1} & H_0 & H_1 & 0 & \dots \\ \dots & \dots & \dots & \dots & \dots & \dots & \dots & \dots & \dots & \dots & \dots \end{pmatrix}. \tag{3.15}$$

One can write the above matrix in the following way:

$$\begin{pmatrix} \mathcal{H}_L & \mathcal{H}_{LM} & 0 \\ \mathcal{H}_{ML} & H_M & \mathcal{H}_{MR} \\ 0 & \mathcal{H}_{RM} & \mathcal{H}_R \end{pmatrix}. \tag{3.16}$$

H_0 is defined as the $N \times N$ matrix describing all interactions within a PL, where N is the total number of degrees of freedom (basis functions) in the PL (note that we use calligraphic symbols $\mathcal{H}$ for infinitely dimensional matrices and capitalized letters H for finite matrices). Similarly H_1 is the $N \times N$ matrix describing the interaction between two PL's. Finally H_M is the $M \times M$ matrix describing the extended molecule (EM) and H_{LM} (H_{RM}) is the $N \times M$ matrix containing the interaction between the last PL of the left-hand side (right-hand side) lead and the extended molecule (Fig. 3.3). The Green's function $\mathcal{G}^r$ is calculated from the equation

$$\left(\epsilon^+ \mathcal{S} - \mathcal{H}\right) \mathcal{G}^r = \mathcal{I}, \tag{3.17}$$

where $\epsilon^+ = lim_{\delta \to 0^+}(E + i\delta)$, $\mathcal{S}$ is the overlap matrix which is calculated by using a nonorthogonal basis set and $\mathcal{I}$ is an infinitely-dimensional identity matrix (after

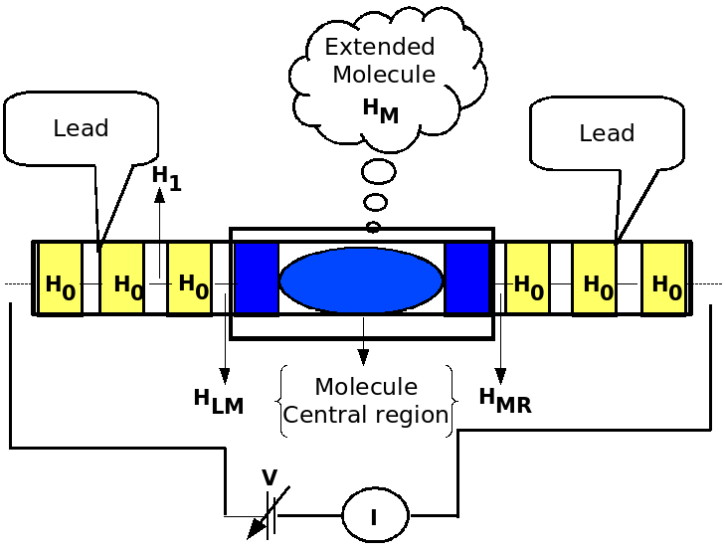

Figure 3.3: An open system with a molecule sandwiched between two electrodes (leads).

that we drop the symbol r indicating the retarded quantities). One can rewrite Eq. (3.17) in the following form:

$$\begin{pmatrix} \epsilon^{+}\mathcal{S}_L - \mathcal{H}_L & \epsilon^{+}\mathcal{S}_{LM} - \mathcal{H}_{LM} & 0 \\ \epsilon^{+}\mathcal{S}_{ML} - \mathcal{H}_{ML} & \epsilon^{+}S_M - H_M & \epsilon^{+}\mathcal{S}_{MR} - \mathcal{H}_{MR} \\ 0 & \epsilon^{+}\mathcal{S}_{RM} - \mathcal{H}_{RM} & \epsilon^{+}\mathcal{S}_R - \mathcal{H}_R \end{pmatrix} \begin{pmatrix} \mathcal{G}_L & \mathcal{G}_{LM} & \mathcal{G}_{LR} \\ \mathcal{G}_{ML} & G_M & \mathcal{G}_{MR} \\ \mathcal{G}_{RL} & \mathcal{G}_{RM} & \mathcal{G}_R \end{pmatrix} = \mathcal{I}. \tag{3.18}$$

We have partitioned the Green's functions $\mathcal{G}$ into infinite blocks describing the left- and right-hand side leads $\mathcal{G}_L$ and $\mathcal{G}_R$. The interaction between the leads and the extended molecule is described by $\mathcal{G}_{LM}$, $\mathcal{G}_{RM}$. $\mathcal{G}_{LR}$ describes the direct scattering between the leads, and G_M is the finite block describing the extended molecule. The final expression for G_M has the form:

$$G_M = \left[\epsilon^{+}S_M - H_M - \Sigma_L - \Sigma_R\right]^{-1}, \tag{3.19}$$

where we have introduced the retarded self-energies for the left- and right-hand side lead:

$$\Sigma_{L/R} = \left(\epsilon^{+}S_{ML/R} - H_{ML/R}\right) G^{s}_{ML/R} \left(\epsilon^{+}S_{L/RM} - H_{L/RM}\right). \tag{3.20}$$

$G^s_{ML/R}$ is the retarded surface Green's function of the leads, i.e. the leads retarded Green's function evaluated at the PL neighboring to the extended molecule. There are a number of techniques to calculate the surface Green's function of a semi-infinite system. These techniques range from recursive methods [94] to semi-analytical constructions [11]. SMEAGOL uses the generalization of the scheme to non-orthogonal basis sets. This method gives us a prescription for calculating the retarded surface Green's function exactly (Appendix C). The main idea is to construct the Green's function for an infinite system as a summation of Bloch states with both real and imaginary wave-vectors, and then to apply the appropriate boundary conditions to obtain the Green's function for a semi-infinite lead.

All the electronic structure information of the extended molecule connected to the leads are contained in the retarded Green's function G_M. One can get the conductance of the system by applying the Fisher-Lee relation [77]:

$$G = \frac{2e^2}{h}\mathrm{Tr}[\Gamma_L G_M^\dagger \Gamma_R G_M], \tag{3.21}$$

where Tr represents the trace, i.e. the sum over diagonal elements, and

$$\Gamma_{L/R} = i[\Sigma_{L/R}(E) - \Sigma_{L/R}^\dagger(E)]. \tag{3.22}$$

Eq. (3.21) is evaluated at the Fermi energy E_F. The quantity $\mathrm{Tr}[\Gamma_L G_M^\dagger \Gamma_R G_M]$ is the energy dependent total transmission coefficient of standard scattering theory [78].

When an external bias V is applied, the charge distribution on the extended molecule will differ from the one at equilibrium since both the net charge and the electrical polarization are affected by the bias. This will determine a new electrostatic potential profile with different scattering properties. The only effect of the external bias on the electrodes is a rigid shift of the on-site energies. The Hamiltonian then takes the form:

$$\begin{pmatrix} \mathcal{H}_L + \mathcal{S}_L\frac{eV}{2} & \mathcal{H}_{LM} + \mathcal{S}_{LM}\frac{eV}{2} & 0 \\ \mathcal{H}_{ML} + \mathcal{S}_{ML}\frac{eV}{2} & H_M & \mathcal{H}_{MR} - S_{MR}\frac{eV}{2} \\ 0 & \mathcal{H}_{RM} - \mathcal{S}_{RM}\frac{eV}{2} & \mathcal{H}_R - S_R\frac{eV}{2} \end{pmatrix}. \tag{3.23}$$

The Hamiltonian of the extended molecule,

$$H_M = H_M[\rho], \tag{3.24}$$

depends on the density matrix. This density matrix is calculated using the lesser Green's function [73, 95]:

$$\rho_M = \frac{1}{2\pi i}\int dE\, G_M^<(E). \tag{3.25}$$

The non-equilibrium Green's function formalism provides the following expression:

$$G_M^<(E) = iG_M\left[\Gamma_L f(E-\mu_L) - \Gamma_R f(E-\mu_R)\right], \tag{3.26}$$

where

$$\Gamma_{L/R} = i\left[\Sigma_{L/R}(E \pm eV/2) - \Sigma_{L/R}^\dagger(E \pm eV/2)\right], \tag{3.27}$$

$$\mu_{L/R} = \mu \pm eV/2. \tag{3.28}$$

Here $f(x)$ and μ indicate the Fermi function and the chemical potential, respectively.

The self-consistent calculation proceeds by first choosing a trial charge ρ^0 to calculate H_M from Eq. (3.24). Then the quantities $\Sigma_{L/R}$, $\Gamma_{L/R}$ and G_M are calculated from Eq.'s (3.20), (3.27) and (3.19), respectively. By using these quantities we can evaluate $G_M^<$ from Eq. (3.26), the density matrix ρ_M^1 from Eq. (3.25) and the new charge density ρ^1 is computed from

$$\rho^1(\mathbf{r}) = \langle \mathbf{r}|\rho_M^1|\mathbf{r}\rangle \tag{3.29}$$

This process is iterated until

$$\mathrm{Max}|\rho^j(\mathbf{r}) - \rho^{j+1}(\mathbf{r})| < \delta. \tag{3.30}$$

where $\delta \ll 1$ is the tolerance parameter.

Finally, the current can be calculated using [83]

$$I = \frac{2e}{h}\int dE\, T(E,V)[f(E-\mu_L) - f(E-\mu_R)], \tag{3.31}$$

where

$$T(E,V) = \mathrm{Tr}[\Gamma_L G_M^\dagger \Gamma_R G_M]. \tag{3.32}$$

To extract the transport properties of the extended molecule at equilibrium, i.e. at zero-bias one can add and subtract $G_M\Gamma_R G_M^\dagger f(E-\mu_L)$ to Eq. (3.26)

$$G_M^<(E) = -2i\mathrm{Im}[G_M]f(E-\mu_L) + G_M\Gamma_R G_M^\dagger\left\{\Gamma_L f(E-\mu_R) - \Gamma_R f(E-\mu_L)\right\}, \tag{3.33}$$

where

$$\Gamma_L + \Gamma_R = i[(G_M^\dagger)^{-1} - G_M^{-1}], \tag{3.34}$$

$$2i\mathrm{Im}[G_M] = G_M - G_M^\dagger. \tag{3.35}$$

Using Eq. (3.33) the density matrix can be written as the sum of two contributions

$$\rho_M = \rho_{eq} + \rho_{neq} \tag{3.36}$$

where

$$\rho_{eq} = \frac{-1}{\pi} \int dE\ \mathrm{Im}[G_M] f(E - \mu_L), \tag{3.37}$$

and

$$\rho_{neq} = \frac{1}{2\pi} \int dE\ G_M \Gamma_R G_M^\dagger \left\{ \Gamma_L f(E - \mu_R) - \Gamma_R f(E - \mu_L) \right\}. \tag{3.38}$$

ρ_{eq} can be interpreted as the density matrix at equilibrium, i.e. both reservoirs have the same chemical potential, while ρ_{neq} contains all the corrections due to the non-equilibrium conditions. The energy integration in ρ_{neq} is limited by the two Fermi functions of the leads, and therefore one needs to perform the integration only in the energy range between the two chemical potentials. In contrast the integration in ρ_{eq} is unlimited, but the integral can be performed in the complex plane using a standard contour integral technique [96], since G_M is both analytical and smooth. Despite being unbounded, in the lower part of the energy axis the integral of Eq. (3.37) only requires the inclusion of all occupied states. At energies below a certain threshold, the integrand goes to zero quite quickly. Hence we can choose a finite value for the lower limit of integration ensuring all the available states below E_F are counted.

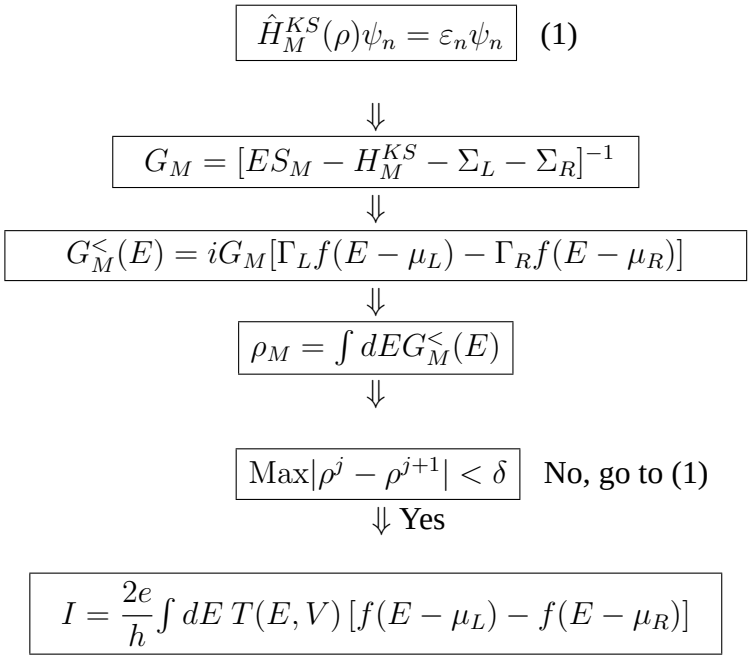

Figure 3.4: Flow chart describing the self-consistent procedure for transport calculations.

Chapter 4

TRANSPORT PROPERTIES OF METAL-METAL INTERFACES

4.1 Introduction

Our study is focused on the following metals: gold (Au), silver (Ag), copper (Cu) and aluminum (Al). Au and Ag are called noble metals because of their chemical stability; they have positive standard reduction potentials and are highly resistant to oxidation, even at elevated temperatures [97–100]. The three metals Au, Ag and Cu are called coinage metals [101] due to their former usage. Coinage metals have several applications because of their catalytic, chemical, optical, magnetic, mechanical, and electrical properties. The catalytic activity of noble metals is widely exploited in production or disposal of different chemical compounds. Coinage metals are used as catalysts in hydrocarbon conversion reactions [102] and in magnetic data storage including antiferromagnetically coupled magnetic recording media [103, 104] and magnetic random access memories (MRAMs) [104]. Aluminum and aluminum alloys are used in a wide variety of products: cans, foils and kitchen utensils, as well as parts of airplanes, rockets and other items that require a strong, light material. Although it does not conduct electricity as well as copper, it is used in electrical transmission lines because of its light weight.

The study of metallic interfaces is very important due to their catalytic and magnetic properties which are associated with modifications in electronic struc-

ture. To understand the transport properties of metallic interfaces we study in this chapter properties of:

- bulk (clean) simple metals;
- distorted interfaces which include a buckled interface plane and interface with vacancy;
- metallic and non-metallic impurities interfaces;
- metallic interlayer interfaces;
- metallic multilayer interfaces and interface alloy.

4.2 Computational Details and Structure Setup

The principal layer of the leads comprises two unit cells. Furthermore, the scattering region consists of six fcc unit cells in each case. The generalized gradient approximation (GGA) for the exchange correlation potential is employed. A mesh of a $15 \times 15 \times 100$ Monkhorst-Pack k-grid is used in the leads calculation, while a mesh of $10\times10\times1$ k-points is utilized to evaluate the transmission coefficient and current at different bias voltages. The direct diagonalization method is used to calculate the ground state wave functions. The density matrix is calculated by using up to 50 energy points on the semi-circle in the complex plane, up to 100 energy points along the line in the complex plane, and up to 50 poles in the Fermi distribution. The structures are assumed to be periodic in the xy-plane with z being the transport direction [001]. The transmission coefficient is normalized by the number of transverse k-points. In order to highlight the effects of our principal distortions, further structural relaxation effects are not taken into account. This is well justified because previous studies of Al nanocontacts have indicated only minor alterations of the bond lengths in the contact region [105].

4.3 Transport Properties of Bulk Metal

The structure for bulk (clean) metals is shown in Fig. 4.1. The sp hybrid metal Al and the coinage metals (Au, Ag, Cu) have been the object of our main study. The

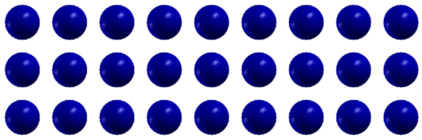

Figure 4.1: Structure under investigation: Bulk metal.

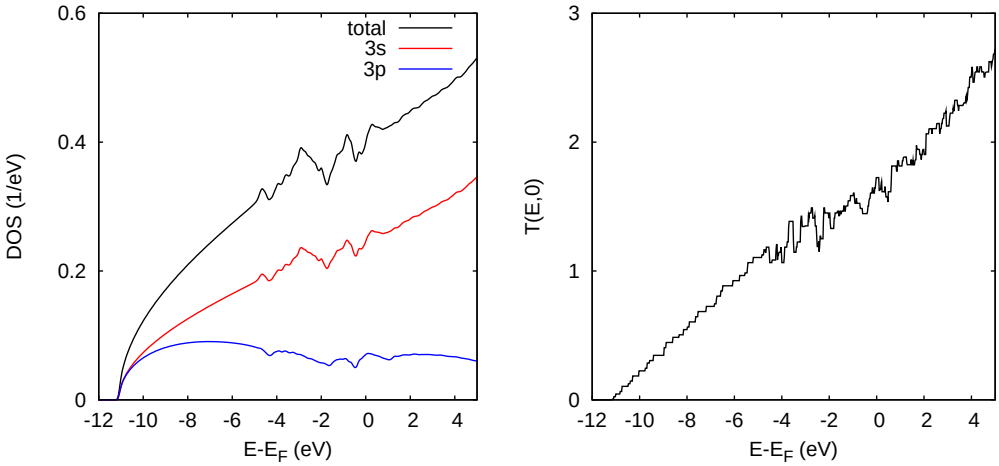

Figure 4.2: Total Al DOS (left-hand side) and transmission coefficient (right-hand side) of bulk Al [106].

pseudopotentials for coinage metals include d valance states. We use a double zeta basis set for calculating the transport properties of bulk metals.

The density of states (DOS) (see Appendix D) and transmission coefficient $T(E, V = 0)$ of Al are displayed in Fig. 4.2. Aluminum is a good example of a sp hybrid metal with the $3s^2 3p^1$ valence state. The s band prevails above -10 eV (see Fig. 4.2, left-hand side). The total and partial, i.e. the angular projected, densities of states are related to the nearly free electron model, since DOS is proportional to the square root of the energy [107]. $T(E_F, V = 0)$, right-hand side of Fig. 4.2, can be interpreted if we compare it with DOS. The onset point for transmission coefficient and density of states is the same. This means that the transmission starts when electronic states are available above -11.0 eV (onset point). The $T(E, V = 0)$ is closely related to the DOS shape so one can explain $T(E, V = 0)$ by using nearly free electron model, i.e. $T(E) \sim E$ [106].

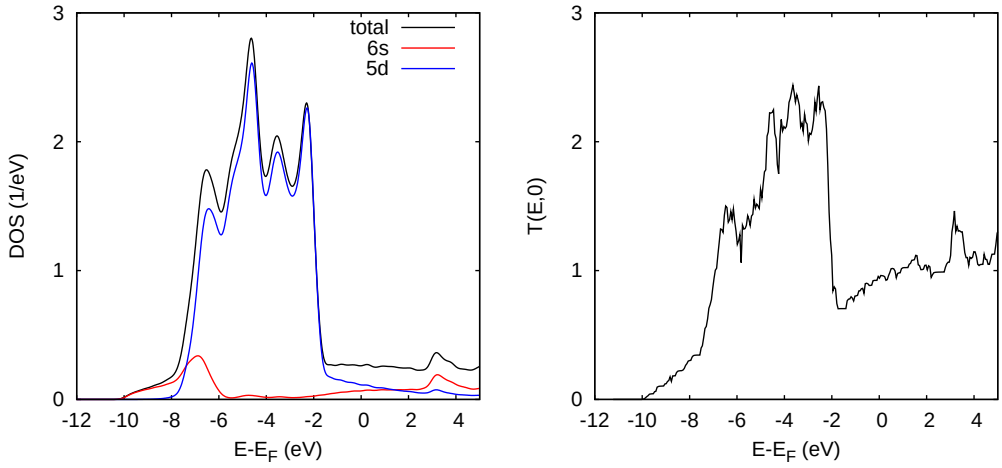

Figure 4.3: Total Au DOS (left-hand side) and transmission coefficient (right hand side) of bulk Au [106].

The quantitative evaluation of the transmission coefficient yields for the conductance $G = G_0 \cdot T(E_F, V = 0)$, with $G_0 = 2e^2/h$, values of about 1.5 G_0 for Al. In metallic conductors, the transmission probability is produced from many channels, so $T(E, V = 0)$ is larger than one.

We discuss now the electronic structure and equilibrium transport properties for coinage metals. From Fig. 4.3, left-hand side, the substantial deviations from the free electron behaviour appear in the vicinity of the Fermi energy. The deviations are due to the appearance of flat d bands which are more localized. Also the s band dominates below -5 eV and d dominates in the energy range -7 eV $< E - E_F < -2$ eV. Although the d states are filled, the d band lies within the occupied region of the conduction band (sp band) and perturbs its otherwise nearly free electron character. Right-hand side of Fig. 4.3 demonstrates that the transmission coefficient reflects the DOS shape. The starting point of $T(E_F, V = 0)$ is near -10 eV and high values appear in the energy range -8 eV $< E - E_F < -2$ eV. We find that the transmission increases linearly with increasing energy in the vicinity of the Fermi energy. The conductance value for Au is 1 G_0 [106].

The density of states and transmission coefficient for other coinage metals Ag and Cu are similar to Au [106], since they have a very similar valence electronic structure: fully occupied d states at about -2 eV below the Fermi level and a

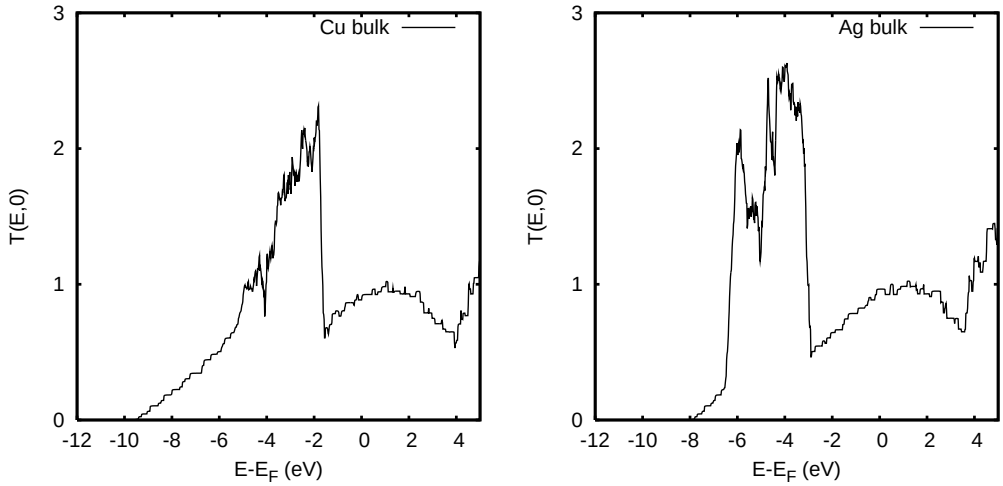

Figure 4.4: Transmission coefficient of bulk Cu (left-hand side) and bulk Ag (right-hand side) [106].

single s valence electron (with substantial sd- hybridization) as shown in Fig. 4.4. The transmission starts near -9.5 eV and -8 eV for Cu and Ag respectively. There is no change for the conductance of the Au, Cu, and Ag. The width of d band transmission for Au is about -6 eV whereas the width of transmission is about -4 eV and -3.5 eV for Cu and Ag bulks, respectively, see Fig. 4.3 and Fig. 4.4. These widths are related to the width of the bulk DOS of Au $5d$, Cu $3d$ and Ag $4d$ bands.

Turning to the non-equilibrium properties, i.e. the influence of applied voltage on the transmission coefficient, in general the application of a potential bias across a homogeneous metallic conductor does not produce a potential drop. This corresponds to the known fact that a pure metal cannot sustain an internal electric field. Nevertheless it is interesting to investigate how an artificially imposed potential drop affects the transport properties of clean and defective interfaces [106]. This gives us an indication on how the system responds to an external electrical perturbation. Within SMEAGOL it is possible to impose such a potential drop by simply setting the difference between the chemical potentials of the leads to eV, in such a way that a potential drop of V is artificially established across the scattering region. Note that the resulting external electric field then depends on the length of the scattering region itself. With this in mind we have re-calculated

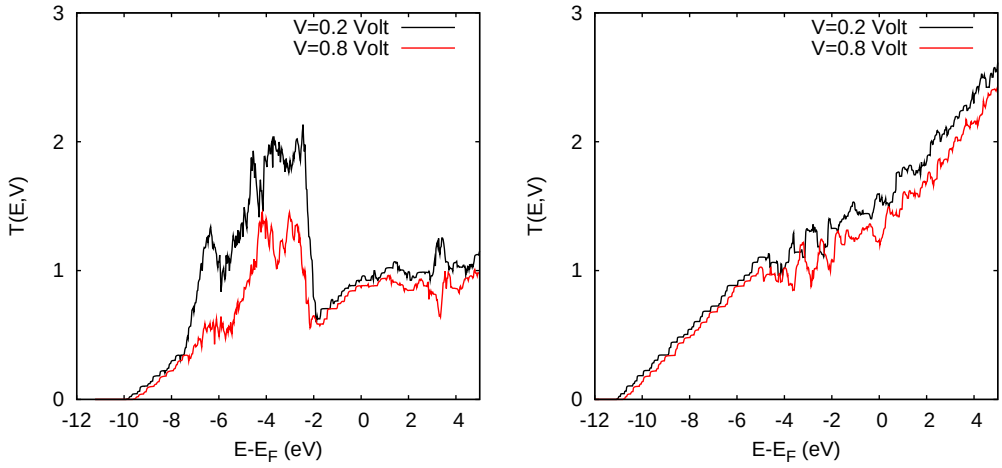

Figure 4.5: Transmission coefficient of Au bulk (left-hand side) and Al bulk (right-hand side) interfaces at voltages of 0.2 Volt and 0.8 Volt [106].

the transmission coefficient as a function of energy for different imposed potential drops. The results are shown in Fig. 4.5, where we use the same convention as for the $V = 0$ case to plot $T(E, V \neq 0)$ with the energy scale measured relative to the equilibrium E_F.

Since the external potential V disturbs the periodicity of the electronic states along the transport direction, a reduction of $T(E, V \neq 0)$, as compared to $T(E, V = 0)$, is expected. This expectation is partially confirmed in the case of bulk Au (see the left-hand side of Fig. 4.5), for which $T(E, V = 0.8V)$ is reduced by 40% with respect to $T(E, V = 0)$ in the energy range corresponding to the Au $5d$ density of states, and by $\approx$ 10% well above the Fermi level. In contrast, the suppression of the transmission coefficient is much smaller for bulk Al interface (see the right-hand side of Fig. 4.5), amounting to $\approx$ 10% above -4 eV. Below this energy, we have no reduction at all. Of course, this observation finds its origin in the free electron character of the Al electronic states below -4 eV, with the same explanation applying to the Au data at the low energy edge and around E_F. Since for both the Al and Au interfaces the value of the transmission coefficient at E_F is hardly modified by the external potential, little changes in the conductivity are predicted in the linear response [106].

The calculated I-V characteristics obtained by artificially imposing the poten-

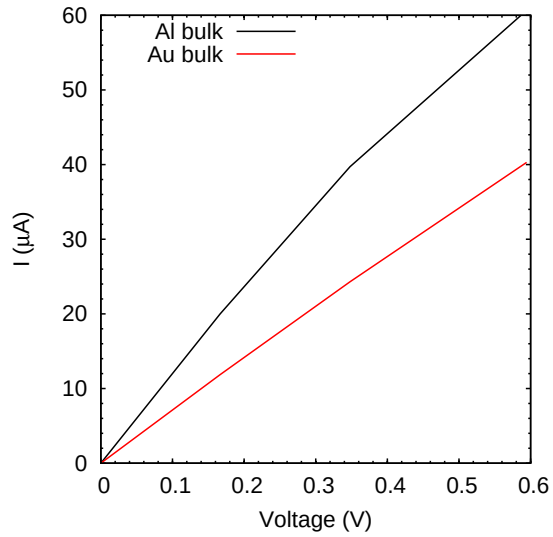

Figure 4.6: I-V characteristics for Au bulk and Al bulk [106].

tial drop are presented in Fig. 4.6 and support this conjecture [106]. The I-V characteristics seem almost perfectly linear. To close this section we have remarked that the non-equilibrium properties for Cu and Ag are similar to Au [106].

4.4 Transport Properties of Buckled and Vacancy Interfaces

A buckled interface means that we shift the neighbouring interface atoms zigzag-like by 10% of the fcc lattice constant along the [001] direction. The vacancy configuration is created by removing each second interface atom. It therefore models a series of mono-atomic contacts. The structure of buckled interface and interface with vacancy are displayed in Fig. 4.7. The transport properties of buckled interface is studied for Au only and the influence of the interface with vacancy on the transmission coefficient is studied for Al, Au, Cu, and Ag.

The distorted interface by vacancies for sp-hybrid Al system (see Fig. 4.8) reduces the transmission coefficient by 40% with respect to the values of Al bulk. This suppression does not depend on the energy [106]. Also, the onset point is shifted about 1 eV towards the Fermi energy. Interestingly, the linear slope of

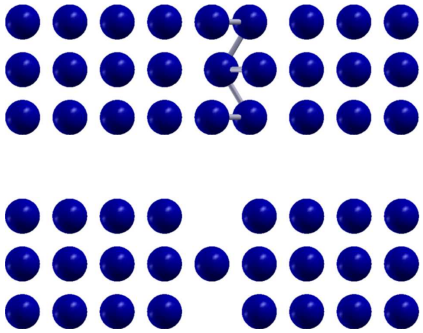

Figure 4.7: Structures under investigation: Buckled interface (top) and interface with vacancy (bottom) [106] .

$T(E, V = 0)$ below -4 eV is not reproduced by the vacancy calculation. We attribute this fact to a strong perturbation of the Al electronic structure near vacancies, which can be traced back to a reduced isotropy of the chemical bonding and, therefore, a suppression of the sp-hybridization [105]. Next the transmission coefficients of the interface with vacancy and the buckled interface for Au are addressed (see Fig. 4.9). We find also a clear decrease of transmission in the whole energy range [106]. The amplitude of the transmission, at around -4 eV, is reduced by 55% as compared to the bulk system. For $E - E_F > -2$ eV the reduction is less pronounced, amounts to 25%. An interface buckling has a similar effect [106], as illustrated on the right-hand side of Fig. 4.9. In particular, almost the same reduction of the transmission coefficient is observed below -2 eV, whereas in the energy range from -2 eV to 5 eV it is significantly smaller, amounting to 15%. This finding can be attributed to the well-known differences in the localization of the Au electronic states below and above -2 eV. We finally mention that the conductance of buckled interfaces is larger than the conductance of interfaces with vacancy. The onset of $T(E, V = 0)$ already appears at -10 eV, while it is found at -8 eV for the vacancy system.

For the influence of vacancies on the Cu and Ag, the reduction of the transmission with vacancy interfaces is the same [106]. The onset point of transmission coefficient for these elements is moved ≈ 1 eV towards the Fermi energy, see Fig. 4.10. The I-V characteristic for buckled interfaces and interfaces with vacancy

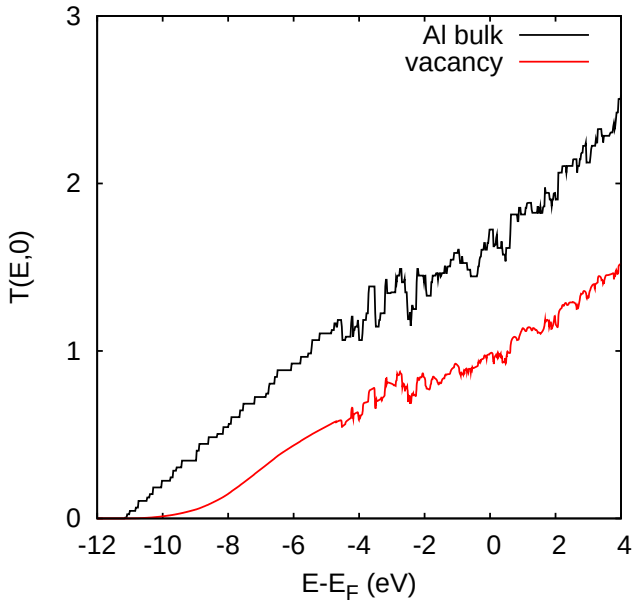

Figure 4.8: Transmission coefficient of the Al interface with vacancy, compared to the corresponding bulk [106].

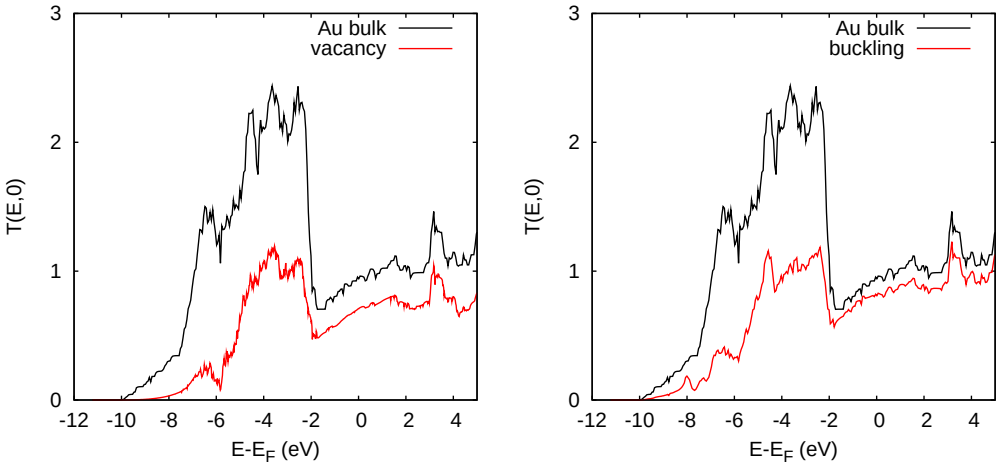

Figure 4.9: Transmission coefficient of the Au interface with vacancy (left-hand side) and the buckled interface (right hand side), compared to bulk Au [106].

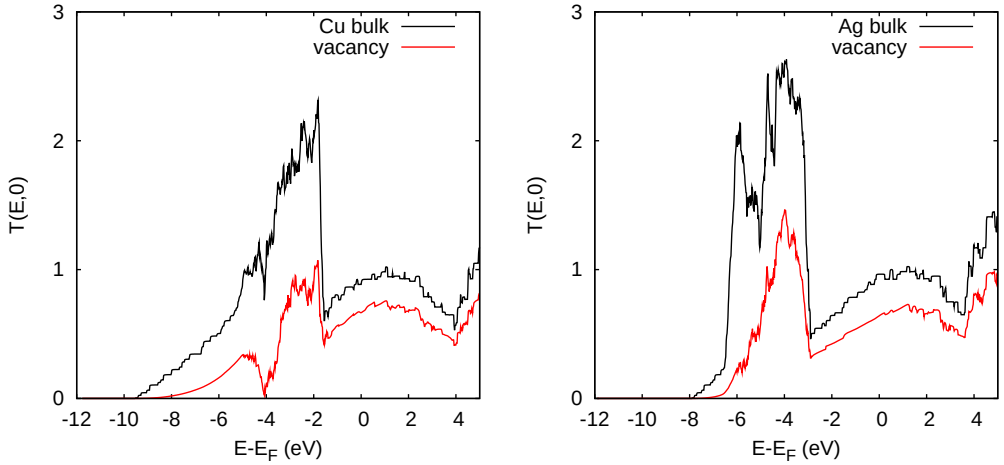

Figure 4.10: Transmission coefficient of the Cu (left-hand side) and Ag (right-hand side) interface with vacancy, each compared to the corresponding bulk interface [106].

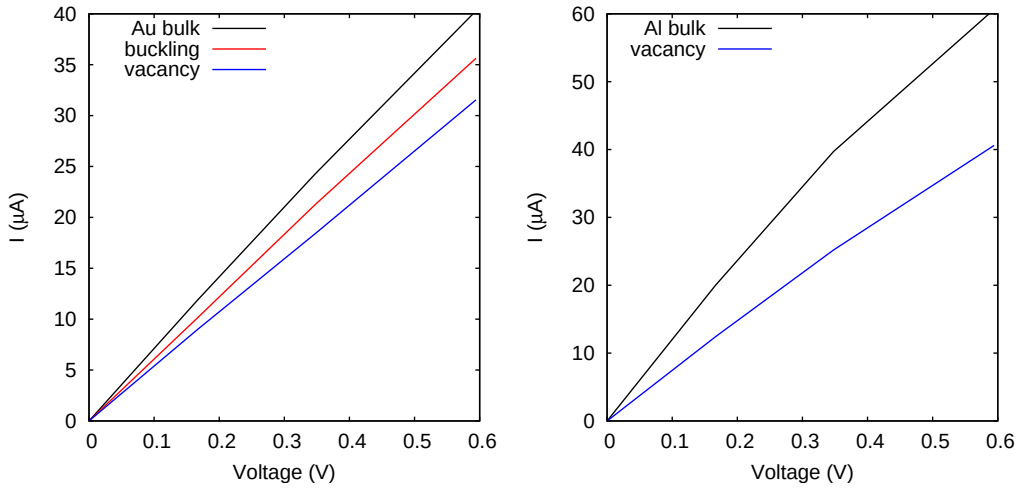

Figure 4.11: Left-hand side: I-V characteristics for the bulk Au interface and the Au interface with buckling, and Au interface with vacancy. Right-hand side: I-V characteristics for the bulk Al interface and the Al interface with vacancy [106].

shows linear characteristic (see Fig. 4.11). The suppression of the transmission coefficient is proportional to the reduction of the conductance, extracted from these I-V [106], amounting to 25% for the vacancy systems and to 15% for the buckled interface, with respect to the bulk values.

4.5 Transport Properties of Different Impurities and Interlayer Interfaces

Impurity systems are generated by replacing each second interface atom by an impurity atom (Si, Cu, Mg, S, Ni, Ag), see the structure in Fig. 4.12. The valence electrons are described by a single zeta basis set. In the first step in this section we compare the effects of non-metallic and metallic impurities. As non-metallic impurities we consider Si (electronic configuration $3s^2 3p^2$, chemically inert) and the chalcogen S (electronic configuration $3s^2 3p^4$) which are typical impurities found in Au. Crystalline Si and S are insulators. In Fig. 4.12 we compare between the effect of Si and the effect of impurities on the transmission coefficient $T(E)$ and also show corresponding data for a vacancy system; compare to our previous section (Fig. 4.9, left-hand side). The conductance obtained for the three systems shows rather similar values close to $G = 0.6 \cdot G_0$, where $G_0 = 2e^2/h$. Just below the Fermi energy E_F the transmission coefficient grows almost linearly with the energy, reflecting a delocalized nature of the related states. In addition, the reduction of the transmission due to the impurities in the energy range from -6 eV to -2 eV, where the Au $5d$ states dominate, is similar in all three cases [108]. Since the d bands are more sensitive to local disorder [109], the reduction here is much stronger than near E_F. Minor differences between the three systems in Fig. 4.13 concern the lower band edge. Below -8 eV (s-like Au) $T(E)$ is suppressed

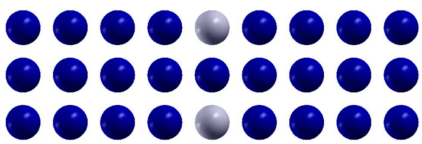

Figure 4.12: Structure under investigation: Interface with impurity.

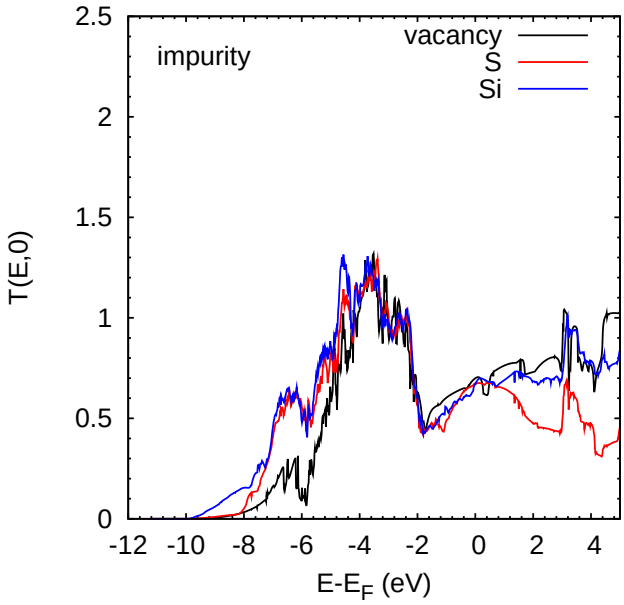

Figure 4.13: Transmission coefficient of the interfaces with S and Si impurities, compared to the interface with a vacancy [108].

for both the S impurity and the vacancy. Between -8 eV and -6 eV (s- and d-like Au) the impurities do not reproduce the reduction of $T(E)$ as found for vacancies. For the Si impurity the transmission coefficient starts at -10 eV due to Au-Si hybridization. Apart from that, non-metallic impurities resemble the effects of vacancies even quantitatively [106].

Turning to the metallic impurities Cu, Mg, and Ni, firstly we discuss the comparison between the transmission coefficient of Au bulk and interface with Cu impurity. Fig. 4.14 shows that due to the stronger localization of the Cu $3d$ orbitals, the transmission is reduced by 40% below -2 eV, with respect to bulk Au interface. In contrast, we find no reduction for the higher energy itinerant states. Moreover the shift of the onset point is very small. These calculations (for Cu) are completed by using a double zeta basis set. The comparison between the calculations using single zeta basis set and that using double zeta basis set are shown in Fig. 4.15. The difference between them does not affect our study. Now for Mg and Ni impurities, Mg is a metal which can be described by a nearly-free

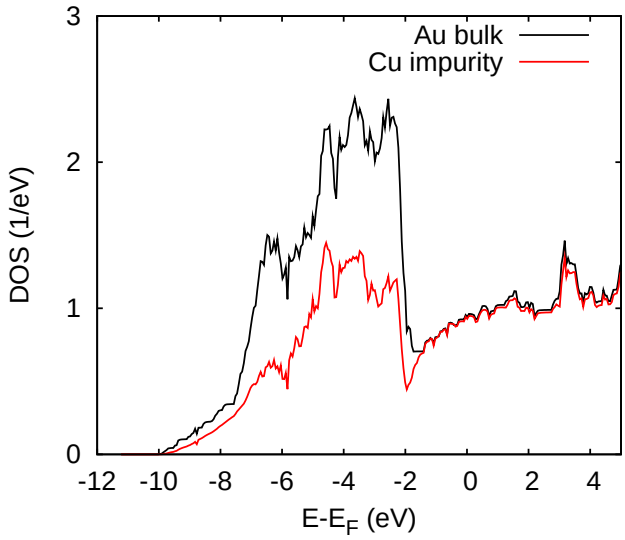

Figure 4.14: Transmission coefficient of the Cu impurity system, compared to the bulk Au interface [106, 108].

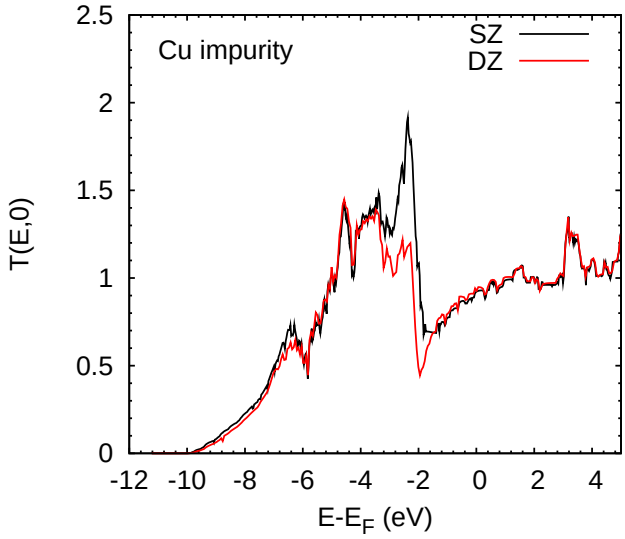

Figure 4.15: Transmission coefficient of the interfaces with Cu impuritie by using single zeta (SZ) and double zeta (DZ).

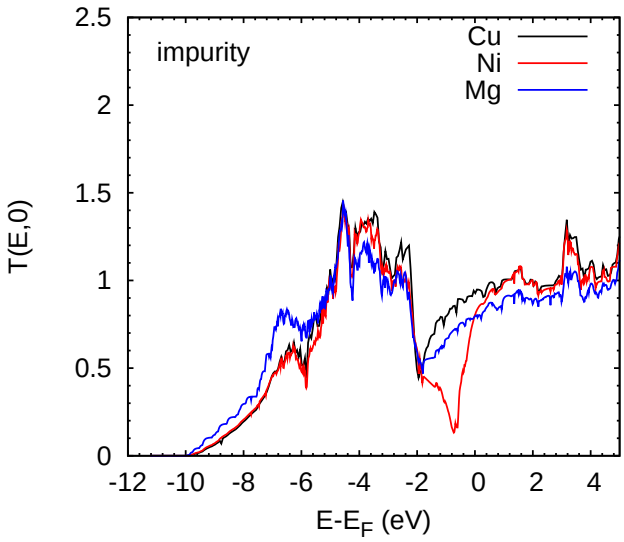

Figure 4.16: Transmission coefficient of the interfaces with Cu, Ni, and Mg impurities [108].

electron model. Ni and Cu, on the other hand, are transition metals with narrow d-bands. Despite this different physical nature of the three metals, they behave rather similar when acting as impurities in Au [108], see Fig. 4.16. The onset of $T(E)$ is found at -9.5 eV and the conductance is $\sim 0.8 \cdot G_0$. Also, the reduction of $T(E)$ in the Au $5d$ dominated energy range is comparable. The only difference is the pronounced dip in $T(E)$ obtained for the Ni impurity near E_F. While the Ni $3d$ states are located at about -1 eV [110], i.e. in the energy range of the Au sd-hybridized states, the Cu $3d$ states appear at about -2 eV, i.e. in the Au $5d$ dominated energy range. Thus, only the Ni $3d$ states can interact with the Au s-d hybride states and form d-d hybride states. The Au $6s$ states, in turn, hybridize with the Ni $4s$ states and shift to much lower energies. As a consequence, the transmission is strongly reduced in the vicinity of the Fermi energy [108].

The I-V characteristics of systems with Cu, Mg, and S impurities are compared in Fig. 4.17. We find the highest conductivity for Cu, since in this case the electronic structure of the impurity is closely related to that of the Au host. When the states deviate more but the impurity is still metallic, see Mg, the conductivity is reduced but not as much as in the case of a non-metallic impurity, see S [108].

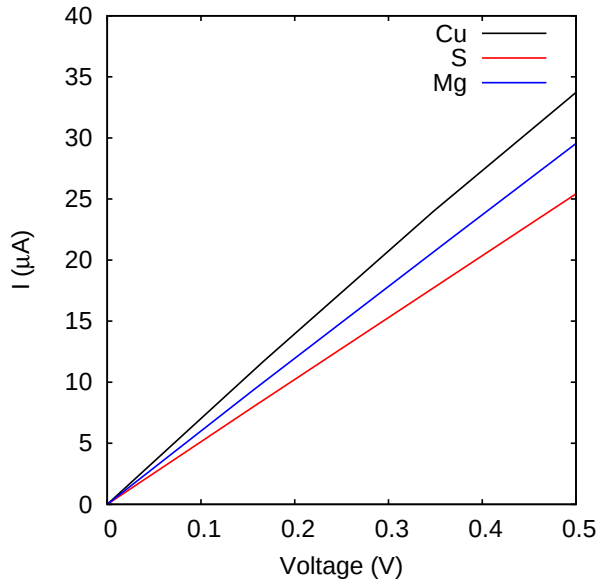

Figure 4.17: I-V characteristics of the interfaces with Cu, S, and Mg impurities [108].

We next compare full impurity interlayers of Cu, Ni, and Ag, which all crystallize in a fcc structure. Fig. 4.18 displays the structure of the interlayer system. The noteworthy reduction of the transmission appears below -2 eV for Cu interlayer with respect to the transmission of the bulk Au [108]. However $T(E, V = 0)$ above 1 eV is not varied. The transmission starts at -9 eV (see Fig. 4.19). In addition, the lattice constant and valence electronic structure of Ag are very similar to Au. The transmission mediated by the Au $5d$ states usually is smaller in interlayer than in impurity systems, while both the onset of $T(E)$ and the conductance agree very well. The transmission coefficients of Cu, Ni, and Ag interlayer systems are depicted in Fig. 4.20. In order to understand the high values of $T(E)$ in the Ag case, as compared to Cu and Ni, we address the related densities of states (DOS): Since the Cu and Ni $3d$ bands are very narrow, they do not hybridize with the Au states and the Au $5d$ transmission consequently is significantly reduced. In contrast, Ag has $4d$ states in the whole energy range between -8 eV and -2 eV and therefore strongly hybridizes with the Au host. Furthermore, the reduced transmission between -2 eV and the Fermi level in the case of the Ni interlayer

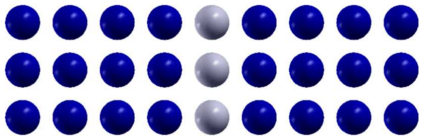

Figure 4.18: Structure under investigation: Interface with metallic interlayer [108].

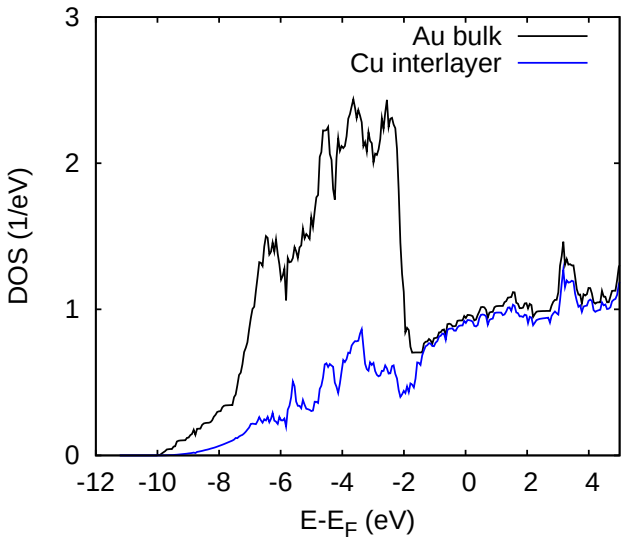

Figure 4.19: Transmission coefficient of the Cu interlayer system, compared to the bulk Au interface [106, 108].

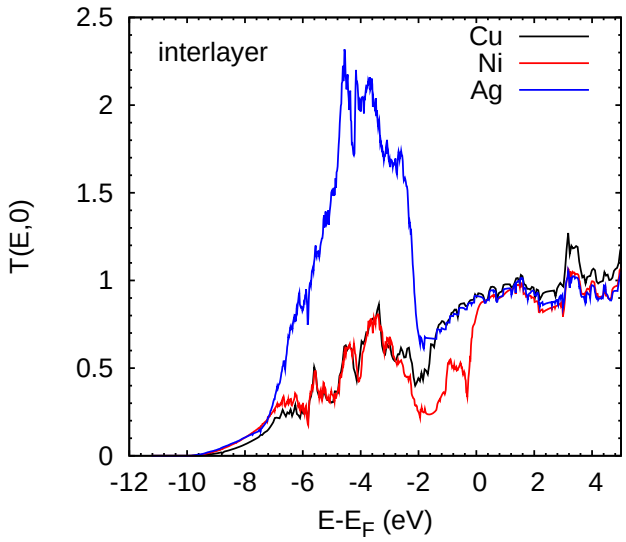

Figure 4.20: Transmission coefficient of the Cu, Ni, and Ag interlayer systems [108].

system has the same origin as discussed before for the Ni impurity [108].

4.6 Transport Properties of Multilayers and Interface Alloys

Artificially made metallic multilayers form a class of material allowing for the combination and optimization of physical properties. With the advance of multilayer synthesizing techniques these new materials have become an important subject for both fundamental and technical studies. As a consequence the number of metallic multilayer systems rapidly increases with the development of theoretical interest. On the other hand the electronic structure of alloys have been extensively studied experimentally and theoretically [111, 112]. An alloy is a metal formed from an intimate combination of two or more elements [113].

In this section we deal with various modifications of the interlayer system. First, we discuss the influence of an increasing interlayer thickness (multilayers). Second, we consider interlayers which are not atomically sharp but show interface

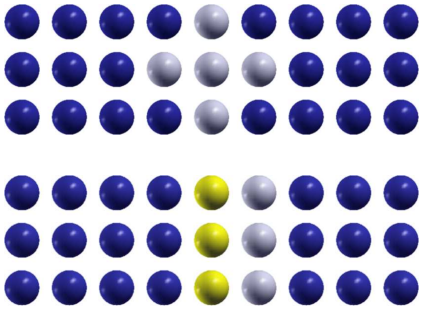

Figure 4.21: Structures under investigation: Interface alloy (top), and two-component interlayer (bottom). Blue, gray, and yellow spheres indicate Au, Ag, and Cu atoms, respectively.

alloy formation. Third, we investigate two-component interlayers. The interface alloy and two-component structures are shown in Fig. 4.21.

The influence of the interlayer thickness is studied for Au/nAg/Au heterostructures with n Ag monolayers. According to Fig. 4.22 the conductance of the system decreases with growing n, where no saturation is found up to $n = 8$. In addition, the shape of $T(E)$ is closely related to the shape of the bulk DOS of the two-component. In the case of a single interlayer, $T(E)$ resembles the DOS of the Au host. Therefore, a linear increase of $T(E)$ between -10 eV and -8 eV (Au s states) and a high transmission in the energy range of the Au $5d$ states are observed. With increasing n, however, the shape of $T(E)$ is given by the bulk Ag DOS. Since the width of the bulk Ag $4d$ bands ($\sim$ 3.5 eV) is smaller than the width of the Au $5d$ bands ($\sim$ 6 eV), the broad peak in $T(E)$ narrows with growing n. In fact, for $n = 8$ the Ag $4d$ band width reappears. The starting point shifts towards the Fermi energy by increasing n. In addition, at the transmission maximum around -4 eV the amplitude is suppressed strongly for growing n because of the localized nature of the d states. On the contrary, the reduction of the conductance is much less pronounced, amounting to 4% at $n = 4$ and 16% at $n = 8$ with respect to the $n = 1$ value. Finally, we note that these results are specific for the Au/nAg/Au system and may change for other systems, since they depend on details of the electronic structures of the component materials [108].

It is known that alloys can be formed at metallic interfaces [114]. We address this issue by comparing the $n = 2$ interlayer system to a configuration with alloy

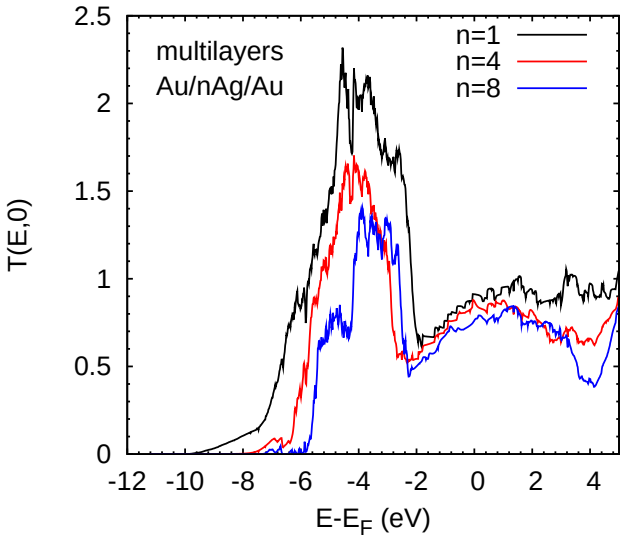

Figure 4.22: Transmission coefficient of the Ag interlayer system for interlayer thicknesses of $n = 1, 4$, and 8 [108].

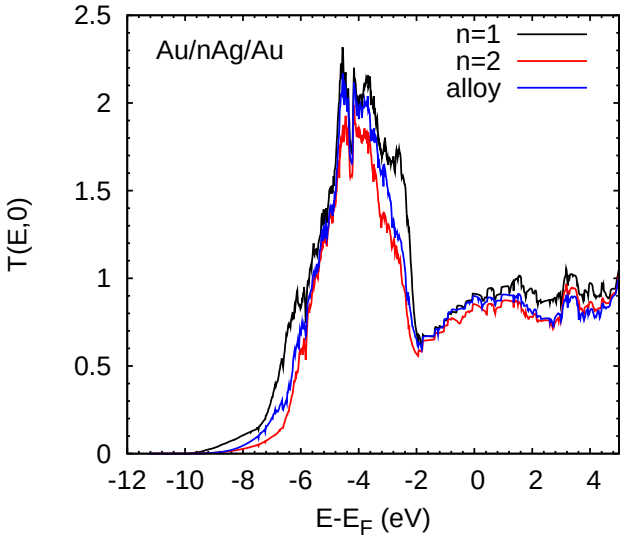

Figure 4.23: Transmission coefficient of the interface alloy, compared to the $n = 1$ and $n = 2$ interlayer system [108].

layers next to a single Ag interlayer, see the first structure of Fig. 4.21. Both systems comprise the same number of Ag atoms. According to Fig. 4.23, the transmission is slightly reduced as compared to the $n = 1$ curve, which traces back to the additional impurities, and, analogously, is higher than the double Ag layer. Moreover, it is worth mentioning that the alloy formation affects $T(E)$ almost uniformly in the studied energy range [108].

As seen before, the electronic structure of the impurity/interlayer material strongly influences $T(E)$. This becomes even more critical when multiple interlayers of different materials are considered, as we shall demonstrate for the Au/AgCu/Au heterostructure, which we compare to the Au/AgAg/Au heterostructure in Fig. 4.24. Since the conductance is reduced neither for the Au/AgAg/Au heterostructure nor for a single Cu interlayer, see Fig. 4.19, it is not surprising that the conductance of the two-component interlayer system also resembles the Au host. The suppression of the transmission below -2 eV is due to the narrow Cu $3d$ bands, see our earlier discussion. It is even larger than a single Cu interlayer, since the Ag-Cu interface results in a further localization of these states. The shape of $T(E)$ of the two-component interlayer system again can be interpreted as a superposition of the component effects [108].

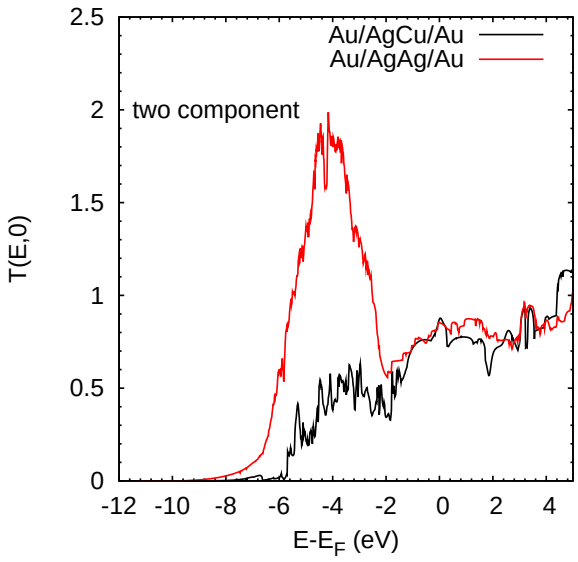

Figure 4.24: Transmission coefficient of the Au/AgCu/Au heterostructure, compared to the Au/AgAg/Au [108].

Chapter 5

TRANSPORT PROPERTIES OF METAL-INSULATOR-METAL HETEROSTRUCTURES

5.1 Introduction

Physical and chemical properties of metal/oxide heterostructures are of great interest because these systems have such different properties that they find wide technological applications such as structural materials, photovoltaic devices, heterogeneous catalysis, coating and sensors [115, 116]. On the other hand, metal/oxide insulators serve as tunneling barriers in several nanodevices and therefore they have to be extremely thin to guarantee sufficiently large currents at low applied voltage. Various metal/MgO (001) interfaces have been studied, both experimentally [117–122] and theoretically [123–133]. From the experimental point of view, significant progress has been achieved in the determination of the atomic structure of ceramic-metal interfaces, particularly by high resolution electron microscopy [134] and atom probe field ion microscopy [135]. Furthermore, spatially resolved electron energy loss spectroscopy is able to elucidate the electronic structure of ceramic-metal interfaces [136].

An understanding of the geometric and electronic structure in the interfacial region between the metal and the oxide at an atomic scale is vital to ensure a continued and controlled improvement of these materials and of their use in different

technological devices.

Magnesium lies very close to being a free-electron-like metallic solid with only a very weak bulk crystal potential. The valence band electronic structure is expected to closely resemble a free-electron-like parabola. In contrast, magnesium oxide is close to an ideal insulating ionic solid with a valence band structure dominated by the strong potential of the ionic cores. The different chemical bonding and electronic structure exhibited by these two systems provides an opportunity to test the applicability of theoretical models to two extreme examples of the solid state. MgO has been more widely studied both experimentally [137–139] and theoretically [140–142] compared to metallic magnesium.

Electronic structure calculations of metal/MgO interfaces have been performed with a variety of methods at various levels of theory. Finite-cluster models of the metal/MgO interfaces were studied using both Hartree-Fock (HF) [126] and DFT [128, 133] methods. An embedded cluster method was applied using a DFT approach [143]. Periodic slab calculations have mainly used different DFT methods [124, 125, 127, 131, 132, 144] based on either the local density approximation (LDA) or the generalized gradient approximations (GGA) using either full-potential methods such as full potential linear muffin-tin orbital (FLMTO) and full-potential linearized augmented- plane-waves (FLAPW) or pseudopotential plane-wave methods (PP-PW). Despite many differences between the aforementioned calculations, several general conclusions can be drawn. Nobel metal adhesion on the oxide substrates occurs mainly due to interaction between the d and O $2p$ energy bands. The formation of the bond across the interface seems to be caused by a complex charge redistribution in the Ag layer [130] but not very much charge transfer or orbital overlap occur.

The last decade has witnessed further progress in information technology, which was initialized by two fundamental discoveries being closely connected to the magnetism in ultrathin magnetic layers. The discovery of the phenomenon of interlayer exchange coupling in 1986 by P. Grünberg and Co-workers [145] and the giant magnetoresistance (GMR) effect in 1988, by the groups of P. Grünberg and A. Fert [24, 25] mark the advent of the field of spin-based electronics (spintronics), in which magnetism and solid state electronics are joining to exploit spin-dependent transport processes [146]. The GMR effect is based on the arrangement of two successive magnetic layers, separated by a very thin non-magnetic layer.

The tunnel junctions with ferromagnetic metals like Fe-MgO-Fe heterostructure often are considered a prototypical metal-insulator-metal system. This hetrostructure is of great importance in spintronics [146]. Therefore it has been subject to intensive experimental and theoretical research, see [147] and the references given therein.

Point defects in oxides determine the optical, electronic, and transport properties of the material. A detailed understanding and a control at atomistic level of the nature (and concentration) of point defects in oxides are therefore of fundamental importance to synthesize new materials with well-defined properties. Before point defects could be created in controlled conditions, they have to be known in all aspects of their physical properties. The accurate theoretical description of the electronic structure of point defects in oxides is essential for the understanding of their structure properties relationship. In a broad classification, one can recognize at least 12 major kinds of point defects. We focus on defects due to vacancies in MgO. Experimentally, vacancies have been found on the surfaces of Au nanoparticles embedded in MgO [148]. Beyond, defects have been observed on the [001] surface of ultrahigh vacuum cleaved single MgO crystals [149]. Since Au can form a chemical bond with defects [150], the Au-vacancy interaction must be taken into consideration when modeling Au-MgO heterointerfaces [151]. Practically, the most often observed defects in MgO are oxygen vacancies. Once the vacancies are formed, their electronic structures could be changed by adding or removing electrons in them [149].

Oxygen vacancies are usually called color or F centers from the German word for color, Farbe. V centers indicate Mg vacancies. The vacancies can have different formal charges. For example, the removal of a neutral O atom results in a neutral F center; the removal of an O^- ion in an F^+ center (paramagnetic); the removal of an O^{2-} ion in an F^{2+} center. The subscripts distinguish a surface F center, F_S, from the bulk counterpart, F. The neutral O vacancies are generally stable in bulk MgO [152]. O and Mg vacancies appear not only in MgO bulk crystals but especially accumulate at interfaces [153].

A basic property of polar Au/MgO interfaces is the termination. The Au/MgO interface can in principle be terminated by an O (i.e. O on top of Au) or by a Mg (i.e. Mg on top of Au) layer Experimentally, the oxygen termination appears to be strongly preferred.

In this chapter we discuss:

- the transport through clean Au-$(MgO)_n$-Au heterostructures, where n indicates the number of unit cells, is of great interest. It is therefore our aim to analyse the dependence of the current on structural details;
- the dependence of the transport properties of the heterostructure on the thickness of the MgO interlayer;
- the influence of the interface spacing on transport properties of the heterostructure;
- F centers in MgO, which appear at the interface and in the bulk of the heterostructure.

5.2 Computational Method and Structural Setup

We construct the Au-MgO-Au supercell by sandwiching an MgO layer, which is $n = 1$, 2, or 3 fcc MgO unit cells thick (i.e., 3, 5, or 7 MgO monolayers), between two semi-infinite fcc Au [100] electrodes. The junctions are assumed to be periodic in the xy-plane with z being the transport direction. To study the transport properties we consider two configurations of the Au-MgO-Au junction: Either the interface Au atoms lie on top of O (conf. I) or on top of Mg (conf. II). Figure 5.1 displays the structure for conf. I. Due to a 3% lattice mismatch between Au and MgO we have to introduce a minor lattice strain by setting the MgO lattice constant to the Au value $a_{\mathrm{Au}} = 4.09$ Å instead of $a_{\mathrm{MgO}} = 4.2$ Å. For the Au-MgO distance, i.e. the interface spacing, we study values of $d = 2.05$, 2.5, and 3.06 Å. All calculations were performed using the local density approximation (LDA) approach and a minimal basis set (simple zeta, SZ), analogous to related studies [154].

The system properties were converged with respect to $15\times15\times100$ k-points in the leads calculation, while a mesh of $10\times10\times1$ k-points is used to evaluate the transmission coefficient and current at different bias voltages. To determine the density matrix, we choose up to 16 energy points on the real axis and 16 energy points on both the semi-circle and the line in the complex plane. In addition, 16 poles in the Fermi distribution are employed.

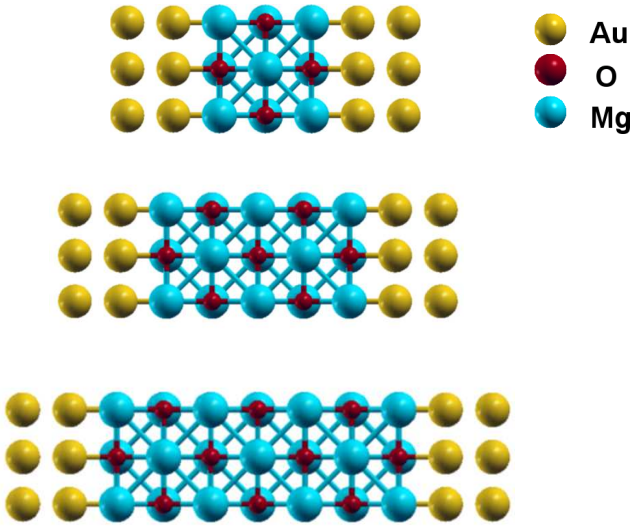

Figure 5.1: Heterostructures under investigation (from top to bottom): $n = 1, 2, 3$ unit cells of MgO sandwiched between Au leads. The O-terminated interface (conf. I) is shown.

We have thoroughly checked our electronic structure results of bulk MgO and bulk Au by comparing them to data from previous studies. In particular, the band gap of MgO is found to be 5.16 eV (see Fig. 5.2), which agrees well with the theoretical values reported in Refs. [155] and [156], but is lower than the experimental value of 7.8 eV [157] due to the underestimation of band gaps by the local density approximation. Fig. 5.2 shows that O $2p$ states dominate in the energy range -7.8 eV $< E - E_F < -2.4$ eV. However Mg $3s$ states dominate at energies higher than 2 eV. One can notice that the overlapping between Mg an O states appears at -6.5 eV.

5.3 Charge Transport through the Clean Junction

We first study the electronic structure of conf. I (O-terminated) at an interface spacing of $d = 2.05$ Å. To this aim, we analyse the projected density of states (PDOS) (see Appendix D), see Fig. 5.3. On the left-hand side, the PDOS of

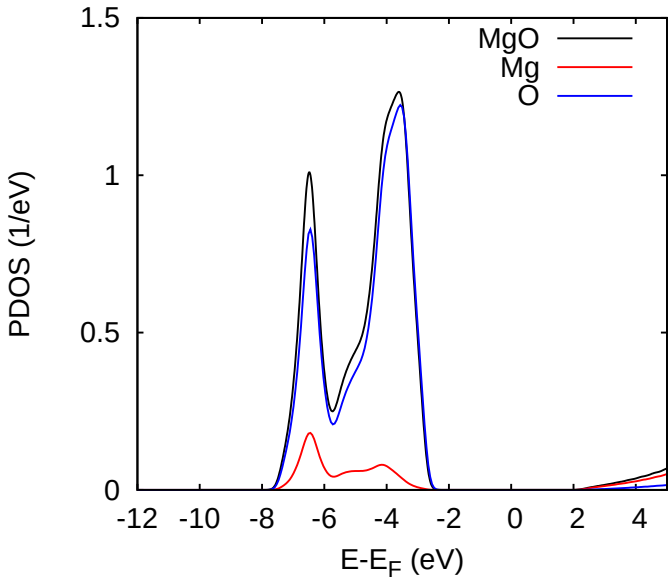

Figure 5.2: DOS of bulk MgO [158].

atoms right at the interface is plotted for the $n = 1$ system. A strong hybridization between the Au and MgO states is evident. As compared to bulk MgO, additional interface states due to Au-O bond are found near the lower MgO band edge at -8 eV and at -4 eV [131]. Thus, formation of an interface Au-O bond is evident at energies -9 eV, -8 eV and at -4 eV. At -9 eV one can see the overlap between the Au, Mg, and O states. The hybridization between O and Mg still appears near -6 eV and new hybridization occurs at -9 eV. Au induced gap states fill up the MgO band gap and leave the interface metallic. The onset point of PDOS for this structure is -10 eV for all atoms. This starting point is similar to the corresponding one of the leads Au (see Fig. 4.4 Chapter 4). The occupied states in the energy range between -10 and -2 eV are O $2p$ dominated, whereas the Mg $3s$ states dominate at energies higher than 1 eV. So the position of occupied states are shifted if we compare between them and the position of the occupied states of bulk MgO (see Fig. 5.3). The band gap does not appear in the PDOS of the O atoms at interface [158]. The PDOS calculated for O and Mg atoms in the center of the interlayer turns out to be bulk-like even for the thin $n = 1$ interlayer, see the right-hand side of Fig. 5.3. When the thickness of the MgO layer increases to $n = 2$ the

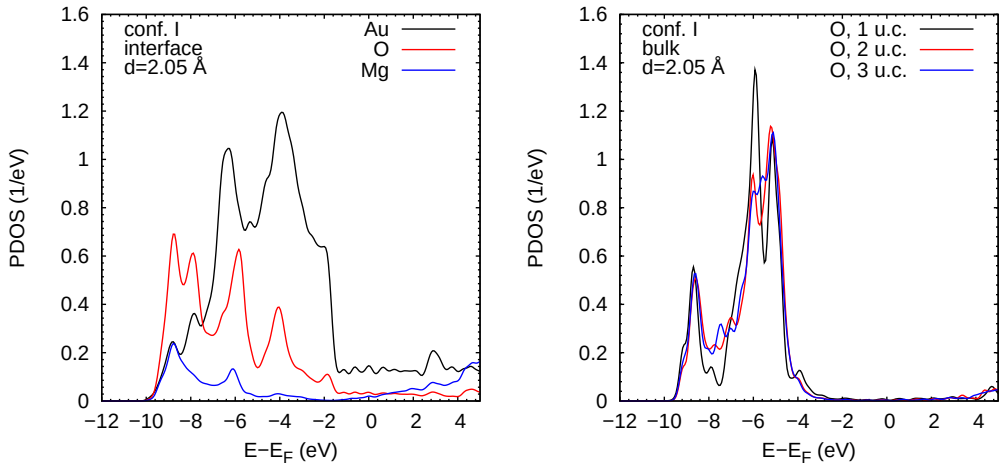

Figure 5.3: Projected DOS of atoms at the interface for $n = 1$ (left-hand side) and of O atoms in the center of the MgO interlayer for $n = 1, 2, 3$ (right-hand side) [158].

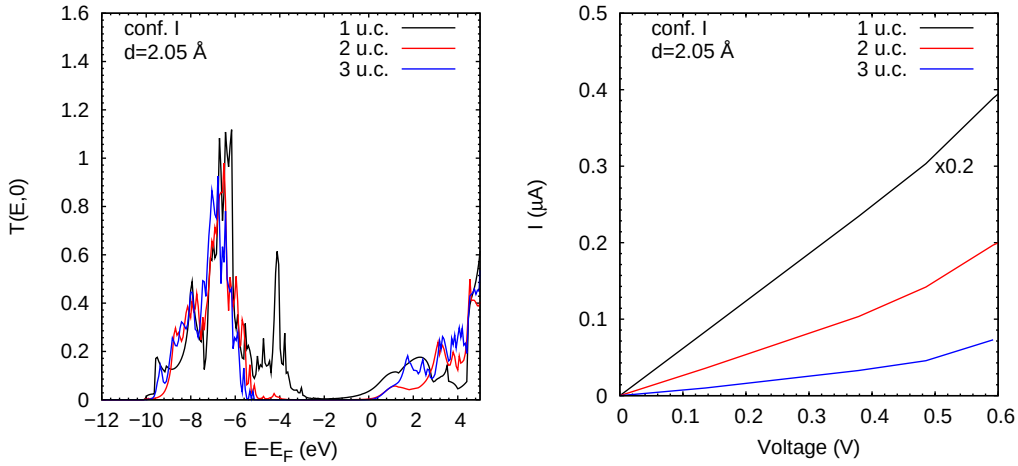

Figure 5.4: Transmission coefficient (left-hand side) and I-V characteristic (right-hand side) for $n = 1, 2, 3$ [158].

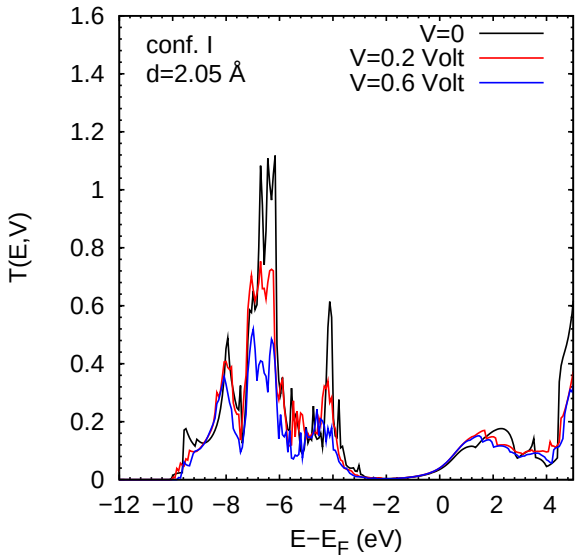

Figure 5.5: The dependence of transmission coefficient on applied voltage [158].

peaks at -8 and -4 eV, reminiscent of the Au-O bonding, vanish. While distinct differences are visible in the PDOS of the central MgO layer for $n = 1$ and $n = 2$, the result for $n = 3$ largely resembles the $n = 2$ PDOS. The PDOS of the bulk atoms of O and Mg shows that there is band gap [158]. Corresponding transport data are shown in Fig. 5.4. For low energies of -10 to -6 eV the shape of the transmission coefficient as a function of the energy, $T(E, 0)$, is closely related to the PDOS of the central MgO layer, see the right-hand side of Fig. 5.3. However, the transmission vanishes at about -5.5 eV although there is a significant PDOS up to -4 eV for all systems under investigation. Only for the $n = 1$ interlayer transmission is found up to about -3 eV, where the transmission peak at -4 eV is related to the interface states. The Au induced gap states lead to a remarkable transmission at the Fermi energy in the $n = 1$ case. Since they cannot penetrate into the center of thicker MgO interlayers, the transmission at the Fermi energy is drastically reduced in these cases [158]. The transmission gap for $n = 1$ is about 2 eV and increases to 4 eV for $n = 2$. For $n = 3$ the change of the value of transmission gap is very small with respect to corresponding one of $n = 2$.

The I-V characteristic therefore shows a much higher conductance for $n = 1$

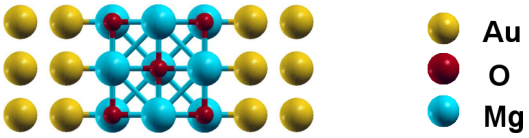

Figure 5.6: Heterostructures under investigation: The Mg-terminated interface (conf. II) is shown [158].

than for $n = 2, 3$; note the scaling factor of 0.2.

Figure 5.5 shows the dependence of transmission coefficient on the applied voltage, $T(E, V)$, for $n = 1$. There is no change in the behaviour of transmission coefficient with increasing applied voltage such as at the Fermi energy and the band gap [158]. However around -6.8 eV the height of $T(E, V)$ is reduced by 32% for $V = 0.2$ Volt and by 51% for $V = 0.6$ Volt as compared to $V = 0$.

Turning to conf. II (Mg-terminated), the structur is displayed in Fig. 5.6. No Au-MgO bond is established since hybridized states are missing in the PDOS, see Fig. 5.7. There is no state for O and Mg below -8 eV and we can not see hybridization between Au and MgO above -8 eV. The effect of no bond between Au-MgO appears also on the starting point of the PDOS. The starting point for O and Mg PDOS appears at -8 eV which is different from the starting point of Au (-10 eV). The Au induced gap states reappear around the Fermi energy and again a reduced band gap is found for the interface Mg states [158]. The O PDOS of the central MgO layer is similar for $n = 2$ and $n = 3$ but deviates slightly in the $n = 1$ case. Moreover, with the interlayer thickness the Mg-O hybridization increases and the PDOS peaks become more pronounced. A minor shoulder due to the Au induced gap states is present at -1.8 eV for $n = 1$ but disappears for the thicker MgO interlayers. The onset point of DOS of O and Mg atoms in the bulk is like the corresponding one at the interface. Due to the weak coupling to the metal, the shape of $T(E, 0)$ in Fig. 5.8 again resembles the PDOS of bulk MgO. The starting point of transmission coefficient corresponds to the starting point of PDOS of O and Mg at the interface and bulk. We find that the conductance of the tunnel junction in conf. II is smaller than that obtained for conf. I [158]. With increasing thickness of the MgO interlayer, d_{MgO}, it decreases nicely exponentially, $G = T(E_F) \propto \exp(-d_{\mathrm{MgO}}/1.41\ \text{Å})$, see the logarithmic plot in

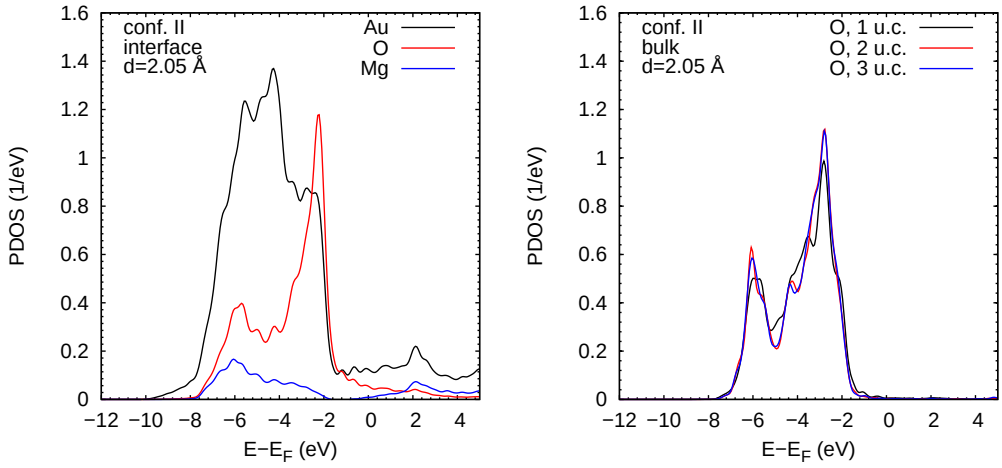

Figure 5.7: Projected DOS of atoms at the interface for $n = 1$ (left-hand side) and of O atoms in the center of the MgO interlayer for $n = 1, 2, 3$ (right-hand side) [158].

Fig. 5.8. The influence of applied voltage on the transmission coefficient, for $n = 1$, are shown in Fig. 5.9. The effect appears only in the energy range -7.8 eV $< E - E_F < -2$ eV, where the reduction of the height of transmission coefficient increases as the applied voltage increases. We observe that the reduction of the height of $T(E, V)$ by increasing the applied voltage for the tunnel junction in conf. II is less than obtained for corresponding one in the conf. I. The starting point of the transmission coefficient shifts by $eV/2$ towards the Fermi energy as increasing V.

In a next step, we study the influence of the interface spacing on the charge transport through the Au-MgO-Au junction. As an example, we consider conf. I for $n = 1$. The left-hand side of Fig. 5.10 shows the PDOS for interface atoms at an interface spacing of $d = 3.06$ Å. The data resemble the PDOS of the Mg-terminated system at $d = 2.05$ Å, see Fig. 5.7. We can not see any overlap between Au, O, and Mg states. One hybridization between O and Mg states appears at -5 eV. In particular, there is no sign of an Au-O bond. Therefore, we find that an Au-MgO distance of about 3 Å is sufficient to fully suppress the Au-O bonding. The starting point of PDOS of O and Mg (-6.2 eV) differs from the starting point of the Au (-9.6 eV) [158]. The O PDOS of atoms in the central MgO layer

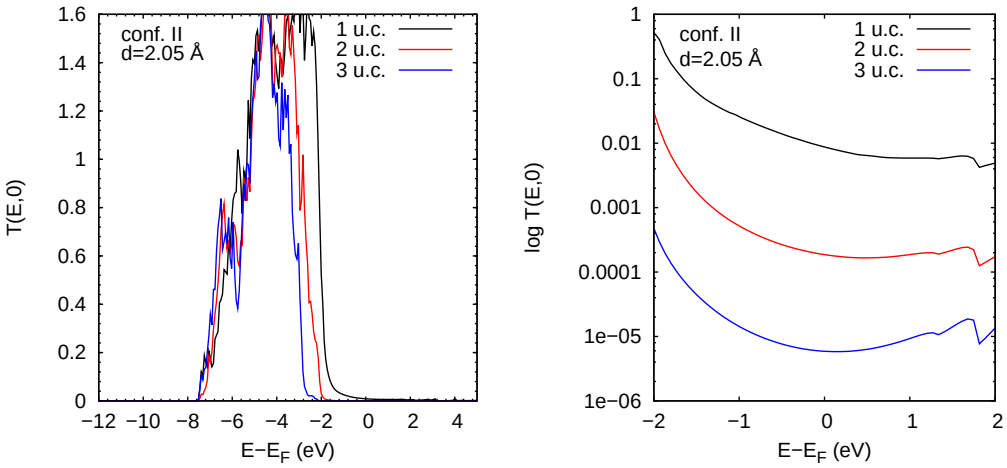

Figure 5.8: Transmission coefficient for $n = 1, 2, 3$. A logarithmic plot of the data in a reduced energy range is shown on the right-hand side [158].

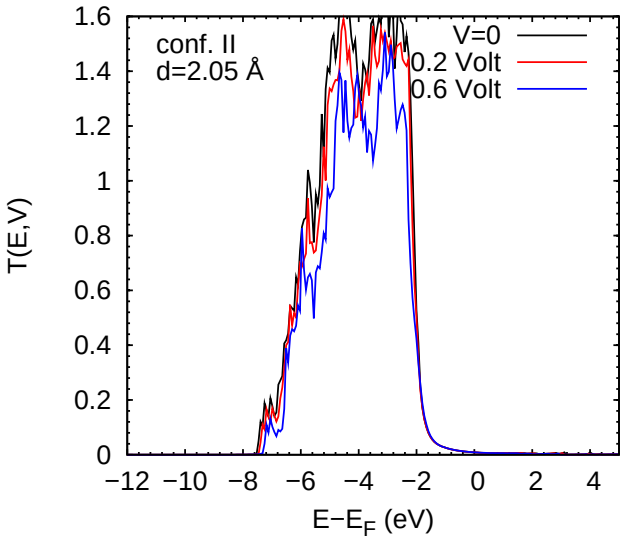

Figure 5.9: The dependence of transmission coefficient on applied voltage [158].

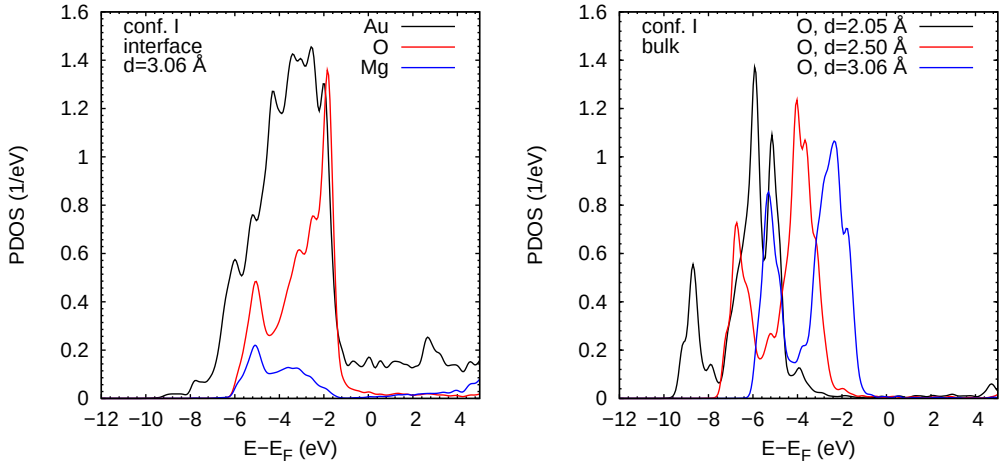

Figure 5.10: Projected DOS of atoms at the interface spacing $d = 3.06$ Å for $n = 1$ (left-hand side) and of O atoms in the center of the MgO interlayer at different values of the interface spacing for $n = 1$ (right-hand side) [158].

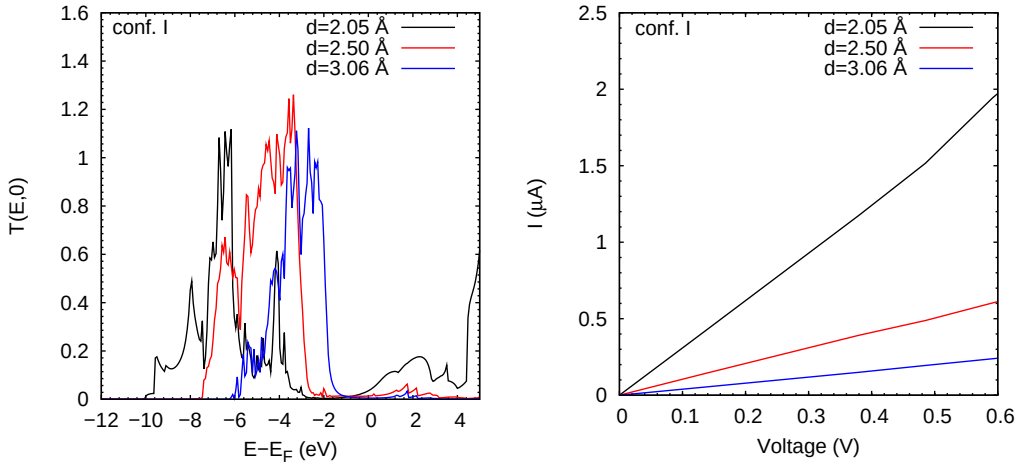

Figure 5.11: Transmission coefficient (left-hand side) and I-V characteristic (right-hand side) at interface spacings of 2.05 Å, 2.50 Å, and 3.06 Å for $n = 1$ [158].

at different interface spacings is compared on the right-hand side of Fig. 5.10. It has been found theoretically that the stable Au-MgO distance is $d = 2.5$ Å [151]. In this case the PDOS turns out to be similar to both bulk MgO and conf. II at $d = 2.05$ Å, see Fig. 5.7. The band width amounts to ~ 6 eV, while it is ~ 7 eV for the shorter spacing. As to be expected, it decreases further to ~ 5 eV for $d = 3.06$ Å. The rigid band shift with growing interface spacing is connected to the fact that the interface becomes more and more surface-like [158].

Fig. 5.11 addresses the transport at different interface spacings. Both the onset and the shape of $T(E, 0)$ are determined by the corresponding PDOS, see the right-hand side of Fig. 5.10. Above the Fermi energy as the interface spacing increases the transmission coefficient decreases. Furthermore, the I-V characteristic in Fig. 5.11 demonstrates that the conductance is exponentially suppressed when the interface spacing increases [158].

5.4 Effects of O Vacancies

The effect of vacancies is discussed subsequently for conf. I and an interface spacing of $d = 2.05$ Å. We study the following configurations: An interface O vacancy, a symmetric vacancy generated by removing an O atom from the center of the MgO interlayer, an asymmetric vacancy located at 1/4 of the MgO interlayer (for $n = 2$), see Fig. 5.12, and a situation with two vacancies located at 1/4 and 3/4 of the MgO interlayer (for $n = 2$).

For the Au-MgO-Au junction with $n = 1$ and an interface vacancy the PDOS of the interface atom is shown on the left-hand side of Fig. 5.13. As compared to the clean system, see Fig. 5.3, vacancy induced Mg states in the energy range between -2.4 and -0.4 eV are created. Therefore, the energy gap in the Mg states has vanished. Since the vacancy induced Mg states and the Au induced gap states are located in the same energy range they are difficult to separate. Au-O bonds do not appear in this case where the vacancy breaks these bonds. We show on the right-hand side of Fig. 5.13 the PDOS of atoms in the central MgO layer. The vacancy induced Mg states are clearly visible [158]. We find Mg states dominates at energies higher than -1 eV where we can not see that in the clean system, see right-hand side of Fig. 5.3. When we change the position of vacancy to become a symmetric vacancy the PDOS of the interface atoms is displayed on the left-hand

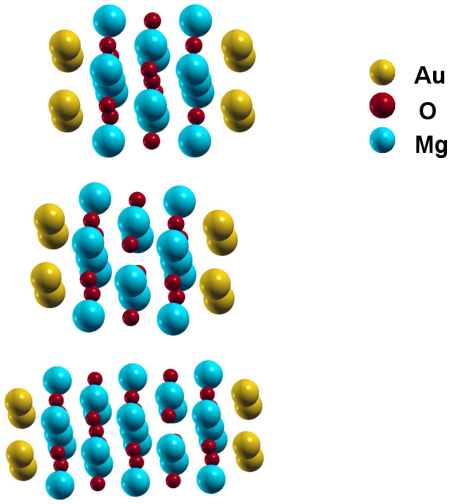

Figure 5.12: Heterostructures under investigation (from top to bottom): An interface O vacancy, a symmetric vacancy in $n = 1$ unit cell and an asymmetric vacancy in $n = 2$ unit cell, respectively. The O-terminated interface (conf. I) is shown.

side of Fig. 5.14. Also the vacancy induced Mg states are produced between the energy range -2.4 and -0.4 eV. The main difference as compared to the interface vacancy system, see right-hand side of Fig. 5.12, is that the contribution of vacancy induced Mg states in this case is more than in the case of interface vacancy above -4 eV [158]. The transmission of the Au-MgO-Au junction with $n = 1$ is enhanced by the incorporation of the interface and symmetric vacancy as compared to the clean system, see Fig. 5.15. The starting point of the transmission coefficient of the interface vacancy case is similar to the starting point of the symmetric vacancy case, -9.5 eV, which is different from the onset point of the clean case, where the vacancies break some bonds as we discussed before. The conductance of the symmetric system (0.4 G_0) is higher than the conductance of the interface system (0.2 G_0). Moreover, the transmission coefficient shows that the induced Mg states at the energies above -3 eV for the symmetric vacancy system is more than interface vacancy system [158]. Enhancement of the transmission therefore depends on both the position of the vacancies and interface spacing. The influence of the interface spacing in O-deficient systems is shown in

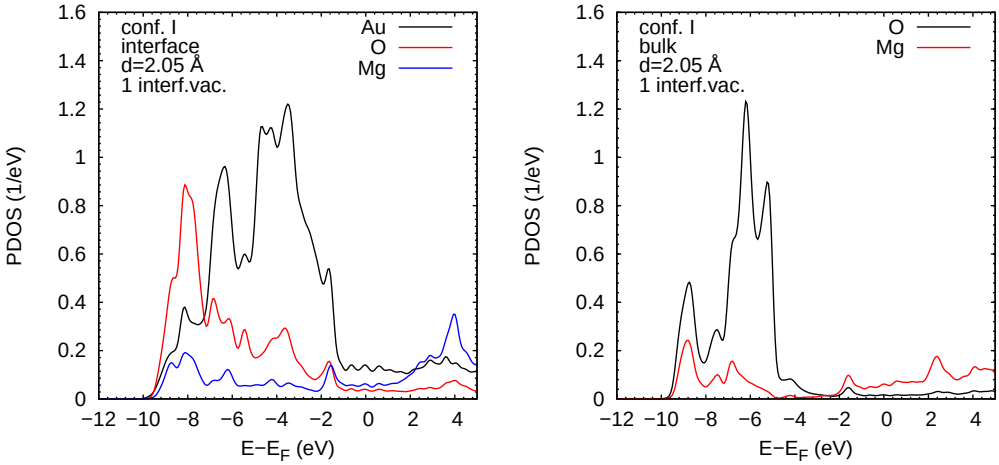

Figure 5.13: Projected DOS of atoms at the interface (left-hand side) and in the center of the MgO interlayer (right-hand side) for $n = 1$ and an interface vacancy; $d = 2.05$ Å [158].

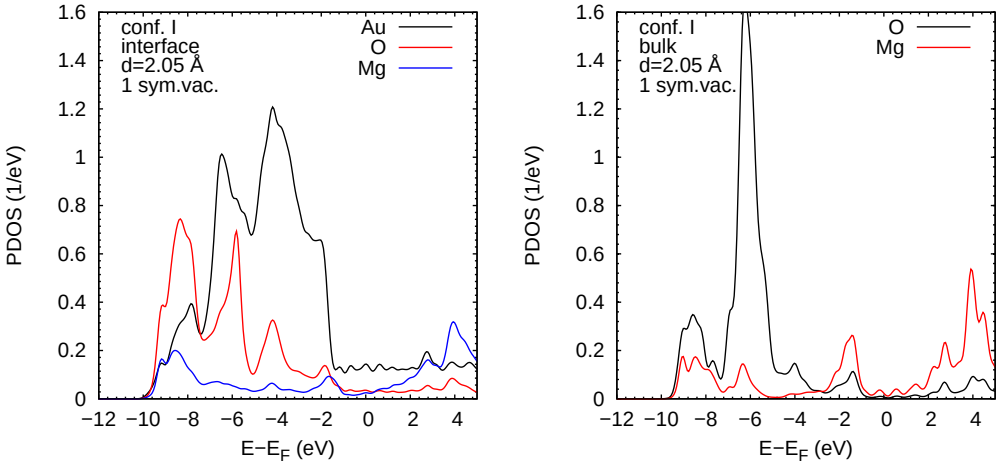

Figure 5.14: Projected DOS of atoms at the interface (left-hand side) and in the center of the MgO interlayer (right-hand side) for $n = 1$ and a symmetric vacancy; $d = 2.05$ Å [158].

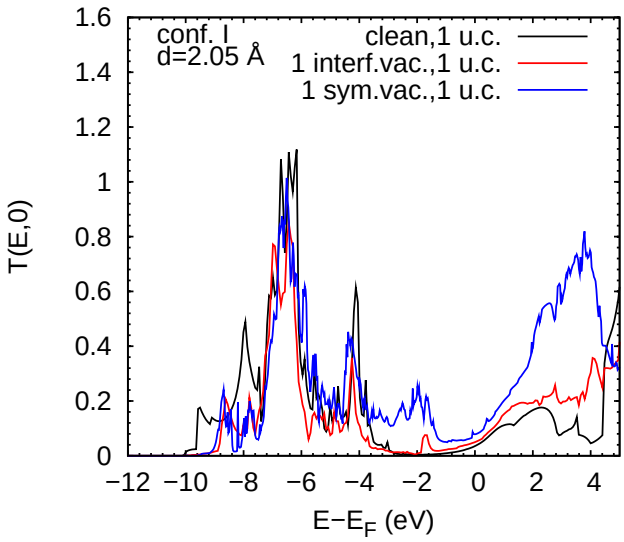

Figure 5.15: Transmission coefficient for $n = 1$ and various vacancy configurations at and $d = 2.05$ Å [158].

Fig. 5.16. Corresponding PDOS data for atoms at the interface and in the central MgO layer, we find that the vacancy induced Mg states now are located close to the Fermi energy, which further enhances the conductance [158]. The onset point of the O and Mg states appears at -7.5 which is different from the onset point in the case of clean with interface spacing 3.06 Å (see Fig. 5.10) and a symmetric vacancy with interface spacing 2.05 Å (see Fig. 5.14). Further enhancement of the transmission can be achieved by introducing a second vacancy, for $n = 2$, which is illustrated by the $T(E, 0)$ data in Fig. 5.17. The vacancy induced Mg states are produced between the energy range -3 and -2 eV. An asymmetric vacancy, in contrast, has almost no effect. Therefore the enhancement of the transmission depends on the density of vacancies [158]. I-V characteristic reflects the effect of various vacancies configurations on the conductance, see right-hand side of Fig. 5.17.

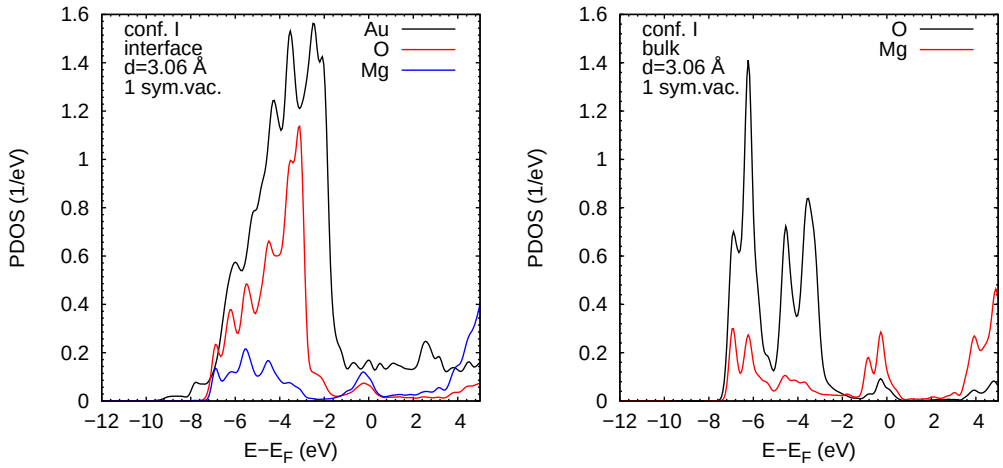

Figure 5.16: Projected DOS of atoms at the interface (left-hand side) and in the center of the MgO interlayer (right-hand side) for $n = 1$ and a symmetric vacancy; $d = 3.06$ Å [158].

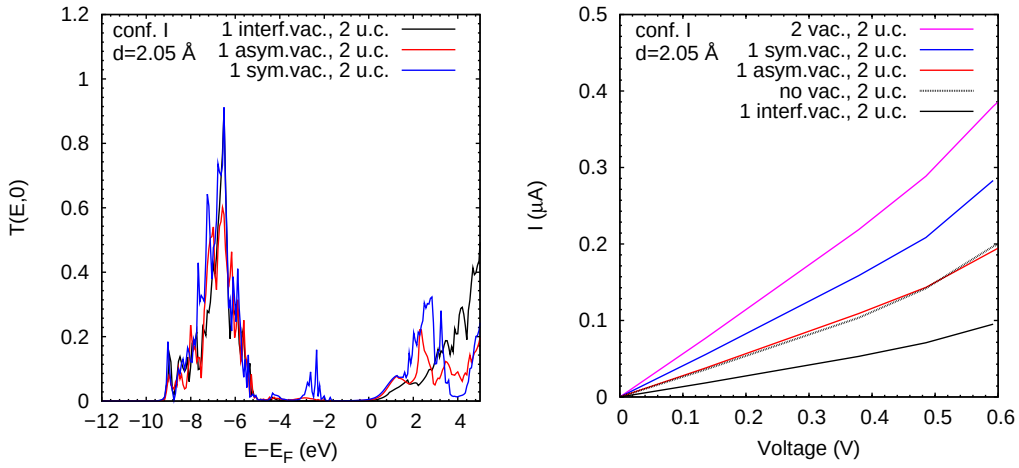

Figure 5.17: Transmission coefficient (left-hand side) and I-V characteristic (right-hand side) for $n = 2$ and various vacancy configurations [158].

Chapter 6

SUMMARY AND CONCLUSION

The details of metal-metal and metal-oxide interfaces have a strong influence on the electronic structure of the junction. The understanding of these details is crucial from a basic scientific point of view. We have calculated the transport properties of metal-metal and metal-oxide interfaces using ab initio calculations in the framework of DFT and non-equilibrium Green's function. This study was done by using the SMEAGOL package.

We have confirmed the capability of SMEAGOL to deal with extended systems. The transport through smooth and distorted fcc Al, Cu, Ag, and Au interfaces has been addressed, where we particularly have identified regimes of (nearly) free electrons. We find that the shape of $T(E, V = 0)$ is closely related to the DOS shape. Investigating various kinds of distortions, we find that vacancy sites have a huge effect on $T(E_F, V = 0)$. Buckling of the interface atomic layers reduces the transmission strongly when localized Cu, Ag, and Au d states are involved. A relevant reduction of $T(E_F, V = 0)$ is also found for (nearly) free electrons. The electronic states at the Fermi energy have been affected by this distortion but there is no change in the electronic configurations. In contrast, insertion of impurities with electronic configurations similar to the host compound does not reduce the conductance of the device. A full impurity interlayer drastically suppresses transmission via directed d bonds, while $T(E_F, V = 0)$ again is hardly altered.

The transmission coefficient of non-metallic impurity systems has the same behaviour as the transmission coefficient of vacancy system, since these systems

do not contribute to the electronic states at the Fermi energy. In the case that an impurity, interlayer, or interface alloy resembles the Au electronic structure, its incorporation alters the transmission only marginally. However, when distinct bonds are formed between the contaminant and the Au host the transmission can be strongly affected. We find only a minor interdependence between multiple modifications, i.e. their cumulative effect is well described in terms of a superposition of the individual effects. The influence of the layer thickness depends on the details of the electronic structures of the component materials. For our specific system, Au/nAg/Au, the conductance decreases as n increases.

We have also studied the transport properties of Au-MgO-Au tunnel junctions. In particular, we have investigated the influence of the thickness of the MgO interlayer, the interface termination, and the interface spacing. As to be expected for tunnel junctions, an exponential decay of the conductance as a function of the interlayer thickness is found when the interface is Mg-terminated. Additional interface states appear in the O-terminated configuration due to the formation of Au-O bonds, modifying the exponential behaviour. An increasing interface spacing suppresses the Au-O bonding and the transmission becomes independent of structural details. The Au induced gap states are found to be similar in both terminations. Moreover, the conductance decreases exponentially with the interface spacing, since the Au-MgO coupling becomes weaker. The latter is reflected by a rigid band shift of the MgO states towards the Fermi energy.

Our results confirm that O vacancies lead to additional states within the MgO band gap and, therefore, can enhance the conductance of the junction. The effect of symmetric vacancies turns out to be much larger than found for asymmetric vacancies. Moreover, the conductance can be enhanced by increasing the vacancy concentration (the number of vacancies per unit cell). In contrast to a clean junction where a growing interface spacing always yields a reduction of the conductance, the rigid band shift of the MgO states here transfers the vacancy induced states to the Fermi energy, which can be used to enhance the conductance in O deficient systems.

As a consequence, we have identified two main mechanisms which determine the conductance of Au-MgO-Au junctions: (i) Introduction of O vacancies increases the transparency of the MgO interlayer due to the creation of additional electronic states close to the Fermi energy. (ii) The interface spacing then can

be used to fine-tune these states and, therefore, to fine-tune the conductance. Although the interface coupling is a very efficient parameter, it is difficult to control in the experiment.

Appendix A

HISTORY OF EXCHANGE-CORRELATION FUNCTIONALS

A.1 Local Density Approximation

The effective potential in the Kohn-Sham Hamiltonian Eq. (2.20) includes the external potential and the effects of the Coulomb interactions between the electrons, e.g. the exchange and correlation interaction. In principle, it also includes the difference in kinetic energy between the fictitious noninteracting system and the real system. In practice, however, this difference is ignored in many modern functionals as the empirical parameters appear, which necessarily introduces some kinetic-energy correction if they are based on experiment [159]. Modeling the exchange and correlation interactions is necessary within KS DFT as the exact functionals for exchange and correlation are not known except for the homogeneous (uniform) electron gas. However, approximations exist that permit the calculation of real systems. The simplest approximation is the local-density approximation (LDA), based upon the exact exchange energy for a uniform electron gas, which can be obtained from the Thomas-Fermi (TF) model, and from fits to the correlation energy for a uniform electron gas. The approximation in the TF model concerns the kinetic energy. For the homogeneous interaction-free electron gas the density is constant and the kinetic energy per unit volume in this

model is proportional to density $\rho^{5/3}$. The TF expression for the energy of a gas of electrons in a given external potential is

$$E^{TF}[\rho(\mathbf{r})] = \frac{\hbar^2}{2m_e}\kappa \int d^3\mathbf{r}\rho^{5/3}(\mathbf{r}) + \frac{e^2}{2}\int d^3\mathbf{r}\int d^3\mathbf{r}'\frac{\rho(\mathbf{r})\rho(\mathbf{r}')}{|\mathbf{r}-\mathbf{r}'|} + \int d^3\mathbf{r}V_{ext}(\mathbf{r})\rho(\mathbf{r}), \tag{A.1}$$

where $\kappa = 3(3\pi^2)^{2/3}/5$. The first and second terms are related to the kinetic energy of electrons and the electrostatic energy of the electron-electron interaction, respectively.

The importance of this equation is not so much how well it is able to really describe the energy even of an atom, but that the energy is given completely in terms of the electron density $\rho(\mathbf{r})$. This is an example of a density-functional for energy allowing us to map a density $\rho(\mathbf{r})$ onto an energy E without any additional information required. Furthermore, the TF model employs the variational principle assuming that the ground state of the system is connected to the electron density for which the energy Eq. (A.1) is minimized under the constraint of $N = \int d^3\mathbf{r}\rho(\mathbf{r})$.

Slater's approximation of HF exchange [160] is another example of exploiting the electron density as the central quantity. In this case, the nonlocal HF exchange energy is approximated proportional to $\int d^3\mathbf{r}\rho^{4/3}(\mathbf{r})$. This approximate expression depends only on the local values of the electron density $\rho(\mathbf{r})$ representing a density-functional for the exchange energy (in the TF model exchange and correlation effects are completely neglected). This formula was originally derived as an approximation to the HF exchange, without any reference to the density-functional theory but it is conceptually connected with this theory. The 4/3 power law for the dependence of the exchange interaction on the electron density was also obtained from a completely different approach using the concept of the uniform electron gas. Combined with the TF energy this approximation is known as the Thomas-Fermi-Dirac model having conceptual importance for DFT methods. In particular, it seems natural that the exchange-correlation energy E_{xc} is approximated by a sum of the exchange E_x and correlation E_c energies. In LDA for the exchange energy calculation the Dirac-Slater exchange energy is used

$$E_x \sim \int d^3\mathbf{r}\rho^{4/3}(\mathbf{r}), \tag{A.2}$$

or the more complicated exchange energy suggested by Barth and Hedin [51]. For

the correlation energy functional $E_c[\rho(\mathbf{r})]$ the situation is more complicated since even for a homogeneous electron gas it is not known analytically. Early approximate expressions for the correlation energy in homogeneous systems were based on applying the perturbation theory and were suggested by Barth and Hedin [51], Gunnarsson and Lundqvist [161]. With the onset of highly precise calculations of the correlation energy for the electron liquid by Ceperley and Alder (CA) [162] the approximations for the correlation energy in a homogeneous system are made by parametrization of CA data for a free-electron gas. There are known parameterizations of Vosko- Wilk-Nisair [163], Perdew-Zunger [42] and Perdew-Wang [52]. The three latter parameterizations of the LDA are implemented in most standard DFT program packages (both for molecules and solids) and in many cases give almost identical results. On the other hand, the earlier parameterizations of the LDA, based on perturbation theory can deviate substantially and are better avoided. The energy density ε_{xc} is treated as a sum of individual exchange and correlation contributions. Two different kinds of densities are involved [159]: the electron density is a per unit volume density, while the energy density is a per particle density. The LDA for E_{xc} formally consists in

$$E_{xc}^{LDA}[\rho(\mathbf{r})] = \int d^3\mathbf{r}\rho(\mathbf{r}) \left(\varepsilon_c^{hom}[\rho(\mathbf{r})] + \varepsilon_x^{hom}[\rho(\mathbf{r})]\right) = \int d^3\mathbf{r}\rho(\mathbf{r})\varepsilon_{xc}^{hom}[\rho(\mathbf{r})]. \tag{A.3}$$

The energy densities ε_x^{hom} and ε_c^{hom} refer to a homogeneous system, i.e. the exchange-correlation energy is simply an integral over all space with the exchange-correlation energy density at each point assumed to be the same as in a homogeneous electron gas with that density. Nevertheless, LDA has proved amazingly successful, even when applied to systems that are quite different from the electron liquid that forms the reference system for the LDA.

For many decades the LDA has been applied in, e.g., calculations of band structures and total energies in solid-state physics. The LDA provides surprisingly good results for metallic solids with delocalized electrons, i.e. those that most closely resemble the uniform electron gas (jellium). At the same time, there are well-known disadvantages of LDA for solids. LDA revealed systematic shortcomings in the description of systems with localized electrons and as a result the underestimation of bond distances and overestimation of binding energies. LDA

calculations as a rule give calculated band gaps that are too small. In quantum chemistry of molecules LDA is much less popular because the local formulation of the energy expression does not account for the electronic redistribution in bonds. For well-localized electrons the non exact cancelation of the self-energy part (self-interaction) of the Hartree term in the LDA exchange functional is important (in HF energy the self-energy part in the Hartree term is canceled by the corresponding part of the exchange term). LDA fails to provide results that are accurate enough to permit a quantitative discussion of the chemical bond in molecules. LDA exploits knowledge of the density at point $\rho(\mathbf{r})$. The real systems, such as molecules and solids, are inhomogeneous (the electrons are exposed to spatially varying electric potentials produced by the nuclei) and interacting (the electrons interact via the Coulomb interaction). The way density-functional theory, in the local-density approximation, deals with this inhomogeneous many-body problem is by decomposing it into two simpler (but still highly nontrivial) problems: the solution of a spatially uniform many-body problem (the homogeneous electron liquid) yields the uniform exchange-correlation energy, and the solution of a spatially inhomogeneous noninteracting problem (the inhomogeneous electron gas) yields the particle density. Both steps are connected by the local-density approximation, which shows how the exchange-correlation energy of the uniform interacting system enters the equations for the inhomogeneous noninteracting system.

In the local spin-density approximation (LSDA) the exchange-correlation energy can be written in terms of either of two spin densities ρ^α and ρ^β

$$E_{xc}^{LSDA}[\rho^\alpha(\mathbf{r}), \rho^\beta(\mathbf{r})] = \int d^3\mathbf{r}\rho(\mathbf{r})\varepsilon_{xc}^{hom}[\rho^\alpha(\mathbf{r}), \rho^\beta(\mathbf{r})]. \tag{A.4}$$

The particular way in which the inhomogeneous many-body problem is decomposed, and the various possible improvements on the LDA, are behind the success of DFT in practical calculations, in particular, materials. The most important improvement of LDA is connected with the attempt to introduce a spatially varying density and include information on the rate of this variation in the functional. The corresponding functionals, known as semilocal functionals, are considered in the next section.

A.2 Beyond the Local Density Approximation

The first successful extensions to the LDA were developed in the early 1980s when it was suggested to supplement the density $\rho(\mathbf{r})$ at a particular point $\mathbf{r}$ with information about the gradient of the electron density at this point in order to account for the nonhomogeneity of the real electron density [164]. LDA was interpreted as the first term of a Taylor expansion of the uniform density, hence the form of the functional was termed the gradient expansion approximation (GEA). It was expected to obtain better approximations of the exchange-correlation functional by extending the series with the next lowest term. In practice, the inclusion of low-order gradient corrections almost never improves on the LDA, and the energy often even worsens it. The reason for this failure is that the GEA has lost many of the properties that made the LDA physically meaningful [164]. Higher-order corrections, on the other hand, are exceedingly difficult to calculate, and little is known about them. It was a major breakthrough when it was realized, in the early 1980s, that instead of power-series-like systematic gradient expansions one could employ more general functions of $\rho(\mathbf{r})$ and $\nabla\rho(\mathbf{r})$, which need not proceed order by order. Such functionals, of the general form

$$E_{xc}^{GGA}[\rho^\alpha, \rho^\beta] = \int d^3\mathbf{r} f[\rho^\alpha, \rho^\beta, \nabla\rho^\alpha, \nabla\rho^\beta], \tag{A.5}$$

have become known as generalized-gradient approximations (GGAs) [165]. GGA functionals are the workhorses of density-functional theory in present day. Different GGAs differ in the choice of the function $f[\rho, \nabla\rho]$. Note that this makes different GGAs much more different from each other than the different parameterizations of the LDA: essentially there is only one correct expression for $\varepsilon_{xc}^{hom}[\rho]$ and the various parameterizations of the LDA are merely different ways of writing it. On the other hand, depending on the method of construction employed for obtaining $f[\rho, \nabla\rho]$ one can obtain very different GGAs. In particular, GGAs used in molecular quantum chemistry typically proceed by fitting parameters to test sets of selected molecules. On the other hand, the GGAs used in physics tend to emphasize exact constraints on the density-functional for the exchange-correlation energy [166]. In this approach, the density-functional approximations are assigned to various rungs according to the number and kind of their local ingredients [166].

The lowest rung is the local spin-density approximation LSDA, the second rung is the generalized gradient approximation GGA (semilocal functionals). More accurate functionals of higher rungs can be called "beyond-GGA functionals" or nonlocal functionals. Third-rung Meta-GGA (MGGA) functionals depend, in addition to the density and its derivatives, also on the kinetic-energy density [167]. Fourth-rung hybrid functionals mix a fraction of the Fock exchange into the DFT exchange functional. MGGA and hybrid functionals can be called orbital functionals because they are represented not only in terms of the electron density, but also contain parts represented in single-particle Kohn.Sham orbitals. Still another type of orbital functional is the self-interaction correction (SIC). Higher-rung density-functionals are increasingly more complex. The semi empirical functionals are fitted to selected data from experiment or from the ab-initio calculations. The higher the rung of the functional the larger is the number of parameters. Once a rung has been selected, there remains little choice about which constraints to satisfy (but greater freedom in how to satisfy them), [166]. Accuracy is expected to increase up the ladder of rungs as additional local ingredients enable the satisfaction of additional constraints. A short summary of exact constraints on E_{xc} can be found in [166].

Nowadays, the most popular GGA functionals are PBE (denoting the functional proposed in 1996 by Perdew, Burke and Ernzerhof [53] in physics, and BLYP (denoting the combination of Becke's 1988 exchange functional [168] with the 1988 correlation functional of Lee, Yang and Parr [169]) in chemistry. PWGGA denotes the GGA functional, suggested by Perdew and Wang [165, 170]. Many other GGA-type functionals are also available, and new ones continue to appear. The new meta-GGA functional TPSS (Tao-Perdew-Staroverov-Scuseria) [171] supersedes an older one the PKZB (Perdew- Kurth-Zupan-Blaha) functional [172]. The known functionals are modified as has been done recently for the PBE functional to improve its accuracy for thermodynamic and electronic properties of molecules [167, 173].

Appendix B

PSEUDOPOTENTIAL

The pseudopotential method allows us to create a smoother potential for the valence electrons only; the work of Phillips and Kleinman first established the theoretical basis of the pseudopotential method [61]. Since this approach is one of the pillars of modern electronic structure theory, we will describe its main ideas here.

In order to develop the pseudopotential for a specific atom we consider it as isolated, and denote by $|\psi^{(n)}\rangle$ the single-particle (sp) states which are the solutions of the single-particle Schrödinger equations. To calculate these states for all the electrons of the atom, using as an external potential that of its nucleus. Let us separate explicitly the single-particle states into valence and core sets, identified as $|\psi^{(v)}\rangle$ and $|\psi^{(c)}\rangle$ respectively. These satisfy the Schrödinger type equations

$$\hat{H}^{sp}|\psi^{(v)}\rangle = E^{(v)}|\psi^{(v)}\rangle, \tag{B.1}$$

$$\hat{H}^{sp}|\psi^{(c)}\rangle = E^{(c)}|\psi^{(c)}\rangle, \tag{B.2}$$

where $\hat{H}^{sp}$ is the appropriate single-particle Hamiltonian for the atom: it contains a potential V^{sp} which includes the external potential due to the nucleus, as well as all the other terms arising from electron-electron interactions. Now let us define a new set of single-particle valence states $|\phi^{(v)}\rangle$ through the following relation:

$$|\psi^{(v)}\rangle = |\widetilde{\phi}^{(v)}\rangle - \sum_{c}\langle\psi^{(c)}|\widetilde{\phi}^{(v)}\rangle|\psi^{(c)}\rangle. \tag{B.3}$$

Applying the single-particle Hamiltonian $\hat{H}^{sp}$ to these states, we obtain

$$\hat{H}^{sp}|\widetilde{\phi}^{(v)}\rangle - \sum_c \langle\psi^{(c)}|\widetilde{\phi}^{(v)}\rangle|\hat{H}^{sp}|\psi^{(c)}\rangle = E^{(v)}\left(|\widetilde{\phi}^{(v)}\rangle - \sum_c \langle\psi^{(c)}|\widetilde{\phi}^{(v)}\rangle|\psi^{(c)}\rangle\right), \tag{B.4}$$

which, taking into account that $\hat{H}^{sp}|\psi^{(c)}\rangle = E^{(c)}|\psi^{(c)}\rangle$, gives

$$\left(\hat{H}^{sp} - \sum_c (E^{(v)} - E^{(c)})|\psi^{(c)}\rangle\langle\psi^{(c)}|\right)|\widetilde{\phi}^{(v)}\rangle = E^{(v)}|\widetilde{\phi}^{(v)}\rangle. \tag{B.5}$$

Therefore, the new states $\widetilde{\phi}^{(v)}$ obey a single-particle equation with a modified potential, but have the same eigenvalues $E^{(v)}$ as the original valence states $\psi^{(v)}$. The modified potential for these states is called the pseudopotential (ps), given by

$$\hat{V}^{ps} = \hat{V}^{sp} + \sum_c (E^{(v)} - E^{(c)})|\psi^{(c)}\rangle\langle\psi^{(c)}|, \tag{B.6}$$

and, correspondingly, the $|\widetilde{\phi}^{(v)}\rangle$'s are called pseudo-wave functions. Why is this a useful approach? First, consider the definition of the pseudo-wave functions through Eq. (B.3): what this definition amounts to is projecting out of the valence wave functions any overlap they have with the core wave functions. In fact, the quantity

$$\sum_c |\psi^{(c)}\rangle\langle\psi^{(c)}|, \tag{B.7}$$

is a projection operator that achieves exactly this result. So the new valence states defined through Eq. (B.3) have zero overlap with core states, but they have the same eigenvalues as the original valence states. Moreover, the potential that these states experience includes, in addition to the regular potential $\hat{V}^{sp}$, the term

$$\sum_c (E^{(v)} - E^{(c)})|\psi^{(c)}\rangle\langle\psi^{(c)}|, \tag{B.8}$$

which is strictly positive, because $E^{(v)} > E^{(c)}$ (valence states have by definition higher energy than core states). Thus, this term is repulsive and tends to push the corresponding states $\widetilde{\phi}^{(v)}$ outside the core. In this sense, the pseudopotential represents the effective potential that valence electrons feel, if the only effect of core electrons is to repel them from the core region. Therefore the pseudo-wave functions experience an attractive Coulomb potential which is shielded near the

position of the nucleus by the core electrons, so it should be a much smoother potential without the $1/r$ singularity due to the nucleus at the origin. Farther away from the core region, where the core states vanish exponentially, the potential that the pseudo-wave functions experience is the same as the Coulomb potential of an ion, consisting of the nucleus plus the core electrons. In other words, through the pseudopotential formulation we have created a new set of valence states, which experience a weaker potential near the atomic nucleus, but the proper ionic potential away from the core region. Since it is this region in which the valence electrons interact to form bonds that hold the solid together, the pseudo-wave functions preserve all the important physics relevant to the behaviour of the solid. The fact that they also have exactly the same eigenvalues as the original valence states, also indicates that they faithfully reproduce the behaviour of true valence states. There are some aspects of the pseudopotential, at least in the way that was formulated above, that make it somewhat suspicious. First, it is a non-local potential, see Eq. (B.6). This certainly complicates things. The pseudopotential also depends on the energy $E^{(v)}$, as the above relationship demonstrates, which is an unknown quantity if we view Eq. (B.5) as the Schrödinger equation that determines the pseudo-wave functions $\phi^{(v)}$ and their eigenvalues. Finally, the pseudopotential is not unique. This can be demonstrated by adding any linear combination of $|\psi^{(c)}\rangle$ states to $|\widetilde{\phi}^{(v)}\rangle$ to obtain a new state $|\widehat{\phi}^{(v)}\rangle$:

$$|\widehat{\phi}^{(v)}\rangle = |\widetilde{\phi}^{(v)}\rangle + \sum_{c'} \alpha_{c'} |\psi^{(c')}\rangle, \tag{B.9}$$

where $\alpha_{c'}$ are numerical constants. Using Eq. (B.5), we obtain

$$\left(\hat{H}^{sp} + \sum_{c} |\psi^{(c)}\rangle\langle\psi^{(c)}|\right)\left(|\widehat{\phi}^{(v)}\rangle - \sum_{c'} \alpha_{c'}|\psi^{(c')}\rangle\right) = E^{(v)}\left(|\widehat{\phi}^{(v)}\rangle - \sum_{c'} \alpha_{c'}|\psi^{(c')}\rangle\right) \tag{B.10}$$

We can now use $\langle\psi^{(c)}|\psi^{(c')}\rangle = \delta_{cc'}$ to reduce the double sum on the left hand side of this equation to a single sum, and eliminate common terms from both sides to arrive at

$$\left(\hat{H}^{sp} + \sum_{c} |\psi^{(c)}\rangle\langle\psi^{(c)}|\right)|\widehat{\phi}^{(v)}\rangle = E^{(v)}|\widehat{\phi}^{(v)}\rangle. \tag{B.11}$$

This shows that the state $|\widehat{\phi}^{(v)}\rangle$ obeys exactly the same single-particle equation as the state $|\widetilde{\phi}^{(v)}\rangle$, which means it is not uniquely defined, and therefore the pseudopotential is not uniquely defined. All these features may cast a long shadow of doubt on the validity of the pseudopotential construction in the mind of the skeptic (a trait not uncommon among physicists). Practice of this art, however, has shown that these features can actually be exploited to define pseudopotentials that work very well in reproducing the behaviour of the valence wave functions in the regions outside the core, which are precisely the regions of interest for the physics of solids. As an example, we discuss next how typical pseudopotentials are constructed for calculations of the properties of solids [63]. We begin with a self-consistent solution of the single-particle equations for all the electrons in an atom (core and valence). For each valence state of interest, we take the calculated radial wave function and keep the tail starting at some point slightly before the last extremum. When atoms are placed at usual interatomic distances in a solid, these valence tails overlap significantly, and the resulting interaction between the corresponding electrons produces binding between the atoms. We want therefore to keep this part of the valence wave function as realistic as possible, and we identify it with the tail of the calculated atomic wave function. We call the radial distance beyond which this tail extends the cutoff radius r_c, so that the region $r < r_c$ corresponds to the core. Inside the core, the behaviour of the wave function is not as important for the properties of the solid. Therefore, we can construct the pseudo-wave function to be a smooth function which has no nodes and goes to zero at the origin. We can achieve this by taking some combination of smooth functions which we can fit to match the true wave function and its first and second derivative at r_c, and approach smoothly to zero at the origin. This hypothetical wave function must be normalized properly. Having defined the pseudo-wave function, we can invert the Schrödinger equation to obtain the potential which would produce such a wave function. This is by definition the desired pseudopotential: it is guaranteed by construction to produce a wave function which matches exactly the real atomic wave function beyond the core region $r < r_c$, and is smooth and nodeless inside the core region, giving rise to a smooth potential. We can then use this pseudopotential as the appropriate potential for the valence electrons in the solid. We note here two important points: (i) The pseudo-wave functions can be chosen to be nodeless inside the core, due to the non-uniqueness in the definition of the pseu-

dopotential and the fact that their behaviour inside the core is not relevant to the physics of the solid. The true valence wave functions have many nodes in order to be orthogonal to core states. (ii) The nodeless and smooth character of the pseudo-wavefunctions guarantees that the pseudopotentials produced by inversion of the Schrödinger equation are finite and smooth near the origin, instead of having a $1/r$ singularity like the Coulomb potential. Of course, each valence state will give rise to a different pseudopotential, but this is not a serious complication as far as actual calculations are concerned. All the pseudopotentials corresponding to an atom will have tails that behave like $Z^{valence}/r$, where $Z^{valence}$ is the valence charge of the atom, that is, the ionic charge for an ion consisting of the nucleus and the core electrons. The huge advantage of the pseudopotential is that now we have to deal with the valence electrons only in the solid (the core electrons are essentially frozen in their atomic wave functions), and the pseudopotentials are smooth so that standard numerical methods can be applied (such as Fourier expansions) to solve the single-particle equations. There are several details of the construction of the pseudopotential that require special attention in order to obtain potentials that work and actually simplify calculations of the properties of solids, but we will not go into these details here. Suffice to say that pseudopotential construction is one of the arts of performing reliable and accurate calculations for solids, but through the careful work of many physicists in this field over the last couple of decades there exist now very good pseudopotentials for essentially all elements of interest in the Periodic Table [59].

Appendix C

Non-equilibrium theory

C.1 Non-equilibrium Green's Function

In order to calculate the non-equilibrium Green's function we consider a system evolving under a Hamiltonian which can be split into

$$H = h + H^{'}(t), \tag{C.1}$$

where h is the time-independent part of the Hamiltonian. It is assummed the time-dependent part of the Hamiltonian $H^{'}(t)$ vanishes at $t < t_0$, i.e. it represents a perturbation which is switched on at $t = t_0$. This perturbation part may be an electric field or any external applied field. Before the perturbation is turned on, the system is assumed to be described by the thermal equilibrium density matrix

$$\rho(h) = \frac{\exp(-\beta h)}{\mathrm{Tr}[\exp(-\beta h)]}, \tag{C.2}$$

where $\beta = \frac{1}{k_B T}$, Tr represents the trace, k_B is the Boltzmann constant and T is the temperature. For $t \geq 0$ the main task would be to calculate statistical averages associated with a quantum mechanical operator O

$$\langle O_{\mathcal{H}}(t) \rangle = \mathrm{Tr}[\rho(h) O_{\mathcal{H}}(t)]. \tag{C.3}$$

Here the subscript $\mathcal{H}$ indicates that the time-dependence is governed by the full Hamiltonian, i.e. $O_{\mathcal{H}}(t)$ is written in the Heisenberg picture. The definition in Eq. (C.3) can be generalized to many time-dependent quantities.

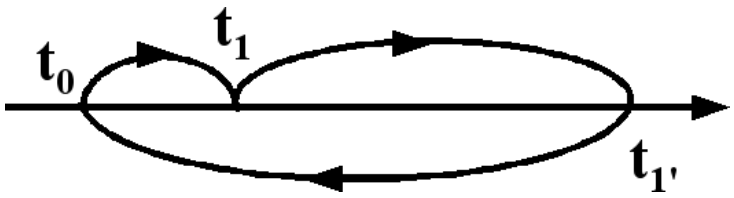

Figure C.1: Contour C.

C.2 Contour Ordered Green's Function

The contour ordered Green's functions are defined on the so called Keldysh contour shown in Fig. C.1. The Keldysh contour is defined in the complex plane starting at t_0 and running along the real time axis, passing through t_1 and $t_{1'}$ once and finally returning to t_0. The Green's function is given by:

$$G(1,1') = -i\langle T_C[\psi_H(1)\psi_H^\dagger(1')]\rangle, \tag{C.4}$$

where the average given by $\langle\rangle$ is defined on a suitable non-equilibrium statistics, T_C is the contour-ordering operator, ψ_H and $\psi_H^\dagger$ are the field operators in the Heisenberg picture. It is important to note that their time evolution is with respect to a the real time t. Thus the complex time τ consists of a real time t and a branch label, i.e., the ordering on the contour is determined by t and the branch label. The shorthand notation $(1) \equiv (x_1, t_1)$ (or $(1) \equiv (x_1, \tau_1)$ when appropriate) [95].

Due to the two branches the contour ordered Green's function contains four different real time Green's functions, corresponding to the following placements of the time labels contour

$$G(1,1') = \begin{cases} G_c(1,1') & t_1, t_{1'} \in C_1 \\ G_>(1,1') & t_1 \in C_2, t_{1'} \in C_1 \\ G_<(1,1') & t_1 \in C_1, t_{1'} \in C_2 \\ G_{\tilde{c}}(1,1') & t_1, t_{1'} \in C_2 \end{cases}$$

Here G_c and $G_{\tilde{c}}$ are respectively the time ordered and anti time ordered Green's functions:

$$\begin{aligned} G_c(1,1') &= -i\langle T[\psi_H(1)\psi_H^\dagger(1')]\rangle \\ &= -i\theta[t_1 - t_{1'}]\langle\psi_H(1)\psi_H^\dagger(1')\rangle + i\theta[t_{1'} - t_1]\langle\psi_H^\dagger(1')\psi_H(1)\rangle \end{aligned} \tag{C.5}$$

$$G_{\tilde{c}}(1,1') = -i\langle \tilde{T}[\psi_H(1)\psi_H^\dagger(1')]\rangle$$
$$= -i\theta[t_{1'} - t_1]\langle \psi_H(1)\psi_H^\dagger(1')\rangle + i\theta[t_1 - t_{1'}]\langle \psi_H^\dagger(1')\psi_H(1)\rangle \quad \text{(C.6)}$$

The greater Green's function $G^>$ and the lesser Green's function $G^<$ are given by:

$$G^>(1,1') = -i\langle \psi_H(1)\psi_H^\dagger(1')\rangle, \quad \text{(C.7)}$$

$$G^<(1,1') = i\langle \psi_H^\dagger(1')\psi_H(1)\rangle. \quad \text{(C.8)}$$

Another set of important functions are the retarded and the advanced Green functions. They are defined as

$$G^r(1,1') = -i\theta[t_1 - t_{1'}]\langle \{\psi_H(1), \psi_H^\dagger(1')\}\rangle$$
$$= \theta[t_1 - t_{1'}][G^>(1,1') - G^<(1,1')], \quad \text{(C.9)}$$

$$G^a(1,1') = i\theta[t_{1'} - t_1]\langle \{\psi_H(1), \psi_H^\dagger(1')\}\rangle$$
$$= \theta[t_{1'} - t_1][G^<(1,1') - G^>(1,1')] \quad \text{(C.10)}$$

Here curly brackets denote an anticommutator. One can notice that the equilibrium and non-equilibrium Green's functions are structurally equivalent. The only differece is the replacement of real integrals by contour integrals [95].

C.3 General Current Formula

We consider the transport of electrons in a system which can be divided into three regions: A central region (C), a left lead (L), and a right lead (R). The leads are metallic and connect the scattering region with two thermal reservoirs that are maintained at the chemical potentials μ_L and μ_R. Following Meir and Wingreen [83] we shall derive an expression for the current through the system under quite general conditions to be stated below.

When a bias voltage is applied, the junction device is driven out of equilibrium and Eq. (C.4) describes this system. In non-equilibrium situations the retarded Green's function and the lesser Green's function are independent, and they are both very important. The retarded and advanced Green's functions have a nice analytic structure (poles in one half plane) and are suitable for calculating a physical

response. The lesser Green's function is directly linked to physical observables, for example, the electron density is determined as follows [95]:

$$n(\vec{r},t) = \langle \psi_H^\dagger(\vec{r},t)\psi_H(\vec{r},t)\rangle = -iG^<(\vec{r},t;\vec{r},t). \tag{C.11}$$

For steady states, the Green's functions only depend on the time difference $t-t'$, for which we can use Fourier transform on the energy. The Hamiltonian of the junction can be is written as:

$$\begin{aligned} H &= H_{L,R} + H_C + H_T \\ &= \sum_{\substack{k,\alpha\in L,R \\ n}} \varepsilon_{k\alpha} c_{k\alpha}^\dagger c_{k\alpha} + H_C(\{d_n\}^\dagger;\{d_n\}) \\ &+ \sum_{\substack{k,\alpha\in L,R \\ n}} V_{k\alpha,n} c_{k\alpha}^\dagger d_n + V_{k\alpha,n}^* d_n^\dagger c_{k\alpha}, \end{aligned} \tag{C.12}$$

where $c_{k\alpha}(c_{k\alpha}^\dagger)$ and $d_n(d_n^\dagger)$ are annihilation (creation) operators in the leads and the central region, respectively. In this picture the description of the leads is at the single-particle level, while only the coupling between the leads and the central region makes the problem to be fully interacting. Before the coupling between the three regions is established, the left and right leads maintain their own thermal equilibrium with the associated Fermi levels μ_L and μ_R, respectively. The corresponding Green's functions in the leads for the uncoupled systems are $g_{k\alpha}^<(E) = 2i\pi f(\varepsilon_{k\alpha}-\mu_{L/R})\delta(E-\varepsilon_{k\alpha})$ and $g_{k\alpha}^{r,a}(E) = (E-\varepsilon_{k\alpha}\pm i\eta)^{-1}$, where $f(E) = 1/[1+\exp(\beta E)]$ is the Fermi distribution function and η is a small positive number ensuring proper convergence of the Fourier integrals. As the leads are coupled to the central region, a current will start to flow. After some time the system achieves a steady state. In the following we consider the steady current at a certain time t. The steady current from the left lead into the central region can be defined as [95]:

$$I_L(t) = \frac{ie}{\hbar}\langle [N_L(t), H(t)]\rangle,\ N_L = \sum_{k,\alpha\in L} c_{k\alpha}^\dagger c_{k\alpha} \tag{C.13}$$

where N_L is the number operator of the left lead. Doing the algebraic calculations for the commutator, the current turns out to be expressed as:

$$I_L(t) = \frac{ie}{\hbar}\sum_{\substack{k,\alpha\in L \\ n}} V_{k\alpha,n}\langle c_{k\alpha}(t)^\dagger d_n(t)\rangle - V_{k\alpha,n}^*\langle d_n^\dagger(t) c_{k\alpha}(t)\rangle. \tag{C.14}$$

Now define two new Green's functions (we set $\hbar = 1$, and reintroduce it in the final expression for the current):

$$G^{<}_{n,k\alpha}(t,t') = i\langle c^{\dagger}_{k\alpha}(t')d_n(t)\rangle, \tag{C.15}$$

$$G^{<}_{k\alpha,n}(t,t') = i\langle d^{\dagger}_{n}(t')c_{k\alpha}(t)\rangle. \tag{C.16}$$

It can be seen that the current is given by the time-diagonal components of these two Green's functions. From Eq.'s (C.14), Eq. (C.15) and Eq. (C.16) one can write:

$$\begin{aligned} I_L(t) &= \frac{e}{\hbar}\sum_{\substack{k,\alpha\in L,R\\ n}} V_{k\alpha,n}G^{<}_{n,k\alpha}(t,t) - V^{*}_{k\alpha,n}G^{<}_{k\alpha,n}(t,t) \\ &= \frac{2e}{\hbar}\sum_{\substack{k,\alpha\in L,R\\ n}} \mathrm{Re}\left[V_{k\alpha,n}G^{<}_{n,k\alpha}(t,t)\right]. \end{aligned} \tag{C.17}$$

Next, one needs an expression for $G^{<}_{k\alpha,n}(t-t')$. For the present case, with noninteracting leads, a general relation for the contour-ordered Green function $G^{<}_{k\alpha,n}(\tau-\tau')$ can be derived rather easily with the equation-of-motion technique. Since the non-equilibrium theory is structurally equivalent to equilibrium theory, it is sufficient to consider the $T = 0$ equation of motion for the time-ordered Green function $G_{k\alpha,n}$:

$$-i\frac{\partial}{\partial t'}G_{n,k\alpha}(t-t') = \varepsilon_{k\alpha}G_{n,k\alpha}(t-t') + \sum_m V_{k,\alpha,m}G_{nm}(t-t'), \tag{C.18}$$

where we defined the central region time-ordered Green function function $G_{nm}(t-t') = -i\langle T\left\{d_n(t)d^{\dagger}_m(t')\right\}\rangle$. Eq. (C.18) can be rewritten as

$$G_{n,k\alpha}g^{-1}_{k\alpha} = \sum_m V_{k\alpha,m}G^{t}_{nm} \tag{C.19}$$

where $g^{-1}_{k\alpha} = -i\frac{\partial}{\partial t'} - \varepsilon_{k\alpha}$. The solution of Eq. (C.19) is given by

$$G_{n,k\alpha}(t-t') = \sum_m \int dt_1 G_{nm}(t-t_1)V^{*}_{k\alpha,m}g^{t}_{k\alpha}(t_1-t'). \tag{C.20}$$

This equation has in non-equilibrium precisely the same form, except that the intermediate time integration runs on the complex contour:

$$G_{n,k\alpha}(\tau,\tau') = \sum_m \int d\tau_1 G_{nm}(\tau,\tau_1)V^{*}_{k\alpha,m}g_{k\alpha}(\tau_1,\tau'). \tag{C.21}$$

Here $G_{nm}(\tau,\tau_1)$ is the contour-ordered Green's function for the central region. The analytic continuation rules can be applied to Eq. (C.21), and we find

$$G^<_{n,k\alpha}(t-t') = \sum_m \int dt_1 V^*_{k\alpha,m}[G^r_{nm}(t-t_1)g^<_{k\alpha}(t_1-t') + G^<_{nm}(t-t_1)g^a_{k\alpha}(t_1-t')]. \tag{C.22}$$

The Fourier transform of Eq. (C.22) is

$$G^<_{n,k\alpha}(E) = \sum_m V^*_{k\alpha,m}[G^r_{nm}(E)g^<_{k\alpha}(E) + G^<_{nm}(E)g^a_{k\alpha}(E)]. \tag{C.23}$$

Thus, using Eq. (C.17), the current becomes

$$I_L(t) = \frac{2e}{\hbar}\int \frac{dE}{2\pi}\mathrm{Re}\left[\sum_{\substack{k,\alpha\in L\\ n,m}} V_{k\alpha,n}V^*_{k\alpha,m}[G^r_{nm}(E)g^<_{k\alpha}(E) + G^<_{nm}(E)g^a_{k\alpha}(E)]\right]. \tag{C.24}$$

In the following, explicit reference to the E dependence will sometimes be omitted to simplify the notations. It is useful to convert the momentum summation into an energy integration by introducing the broadening function of the left lead

$$\Gamma^L_{mn}(E) = 2\pi\sum_{k,\alpha\in L}\delta(E-\varepsilon_{k\alpha})V_{k\alpha,n}V^*_{k\alpha,m}. \tag{C.25}$$

There are two terms in the current expression (C.24). Consider, for example, the piece involving G^r_{nm}, which we evaluate as

$$\begin{aligned}
&\frac{2e}{\hbar}\int\frac{dE}{2\pi}\int d\varepsilon_k\Gamma^L(\varepsilon_k)\mathrm{Re}[G^r(E)i\delta(E-\varepsilon_k)f_L(E)]\\
&\quad= \frac{2e}{\hbar}\int\frac{dE}{2\pi}f_L(E)\Gamma^L(E)\mathrm{Re}[iG^r(E)]\\
&\quad= -\frac{2e}{\hbar}\int\frac{dE}{2\pi}f_L(E)\Gamma^L(E)\mathrm{Im}[G^r(E)]\\
&\quad= i\frac{2e}{\hbar}\int\frac{dE}{2\pi}f_L(E)\Gamma^L(E)[G^r(E)-G^a(E)].
\end{aligned} \tag{C.26}$$

Similar manipulations can be applied to the other term, and the current from left (right) contact to central region becomes

$$I_{L/R}(t) = \frac{ie}{\hbar}\int\frac{dE}{2\pi}\mathrm{Tr}\left[\Gamma^{L/R}\left\{G^<(E) + f_{L/R}\left(G^r(E)-G^a(E)\right)\right\}\right]. \tag{C.27}$$

In steady state, the current will be uniform, so that the general expression for the current through a two-terminal electrode-molecule-electrode device is

$$I = \frac{I_L - I_R}{2} = \frac{ie}{2\hbar}\int \frac{dE}{2\pi}\mathrm{Tr}\left[\left(\Gamma^L - \Gamma^R\right)G^< + \left(f_L\Gamma^L - f_R\Gamma^R\right)\left(G^r - G^a\right)\right]. \tag{C.28}$$

Clearly, the current is determined by three factors: (1) the coupling between the central region and the leads, accounted for by the broadening functions Γ^L and Γ^R; (2) the occupation of the energy levels, given by the Fermi functions f_L and f_R for the leads and by $iG^<$ for the central region; (3) the energy levels in the central region, given by $i(G^r - G^a)$. This current formula is a very powerful result, which is valid for two-terminal devices with any arbitrary structure. The practical problem of its application is how to calculate these Green's functions, which is not an easy task. Both the lesser Green's function and the retarded Green's function of the central region must be calculated in the presence of tunneling, which can be realized by simultaneously solving the Keldysh equation for $G^<$ and the non-equilibrium Dyson equation for $G^{r,a}$:

$$G^< = G^r[\Sigma_L^< + \Sigma_R^< + \Sigma_{int}^<]G^a, \tag{C.29}$$

$$G^{r,a} = g^{r,a} + g^{r,a}[\Sigma_L^{r,a} + \Sigma_R^{r,a} + \Sigma_{int}^{r,a}]G^a. \tag{C.30}$$

Here, $g^{r,a}$ are the reference non-interacting retarded and advanced Green's function for the central region. The lesser, retarded and advanced self-energies $\Sigma_R^{<,r,a}$ for the central region include two parts, one is due to the coupling to the left and right leads, the other is due to the interactions limited in the central region that should be determined by suitable approximations. It should be noted that the exact many-body self-energy operators are usually non-hermitian and energy-dependent. For the single particle case, that is, when the interaction in the central region is also treated with a mean-field approximation like the Hartree-Fock (HF) approximation or the Kohn-Sham DFT, the Hamiltonian of the central region can be written as $H_C = \sum_n \varepsilon_n d_n^\dagger d_n$ and the current formula can be further simplified. In this case, one part of the retarded and advanced self-energies that originates from the electron-electron interaction in the central region is approximated by some suitable potentials which can be adsorbed in the Hamiltonian for the central region. Thus, the retarded and advanced self-energies only include the part due to

the coupling to the left and right leads, which take the following form:

$$\Sigma^{r,a}_{nm} = \frac{V_{k\alpha,n}V^*_{k\alpha,m}}{E - \varepsilon_{k\alpha} \pm i\eta}. \tag{C.31}$$

Comparing with the definition of the broadening function, it can be seen that the broadening function is equal to twice the imaginary part of the retarded self-energy, i.e.,

$$\Gamma^{L/R} = i(\Sigma^r_{L/R} - \Sigma^a_{L/R}). \tag{C.32}$$

Similarly, the lesser self-energy also includes only the part due to the coupling to the leads:

$$\Sigma^<_{nm} = i(f_L\Gamma^L + f_R\Gamma^R). \tag{C.33}$$

Thus, the lesser Green's function for the non-interacting central region is

$$G^< = if_L G^r\Gamma^L G^a + if_R G^r\Gamma^R G^a. \tag{C.34}$$

Putting Eq. (C.32) and Eq. (C.34) into Eq. (C.28) and using the relation $G^r - G^a = -iG^r(\Gamma^L + \Gamma^R)G^a$, we get the current formula for the non-interacting case:

$$I = \frac{e}{h}\int dE(f_L - f_R)T(E), \tag{C.35}$$

where $T(E) = \mathrm{Tr}[\Gamma^L G^r \Gamma^R G^a]$ is the transmission function. If we assume that the two spin contributions are degenerate, then the current formula becomes

$$I = \frac{2e}{h}\int dE(f_L - f_R)T(E) \tag{C.36}$$

This is the Landauer formula, which connects the current to the transmission across a scattering region. It should be stressed that this formalism and its interpretation break down in the presence of interactions in the central region.

Appendix D

DENSITY OF STATES

In the numerical calculations we repeatedly calculate both total and projected densities of states. The density of states for a system described by the Hamiltonian matrix $\hat{H}$ is defined by [174]:

$$DOS(E) = \sum_i \langle \psi_i | \delta(E - \hat{H}) | \psi_i \rangle, \tag{D.1}$$

where $|\psi_i\rangle$ is the eigenstates of the Hamiltonian $\hat{H}$. One can rewrite Eq. (D.1) as

$$DOS(E) = \sum_i \langle \psi_i | \psi_i \rangle \delta(E - \varepsilon_i), \tag{D.2}$$

here ε_i are a discrete set of eigenenergies. So for a complete and orthonormal basis set, the density of states is a set of delta peaks. Eq. (D.2) can be written as follows:

$$DOS(E) = \sum_i PDOS_i(E) \tag{D.3}$$

where the $PDOS$ is the projected density of states

$$PDOS_i(E) = \sum_j \langle \psi_j | i \rangle \langle i | \psi_j \rangle \delta(E - \varepsilon_j). \tag{D.4}$$

Here the quantity $PDOS_i(E)$ expresses the density of states projected onto $|i\rangle$.

Bibliography

[1] K. von Klitzing, Rev. Mod. Phys. **58**, 519 (1986).

[2] Y. Alhassid, Rev. Mod. Phys. **72**, 895 (2000).

[3] D. A. Wharam, T. J. Thornton, R. Newbury, M. Repper, H. Ahmed, J. E. F. Frost, D. G. Hasko, D. C. Peacock, D. A. Ritchie, G. A. C. Jones, J. Phys. C **21**, L887 (1988).

[4] B. J. van Wees, H. van Houten, C. W. J. Beenakker, J. G. Williamson, L. P. Kouwenhoven, D. van der Marel, C. T. Foxon, Phys. Rev. Lett. **60**, 848 (1988).

[5] R. M. Martin, *Electronic Structure: Basis Theory and Practical Methods* (Cambridge University Press, 2004).

[6] R. Landauer, Phil. Mag. **21**, 863 (1970).

[7] L. P. Kadanoff, G. Baym, *Quantum Statistical Mechanics* (W.A. Benjamin, New York, 1962).

[8] J. Taylor, H. Guo, J. Wang, Phys. Rev. B **63**, 245407 (2001).

[9] M. Bradbyge, J. Taylor, K. Stokbro, J.-L. Mozos, P. Ordejón, Phys. Rev. B **65**, 165401 (2002).

[10] A. R. Rocha, V. M. Garcia-Suárez, S. W. Bailey, C. J. Lambert, J. Ferrer, S. Sanvito, Nature Materials **4**, 335 (2005).

[11] A. R. Rocha, V. M. Garcia-Suárez, S. W. Bailey, C. J. Lambert, J. Ferrer, S. Sanvito, Phys. Rev. B **73**, 085414 (2006).

[12] K. Eisenbeiser, J. M. Finder, Z. Yu, J. Ramdani, J. A. Curless, J. A. Hallmark, R. Droopad, W. J. Ooms, L. Salem, S. Bradshaw, C. D. Overgaard, Appl. Phys. Lett. **76**, 1324 (2000).

[13] C. H. Ahn, K. M. Rab, J.-M. Triscone, Science **303**, 488 (2004).

[14] H. Hilgenkamp, J. Mannhart, Rev. Mod. Phys. **74**, 485 (2003).

[15] U. Schwingenschlögl, C. Schuster, Phys. Rev. B **79**, 092505 (2009).

[16] H. Zhang, Y. Aoyagi, S. Iwai, S. Namba, Appl. Phys. A **44**, 273 (1987).

[17] C. H. Ahn, A. Bhattacharya, M. D. Ventra, J. N. Eckstein, C. D. Frisbie, M. E. Gershenson, A. M. Goldman, I. H. Inoue, J. Mannhart, A. J. Millis, A. F. Morpurgo, D. Natelson, J.-M. Triscone, Rev. Mod. Phys. **78**, 1185 (2006).

[18] S. Okamoto, A. J. Millis, Nature (London) **428**, 630 (2004).

[19] S. Thiel, G. Hammerl, A. Schmehl, C. W. Schneider, J. Mannhart, Science **313**, 1942 (2006).

[20] U. Schwingenschlögl, C. Schuster, Europhys. Lett. **81**, 17007 (2008).

[21] M. Scheffler, C. Stampfl, *Electronic Structure: Theory and Practical Methods* (Cambridge University Press, Cambridge, 2004).

[22] P. S. Bagus, K. Hermann, C. J. Wöll, J. Chem. Phys. **123**, 184109 (2005).

[23] C. Schuster, U. Schwingenschlögl, Chem. Phys. Lett. **468**, 75 (2009).

[24] M. N. Baibich, J. M. Broto, A. Fert, F. Nguyen Van Dau, F. Petroff, P. Etienne, G. Creuzet, A. Friederich, J. Chazelas, Phys. Rev. Lett. **61**, 2472 (1988).

[25] G. Binasch, P. Grünberg, F. Saurenbach, W. Zinn, Phys. Rev. B **39**, 4828 (1989).

[26] P. Armour, T.-H. Shen, M.-L. Ke, R. Grey, Appl. Surf. Sci. **123/124**, 412 (1998).

[27] A. Yaniv, Phys. Rev. B **17**, 3904 (1977).

[28] K. Xia, P. J. Kelly, G. E. W. Bauer, I. Turek, J. Kudrnovský, V. Drchal, Phys. Rev. B **63**, 064407 (2001).

[29] A. A. Abrikosov, L. P. Gorkov, I. E. Dzyaloshinski, *Methods of Quantum Field Theory in Statistical Physics* (Dover, New York, 1963).

[30] A. L. Fetter, J. D. Walecka, *Quantum Theory of Many Particle Systems* (McGraw-Hill, Boston, 1971).

[31] L. Hedin, Phys. Rev. **139**, A796 (1965).

[32] P. van Gelderen, P. A. Bobbert, P. J. Kelly, G. Brocks, Phys. Rev. Lett. **85**, 2989 (2000).

[33] G. Onida, L. Reining, A. Rubio, Rev. Mod. Phys. **74**, 601 (2002).

[34] N. E. Dahlen, R. van Leeuwen, U. von Barth, Phys. Rev. A **73**, 012511 (2006).

[35] G. Senatore, N. H. March, Rev. Mod. Phys. **66**, 445 (1994).

[36] I. D. Feranchuk, L. I. Komarov, I. V. Nichipor, A. P. Ulyanenkov, Ann. Phys. (New York) **238**, 370 (1995).

[37] W. M. C. Foulkes, L. Mitas, R. J. Needs, G. Rajagopal, Rev. Mod. Phys. **73**, 33 (2001).

[38] C. D. Sherrill, H. F. Schaefer, Adv. Quant. Chem. B **34**, 143 (1999).

[39] P. Hohenberg, W. Kohn, Phys. Rev. **136**, B864 (1964).

[40] W. Kohn, L. J. Sham, Phys. Rev. **140**, A1133 (1965).

[41] R. O. Jones, O. Gunnarsson, Rev. Mod. Phys. **61**, 689 (1989).

[42] J. Perdew, A. Zunger, Phys. Rev. B **23**, 5048 (1981).

[43] K. Burke, J. Werschnik, E. K. U. Gross, J. Chem. Phys. **123**, 062206 (2005).

[44] E. Merzbacher, *Quantum Mechanics* (John Wiley & Sons Inc., New York, 1998).

[45] C. Kittel, *Quantum Theory of Solids* (John Wiley and Sons, Inc., New York, 1963).

[46] N. H. March, *Electron Density Theory of Atoms and Molecules* (Academic Press, London, 1992).

[47] H. Eschrig, *The Fundamentals of Density Functional Theory* (Teubner, Leipzig, 1996).

[48] R. G. Parr, W. Yang, *Density-functional Theory of Atoms and Molecules* (Oxford University Press, Oxford, 1989).

[49] J. P. Perdew, S. Kurth, Lecture Notes in Phys. **620**, 1 (2003).

[50] W. Kohn, Rev. Mod. Phys. **71**, 1253 (1998).

[51] U. von Barth, L. Hedin, J. Phys.: Condens. Matter **5**, 1629 (1972).

[52] J. Perdew, Y. Wang, Phys. Rev. B **45**, 13244 (1992).

[53] J. P. Perdew, K. Burke, M. Ernzerhof, Phys. Rev. Lett. **77**, 3865 (1996).

[54] M. C. Payne, M. P. Teter, D. C. Allan, T. A. Arias, J. D. Joannopoulos, Rev. Mod. Phys. **64**, 1045 (1992).

[55] J. Ihm, A. Zunger, M. L. Cohen, J. Phys. C: Sol. State Phys. **12**, 4409 (1979).

[56] D. Singh, *Plane waves, Pseudopotentials and the LAPW Method* (Kluwer Academic, 1994).

[57] P. Ordejón, E. Artacho, J. M. Soler, Phys. Rev. B **53**, R10441 (1996).

[58] O. K. Andersen, O. Jepsen, Phys. Rev. Lett. **53**, 2571 (1984).

[59] G. B. Bachelet, D. R. Hamann, M. Schlüter, Phys. Rev. B **26**, 4199 (1982).

[60] D. Vanderbilt, Phys. Rev. B **41**, 7892 (1990).

[61] J. C. Phillips, L. Kleinman, Phys. Rev. **116**, 287 (1959).

[62] L. Kleinman, D. M. Bylander, Phys. Rev. Lett. **48**, 1425 (1982).

[63] D. R. Hamann, M. Schlüter, C. Chiang, Phys. Rev. Lett. **43**, 1494 (1979).

[64] N. Troullier, J. L. Martins, Phys. Rev. B **43**, 1993 (1991).

[65] K. Laasonen, A. Pasquarello, R. Car, C. Lee, D. Vanderbilt, Phys. Rev. B **47**, 10142 (1993).

[66] P. E. Blöchl, Phys. Rev. B **50**, 17953 (1994).

[67] G. Kresse, D. Joubert, Phys. Rev. B **59**, 1758 (1999).

[68] J. M. Soler, E. Artacho, J. D. Gale, A. García, J. Junquera, P. Ordejón, D. Sánchez-Portal, J. Phys.: Condens. Matter **14**, 2745 (2002).

[69] F. Mauri, G. Galli, R. Car, Phys. Rev. B **47**, 9973 (1993).

[70] P. Ordejón, D. A. Drabold, R. M. Martin, M. P. Grumbach, Phys. Rev. B **51**, 1456 (1995).

[71] J. Kim, F. Mauri, G. Galli, Phys. Rev. B **52**, 1640 (1995).

[72] X.-P. Li, R. W. Nunes, D. Vanderbilt, Phys. Rev. B **47**, 10891 (1993).

[73] S. Datta, *Electronic Transport in Mesoscopic Systems* (Cambridge University Press, Cambridge, UK, 1995).

[74] D. K. Ferry, S. M. Goodnick, *Transport in Nanostructures* (Cambridge University Press, Cambridge, UK, 1997).

[75] N. W. Ashcroft, N. D. Mermin, *Solid State Physics* (Saunders College Publishing, USA, 1976).

[76] N. Agraït, A. L. Yeyati, J. M. van Ruitenbeek, Phys. Rep. **377**, 81 (2003).

[77] D. Fisher, P. Lee, Phys. Rev. B **23**, 6851 (1981).

[78] M. Büttiker, Y. Imry, R. Landauer, S. Pinhas, Phys. Rev. B **31**, 6207 (1985).

[79] M. Büttiker, Phys. Rev. Lett. **57**, 1761 (1986).

[80] G. Rubio, N. Agraït, S. Vieira, Phys. Rev. Lett. **76**, 2302 (1996).

[81] E. Scheer, N. Agraït, J. C. Cuevas, A. L. Yeyati, B. Ludoph, A. Martin-Rodero, G. R. Bollinger, J. M. van Ruitenbeek, C. Urbina, Nature **394**, 154 (1998).

[82] A. I. Yanson, G. R. Bollinger, H. E. van den Brom, N. Agraït, J. M. van Ruitenbeek, Nature **395**, 783 (1998).

[83] Y. Meir, N. S. Wingreen, Phys. Rev. Lett. **68**, 2512 (1992).

[84] K. S. Thygesen, Phys. Rev. B **73**, 035309 (2006).

[85] Y. Xue, S. Datta, M. A. Ratner, Chem. Phys. **281**, 151 (2001).

[86] S.-H. Ke, H. U. Baranger, W. Yang, Phys. Rev. B **70**, 085410 (2004).

[87] T. Frederiksen, M. Brandbyge, N. Lorente, A.-P. Jauho, Phys. Rev. Lett. **93**, 256601 (2004).

[88] M. Galperin, M. A. Ratner, A. Nitzan, J. Chem. Phys. **121**, 11965 (2004).

[89] R. Lake, G. Klimeck, S. Datta, Phys. Rev. B **47**, 6427 (1993).

[90] A. Brandt, Math. Comput. **31**, 333 (1977).

[91] J. J. Palacios, A. J. Pérez-Jiménez, E. Louis, E. SanFabián, J. A. Vergés, Phys. Rev. B **66**, 035322 (2002).

[92] E. Louis, J. A. Vergés, J. J. Palacios, A. J. Pérez-Jiménez, E. SanFabián, Phys. Rev. B **67**, 155321 (2003).

[93] J. Joannopouls, F. Yndurain, Phys. Rev. B **10**, 5164 (1974).

[94] M. Nardelli, Phys. Rev. B **60**, 7828 (1999).

[95] H. Haug, A.-P. Jauho, *Quantum Kinetics in Transport and Optics of Semiconductors* (Springer, Berlin, 1996).

[96] A. R. Williams, P. J. Feilbelman, N. D. Lang, Phys. Rev. B **26**, 5433 (1982).

[97] J. L. Gland, B. A. Sexton, G. B. Fisher, Surf. Sci. **95**, 587 (1980).

[98] A. Böttcher, H. Niehus, J. Chem. Phys. **110**, 3186 (1999).

[99] S. Kohli, C. D. Rithner, P. K. Dorhout, J. Appl. Phys. **91**, 1149 (2002).

[100] B. Hammer, J. K. Nørskov, Nature **376**, 238 (1995).

[101] N. N. Greenwood, A. Earnshaw, *Chemistry of the Elements* (Butterworth-Heinemann Ltd., Linacre House, Jordan Hill, Oxford, 1984).

[102] P. Serp, L. Chateau, R. Feurer, A. Kiennemann, P. Kalck, J. Mol. Catal. A: Chem. **136**, 269 (1998).

[103] E. N. Abarra, A. Inomata, H. Sato, I. Okamoto, Y. Mizoshita, Appl. Phys. Lett. **77**, 2581 (2000).

[104] J. P. Wang, S. N. Piramanayagam, C. H. Hee, L. Huang, S. I. Pang, S. K. Chow, X. Shi, T. C. Chong, Appl. Phys. Lett. **91**, 7694 (2002).

[105] U. Schwingenschlögl, C. Schuster, Chem. Phys. Lett. **439**, 143 (2007).

[106] M. M. Fadlallah, C. Schuster, U. Schwingenschlögl, T. Wunderlich, S. Sanvito, J. Phys.: Condens. Matter **21**, 315001 (2009).

[107] M. Springborg, *Density Functional Method in Chemistry and Material Science* (John Wiley & Sons, Chichester, 1997).

[108] M. M. Fadlallah, C. Schuster, U. Eckern, U. Schwingenschlögl, Europhys. Lett. **89**, 47003 (2010).

[109] G. Autés, C. Barreteau, D. Spanjaard, M.-C. Desjonquéres, Phys. Rev. B **77**, 155437 (2008).

[110] V. dos Santos, C. A. Kuhnen, Thin Solid Films **350**, 258 (1999).

[111] C. E. Lekka, N. Bernstein, M. J. Mehl, D. A. Papaconstantopoulosa, Appl. Surf. Sci. **219**, 158 (2003).

[112] B. Ginatempo, G. Y. Guo, W. M. Temmerman, J. B. Staunton, P. J. Durham, Phys. Rev. B **42**, 2761 (1990).

[113] H. P. Myers, *Introductory Solid State Physics* (Taylor & Francis Inc., New York, 2002).

[114] A. K. Santra, C. N. R. Rao, Appl. Surf. Sci. **84**, 347 (1995).

[115] M. W. Finnis, J. Phys.: Condens. Matter **8**, 5811 (1996).

[116] V. E. Henrich, Rep. Prog. Phys. **48**, 1481 (1985).

[117] F. Didier, J. Jupille, Surf. Sci. **307**, 587 (1994).

[118] M.-H. Schaffner, F. Patthey, W.-D. Schneider, Surf. Sci. **417**, 159 (1998).

[119] O. Robach, G. Renaud, A. Barbier, Phys. Rev. B **60**, 5858 (1999).

[120] T. Suzuki, S. Hishita, K. Oyoshi, R. Souda, Surf. Sci. **442**, 291 (1999).

[121] J. H. Larsen, J. T. Ranney, D. E. Starr, J. E. Musgrove, C. T. Campbell, Phys. Rev. B **63**, 195410 (2001).

[122] P. Stracke, S. Krischok, V. Kempter, Surf. Sci. **473**, 86 (2000).

[123] B. Herschend, K. Hermansson, M. Alfredsson, Y. F. Zhukovsk, E. A. Kotomin, P. W. M. Jacobs, J. Phys. Chem. B **107**, 11893 (2003).

[124] C. Li, R. Wu, A. J. Freeman, C. L. Fu, Phys. Rev. B **48**, 8317 (1993).

[125] J. Cho, K. S. Kim, C. T. Chan, Z. Zhang, Phys. Rev. B **63**, 113408 (2001).

[126] A. M. Ferrari, G. J. Pacchioni, Phys. Chem. **100**, 9032 (1996).

[127] R. Benedek, M. Minkoff, L. H. Yang, Phys. Rev. B **54**, 7697 (1996).

[128] I. V. Yudanov, S. Vent, K. M. Neyman, G. Pacchioni, N. Rösch, Chem. Phys. Lett. **275**, 245 (1997).

[129] J. Purton, S. C. Parker, D. W. J. Bullett, J. Phys.: Condens. Matter **9**, 5709 (1997).

[130] E. Heifets, Y. F. Zhukovskii, E. A. Kotomin, M. Causá, Chem. Phys. Lett. **283**, 395 (1998).

[131] J. Goniakowski, Phys. Rev. B **57**, 1935 (1998).

[132] J. Goniakowski, Phys. Rev. B **58**, 1189 (1998).

[133] N. Lopez, F. Illas, N. Rösch, G. J. Pacchioni, J. Chem. Phys. **110**, 4873 (1999).

[134] H. B. Groen, B. J. Kooi, W. P. Vellinga, J. T. M. D. Hosson, Philos. Mag. A **79**, 2083 (1999).

[135] D. K. Chan, D. N. Seidman, K. L. Merkle, Phys. Rev. Lett. **75**, 1118 (1995).

[136] D. A. Muller, D. A. Shashkov, R. Benedek, L. H. Yang, J. Silcox, D. N. Seidman, Phys. Rev. Lett. **80**, 4741 (1998).

[137] J. C. Fuggle, Surf. Sci. **69**, 581 (1977).

[138] L. H. Tjeng, A. R. Vos, G. A. Sawatzky, Surf. Sci. **235**, 269 (1990).

[139] D. Ochs, W. Maus-Friedrichs, M. Brause, J. Günster, V. Kempter, V. Puchin, A. Shluger, L. Kanotorovich, Surf. Sci. **265**, 557 (1996).

[140] K. J. Chang, M. L. Cohen, Phys. Rev. B **30**, 4774 (1984).

[141] M. Causá, R. Dovesi, C. Pisani, C. Roetti, Phys. Rev. B **33**, 1308 (1986).

[142] U. Schönberger, F. Aryasetiawan, Phys. Rev. B **52**, 8788 (1995).

[143] A. V. Matveev, K. M. Neyman, I. V. Yudanov, N. Rösch, Surf. Sci. **426**, 123 (1999).

[144] V. Musolino, A. Selloni, R. Car, Phys. Rev. Lett. **83**, 3242 (1999).

[145] P. Grünberg, R. Schreiber, Y. Pang, M. B. Brodsky, H. Sowers, Phys. Rev. Lett. **57**, 2442 (1986).

[146] S. A. Wolf, D. D. Awschalom, R. A. Buhrmann, J. M. Daughton, S. von Molnár, M. L. Roukes, A. Y. Chtchelkanova, D. M. Treger, Science **294**, 1488 (2001).

[147] I. Rungger, O. Mryasov, S. Sanvito, Phys. Rev. B **79**, 094414 (2009).

[148] J. Xu, A. P. Mills, Jr., A. Ueda, D. O. Henderson, R. Suzuki, S. Ishibashi, Phys. Rev. Lett. **83**, 4586 (1999).

[149] C. Barth, C. R. Henry, Phys. Rev. Lett. **91**, 196102 (2003).

[150] K. Honkala, H. Häkkinen, J. Phys. Chem. C **111**, 4319 (2007).

[151] D. Chen, X. L. Ma, Y. M. Wang, Phys. Rev. B **75**, 125409 (2007).

[152] Q. S. Wang, N. A. W. Holzwarth, Phys. Rev. B **41**, 3211 (1990).

[153] L. A. Kappers, R. L. Kroes, E. B. Hensley, Phys. Rev. B **1**, 4151 (1970).

[154] Z. Yang, R. Wu, Q. Zhang, D. W. Goodman, Phys. Rev. B **65**, 155407 (2002).

[155] J. Peralta-Ramos, A. M. Llois, I. Rungger, S. Sanvito, Phys. Rev. B **78**, 024430 (2008).

[156] H. Baltache, R. Khenata, M. Sahnoun, M. Driz, B. Abbar, B. Bouhafs, Physica B **344**, 334 (2004).

[157] M. Klaua, D. Ullmann, J. Barthel, W. Wulfhekel, J. Kirschner, R. Urban, T. L. Monchesky, A. Enders, J. F. Cochran, B. Heinrich, Phys. Rev. B **64**, 134411 (2001).

[158] M. M. Fadlallah, C. Schuster, U. Schwingenschlögl, I. Rungger, U. Eckern, Phys. Rev. B **80**, 235332 (2009).

[159] C. J. Cramer, *Essentials of Computational Chemistry* (Wiley, New York, 2004).

[160] J. C. Slater, Phys. Rev. B **81**, 385 (1951).

[161] O. Gunnarsson, B. I. Lundqvist, Phys. Rev. B **13**, 4274 (1976).

[162] D. M. Ceperley, B. J. Alder, Phys. Rev. Lett. **45**, 566 (1980).

[163] S. J. Vosko, L. Wilk, M. Nussair, Can. J. Phys. **58**, 1200 (1980).

[164] W. Koch, M. C. Holthausen, *A Chemist's Guide to Density Functional Theory* (John Wiley, New York, 2002).

[165] J. P. Perdew, Y. Wang, Phys. Rev. B **33**, 8800 (1986).

[166] J. P. Perdew, A. Ruzsinszky, J. Tao, V. N. Staroverov, G. E. Scuseria, G. I. Csonka, J. Chem. Phys. **123**, 062201 (2005).

[167] V. N. Staroverov, G. E. Scuseria, J. Tao, J. P. Perdew, Phys. Rev. B **69**, 075102 (2004).

[168] A. D. Becke, Phys. Rev. A **38**, 3098 (1988).

[169] C. Lee, W. Wang, R. G. Parr, Phys. Rev. B **37**, 785 (1988).

[170] J. P. Perdew, Y. Wang, Phys. Rev. B **45**, 13244 (1992).

[171] J. Tao, J. P. Perdew, V. N. Staroverov, G. E. Scuseria, Phys. Rev. Lett. **91**, 146401 (2003).

[172] J. P. Perdew, S. Kurth, A. Zupan, P. Blaha, Phys. Rev. Lett. **82**, 2544 (1999).

[173] X. Xu, W. A. Goddard III, J. Chem. Phys. **121**, 4068 (2004).

[174] P. Marder, *Condensed Matter Physics* (John Wiley & Sons Inc., 2000).

[175] R. M. Dreizler, E. K. U. Gross, *Density Functional Theory* (Springer, Berlin, 1990).

[176] W. H. Press, B. P. Flannery, S. A. Teukolsky, W. T. Vetterling, *Numerical Recipes in Fortran* (Cambridge University Press, Cambridge, UK, 1992).

[177] M. J. Frisch, G. W. Trucks, H. B. Schlegel, G. E. Scuseria, M. A. Robb, J. R. Cheeseman, J. A. Montgomery, Jr., T. Vreven, K. N. Kudin, J. C. Burant, J. M. Millam, S. S. Iyengar, J. Tomasi, V. Barone, B. Mennucci, M. Cossi, G. Scalmani, N. Rega, G. A. Petersson, H. Nakatsuji, M. Hada, M. Ehara, K. Toyota, R. Fukuda, J. Hasegawa, M. Ishida, T. Nakajima, Y. Honda, O. Kitao, H. Nakai, M. Klene, X. Li, J. E. Knox, H. P. Hratchian, J. B. Cross, V. Bakken, C. Adamo, J. Jaramillo, R. Gomperts, R. E. Stratmann, O. Yazyev, A. J. Austin, R. Cammi, C. Pomelli, J. W. Ochterski,

P. Y. Ayala, K. Morokuma, G. A. Voth, P. Salvador, J. J. Dannenberg, V. G. Zakrzewski, S. Dapprich, A. D. Daniels, M. C. Strain, O. Farkas, D. K. Malick, A. D. Rabuck, K. Raghavachari, J. B. Foresman, J. V. Ortiz, Q. Cui, A. G. Baboul, S. Clifford, J. Cioslowski, B. B. Stefanov, G. Liu, A. Liashenko, P. Piskorz, I. Komaromi, R. L. Martin, D. J. Fox, T. Keith, M. A. Al-Laham, C. Y. Peng, A. Nanayakkara, M. Challacombe, P. M. W. Gill, B. Johnson, W. Chen, M. W. Wong, C. Gonzalez, J. A. Pople, *Gaussian 03, Revision C.02* (Gaussian, Inc., Wallingford, CT, 2004).

[178] K. Hirose, M. Tsukada, Phys. Rev. B **51**, 5278 (1995).

[179] N. D. Lang, Phys. Rev. B **52**, 5335 (1995).

[180] L. Chico, L. M. Falicov, Phys. Rev. B **52**, 6640 (1995).

[181] J. C. Cuevas, A. L. Yeyati, A. Martín-Rodero, Phys. Rev. Lett. **80**, 1066 (1998).

[182] J. M. MacLaren, X.-G. Zhang, W. H. Butler, X. Wang, Phys. Rev. B **59**, 5470 (1999).

[183] S. Crampin, J. B. A. N. van Hoof, M. Nekovee, J. E. Inglesfield, J. Phys.: Condens. Matter **4**, 1475 (1992).

[184] D. Wortmann, H. Ishida, S. Blügel, Phys. Rev. B **66**, 075113 (2002).

[185] P. X. Xu, K. Xia, M. Zwierzycki, M. Talanana, P. J. Kelly, Phys. Rev. Lett. **96**, 176602 (2006).

[186] E. Anglada, J. M. Soler, J. Junquera, E. Artacho, Phys. Rev. B **66**, 205101 (2002).

[187] J. Moreno, J. M. Soler, Phys. Rev. B **45**, 13891 (1992).

[188] D. Fuks, S. Dorfman, E. A. Kotomin, Y. F. Zhukovskii, A. M. Stoneham, Phys. Rev. Lett. **85**, 4333 (2000).

[189] A. M. Rappe, K. M. Rabe, E. Kaxiras, J. D. Joannopoulos, Phys. Rev. B **41**, 1227 (1990).

[190] D. J. Chadi, M.L.Cohen, Phys. Rev. B **8**, 5747 (1973).

[191] J. D. Joannopoulos, M.L.Cohen, J. Phys. C **6**, 1572 (1973).

[192] H. J. Monkhorst, J. D. Pack, Phys. Rev. B **13**, 5188 (1976).

[193] R. A. Evarestov, V. P. Smirnov, Phys. Status Solidi B **119**, 9 (1983).

Acknowledgments

Looking back I can say that it is a great pleasure to be in Germany and spending more than three years on a research that turned out to be challenging and very interesting. I would like to thank all the people whom I have met in Germany, Augsburg, and who made my life full and comfortable in spite of my being far from home. Of course, there are people who were very close to me over these years and to whom I would like to express my sincere gratitude especially my supervisor Prof. Dr. Ulrich Eckern, for giving me the opportunity to do my Ph.D work in his group. I thank him for his constant and professional guidance and supervision, for his unceasing advice and for his encouragement. I have learnt a lot from him. One of the amazing things about him that his help quite often exceeded my expectations. I express my special gratitude and I am indebted to Dr. Cosima Schuster for her understanding, her patience, useful discussions and excellent guidance. This thesis could not have been finished if it were not for the understanding and support of her and Prof. Eckern. I wish to thank Prof. Dr. Udo Schwingenschlögl for his contribution to the work and his help in the publications. I would also like to extend special thanks to Dr. M. Dzierzawa for his good reading and useful corrections to my dissertation.

I would like to acknowledge the members of TP II, Priv.-Doz. Dr. P. Schwab, O. Fialko, Dr. L. Chotorlishvili, Dr. S. Schenk, Dr. C. Gorini and our secretary C. Wunsch for the pleasant and nice atmosphere. I thank SFB 484 and the Egyptian Missions System for financial support. Also, I thank DAAD for giving me the opportunity to visit Mexico, CINVESTAV-Unidad Queretaro, and cooperate with Prof. Dr. Aldo Romero. Last but not least I would like to thank my parents, my wife and my big family for their continuous help. I cannot forget my small family in Physics department, Benha university, Egypt, in particular Prof. A. Rabi, Dr. M. Nour El-Din and Prof. M. El-shaarawy for encouraging me.

Curriculum Vitae

Mohamed Mostafa Fadlallah Elabd
Born in Cairo, Egypt

Date of Birth: December 30, 1974

Qualifications:

June 1997	B.Sc. (Physics), very good with Honor Degree, Faculty of Science, Benha University, Egypt
March 2002	M.Sc. (Theoretical Solid State Physics), Faculty of Science, Benha University, Egypt
2007-2010	Ph.D. (Theoretical Solid State Physics) student, Institut für Physik, Universität Augsburg, Germany

Employments:

1998-2002	Demonstrator, Physics Department, Faculty of Science, Benha University, Egypt
Since 2002	Assistant lecturer, Physics Department, Faculty of Science, Benha University, Egypt
2009-2010	Scientific researcher, Institut für Physik, Universität Augsburg, Germany